Fall 12-17-2018

SUB-NANOMETER COUPLING DISTANCE CONTROL AND PLASMON ENHANCED CARRIER GENERATION AND DYNAMICS IN III-V SEMICONDUCTOR HETEROSTRUCTURES

Sharmin Haq
University of New Mexico

Sharmin Haq

Candidate

Optical Science and Engineering

Department

This dissertation is approved, and it is acceptable in quality and form for publication:

Approved by the Dissertation Committee:

Prof. Terefe G. Habteyes, Chairperson

Prof. Steven R. J. Brueck

Prof. Kavin Malloy

Prof. Francesca Cavallo

Dr. Igal Brener

SUB-NANOMETER COUPLING DISTANCE CONTROL AND PLASMON ENHANCED CARRIER GENERATION AND DYNAMICS IN III-V SEMICONDUCTOR HETEROSTRUCTURES

by

SHARMIN HAQ

B.Sc. & M.S., Applied Physics, Electronics & Communication Engineering, University of Dhaka, Bangladesh, 2010

M.S., Optical Science and Engineering, University of New Mexico, 2016

DISSERTATION

Submitted in Partial Fulfillment of the
Requirements for the Degree of

Doctor of Philosophy

Optical Science and Engineering

The University of New Mexico
Albuquerque, New Mexico

May 2019

DEDICATION

To

My Family

Acknowledgements

First and foremost I would to like to thank my advisor, Prof. Terefe G. Habteyes for giving me the opportunity to be a part of his research group and work on an emerging field of science. I am grateful for his continuous support, advice, and dedicated guidance throughout the years. This helped me to grow as a scientist and prepared me to face the future challenges.

I would like to thank other committee members of my dissertation, Prof. Steven R.J. Brueck, Prof. Kevin Malloy, Prof. Francesca Cavallo, and Dr. Igal Brener for their time and constructive inputs in my research.

I would like to thank Dr. Igal Brenar for giving me the opportunity to use the research facility at Center for Integrated Nanotechnologies (CINT) of Sandia National Laboratory. I would like to acknowledge John Nogan, Anthony James and Doug Pete for training me in different tools at CINT. Thanks a lot Dr. Katie Jungjohann, for facilitating the imaging of the transmission electron microscopy for my samples, and Doug Pete for preparing the samples with care by focused ion beam (FIB).

I would like to thank Dr. Sadhvikas Addamane for fabricating the samples using molecular beam epitaxy (MBE). I would like to thank Dr. Danhong Huang for supporting us with mathematical modeling. Special thanks to Prof. Kavin Malloy for giving us the experimental set-up for temperature dependent measurements. I would like to thank Prof. Ganesh Balakrishnan for allowing me to use the PL set-up at Center for High Technology Materials (CHTM).

I would like to thank all my group members for their supports all the time. All the discussion during our coffee time made the working environment so friendly. I would also like to show my gratitude to all the staff at CHTM for helping me in so many ways.

Finally, I would like to thank my family members and friends, specially my mom, my husband, my elder brother for all their love and support throughout this crazy adventure, specially my toddler boy for all the lovely distractions.

Sub-nanometer coupling distance control and plasmon enhanced carrier generation and dynamics in III-V semiconductor heterostructures

by

Sharmin Haq

B.Sc. & M.S., Applied Physics, Electronics & Communication Engineering, University of Dhaka, Bangladesh, 2010

M.S., Optical Science and Engineering, University of New Mexico, 2016

Ph.D., Optical Science and Engineering, University of New Mexico, 2019

Abstract

Plasmonic modes in metal nanostructures enable light confinement at subwavelength scales. This field confinement is important for exploring the potential of nanotechnology in miniaturization of optics as well as for the advancement of optoelectronic devices, such as photodetectors, photovoltaics, and light-emitting diodes. Plasmon resonances are also ideal for developing ultrasensitive biosensors, and for enhancing surface photochemistry and photocatalysis. The increasing number of plasmon applications requires fundamental understanding of the plasmon coupled system which has not yet been completely understood. Controlling and engineering the plasmon response at the nanoscale will open still more applications in material science, communications, biochemistry and medicine.

In this dissertation, the optical interactions between resonant plasmonic nanoparticles and both polarizable semiconductor substrates and metallic films have been

investigated by analyzing the scattering properties of the plasmonic nanoparticles and the photoluminescence (PL) of emitters embedded in the semiconductor substrate. Fundamental studies of the coupling of the localized surface plasmon resonance of colloidal gold nanoparticles with III-V semiconductor quantum dots (QDs), and metallic gold-films have been carried out. By coupling colloidal gold nanorods (AuNRs) to InAs QDs, embedded in InGaAs/GaAs quantum well, plasmon enhanced carrier generation and photon emission are investigated by monitoring the PL intensity enhancement at room temperature. The length scales of the near-field confinement, carrier diffusion, and excitation energy transfer to the metal surface (that leads to quenching of PL at small AuNR-InAs separation distances), have been determined systematically both experimentally and theoretically by varying the GaAs capping layer thickness. After establishing the dependence on separation, the temperature dependence of plasmon enhanced carrier generation and photon emission are studied by analyzing QDs PL.

Atomic layer deposition (ALD) of Al_2O_3 dielectric spacer layers is developed for precise, atomic scale control of separation and uniform conformal deposition. Using the AuNR-SiO_2 system as a reference, the optical interaction in a AuNR-GaAs system separated by a ALD Al_2O_3 dielectric spacer is explored. Super-resolved optical interaction has been demonstrated for the metallic gold particle-film system separated by Al_2O_3 spacer layer. Controlling the spacer layer thickness at a sub-nanometer length scale provides the opportunity to experimentally examine the transition from the classical to quantum mechanical regime. The optical coupling in a metallic particle-film system is investigated from capacitive to conductive junction. These fundamental analysis may help to advance the development of plasmonic devices.

Table of Contents

List of figures

Chapter 1

Introduction

1.1 **Fundamentals of plasmonics**

Plasmons are oscillation of free electrons which can be propagating surface plasmon polaritons (SPP) or localized surface plasmons. SPPs are electromagnetic excitations propagating along the interface between a dielectric and a metal, confined in the perpendicular direction.[1] In this dissertation, we focus only on localized surface plasmons, and it has been utilized in the entire work.

Localized surface plasmons are one of the fundamental excitations of plasmonics, which are non-propagating excitations of the conduction electrons of metallic nanostructures coupled to the electromagnetic field. The curved surface of the small, sub-wavelength conductive nanoparticle exerts restoring force on the driven electrons, therefore resonance can occur, leading to field amplification both inside and outside the particle in the near-field regime.[2] This resonance is called localized surface plasmon resonance, which can be excited by direct light illumination as shown in Figure 1.1.

For gold and silver nanoparticles, the resonances fall into visible region of the electromagnetic spectrum, exhibiting bright colors both in transmitted and reflected light, due to resonantly enhanced absorption and scattering. This property has applications for hundreds of years, for example in the staining of glass for windows or decorative cups. In recent years, a number of modern applications of localized plasmon resonances have attracted the investigations of scientists of different background.

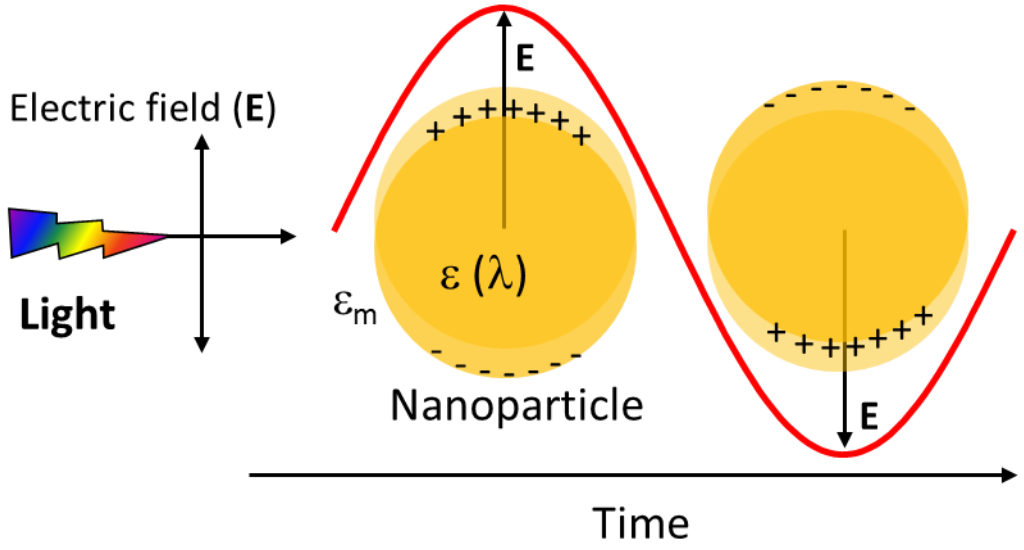

Figure 1.1 Localized surface plasmon resonance excited by light of wavelength >> particle size causes collective oscillation of free electrons.

The optical properties of metal nanopartilces show distinct differences relative to bulk or thin film as shown by Maier and Atwater (Figure 1.2).[3] They show the film absorbs light throughout the near-infrared and visible regions due to free electron absorption, in contrast the process quenched for the nanoparticles below the energy 2 eV. The absorption peak around 2.25 eV is dipolar surface plasmon resonance. This modified optical response leads to bright colors of the noble metal nanoparticles. Above the dipole resonance energy, the absorption is similar for film and nanoparticles due to dominance of interband transitions.

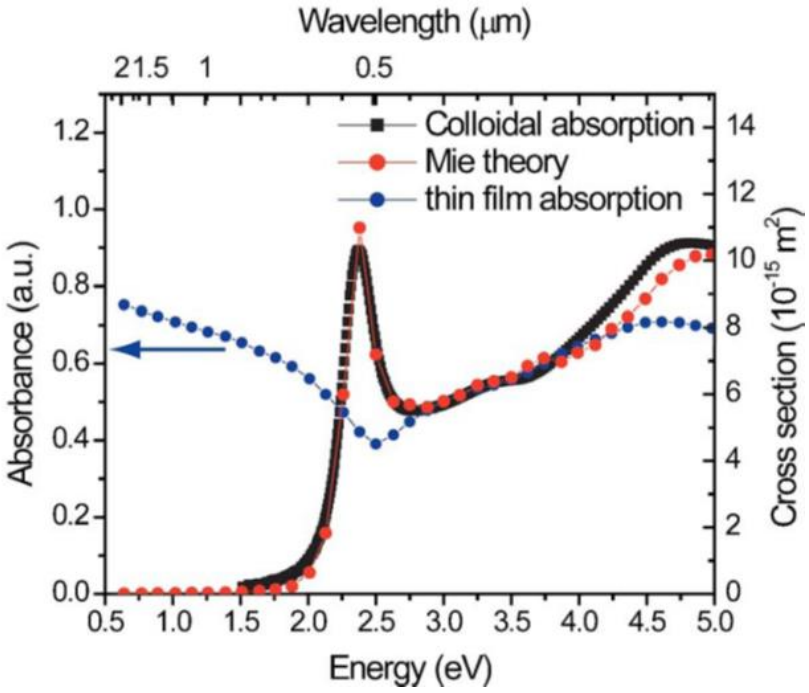

Figure 1.2 Calculated absorption spectrum of a thin gold film (blue dots) and 30 nm Au nanoparticles in water (red dots) using classical electromagnetic theory. Measured absoption spectrum of an aqueous solution of 30 nm Au nanoparticle (black dots) shows good agreement with the theory. (Maier & Atwater, J. Appl. Phys. 98, 011101, ***2005****)*[3]

The resonance of the noble metal particle is due to the confinement of conduction electrons to the small particle volume. Upon electromagnetic wave excitation of particles with diameter $d<<\lambda$, the conduction electrons move in phase leading to a buildup polarization charges on the particle surface. These charges act as an effective restoring force causing resonance to occur at a specific frequency. In general, the spectral position, damping and strength of the dipole plasmon resonance depends on the particle size, geometry,[4] orientation,[5] material, and dielectric function of the surrounding medium.[6, 7] For a spherical metal nanoparticle of radius $r<<\lambda$ surrounded by medium of dielectric constant ε_m, the polarizability of the particle is expressed as,

$$\alpha = 4\pi r^3 \frac{\varepsilon(\lambda) - \varepsilon_m}{\varepsilon(\lambda) + 2\varepsilon_m}$$

where ε (λ) is complex dielectric function of the metal. The spectral position of resonance is red-shifted with increasing dielectric constant of the surrounding media due to building up polarization charges that weakens the total restoring force.

1.2 **Localized surface plasmon resonance utilizing colloidal nanoparticles**

Experimentally, metal nanoparticles of different shapes can be fabricated using both colloidal synthesis methods,[8] and top-down nanofabrication techniques such as electron-beam lithography.[5, 6] Top-down fabrication techniques have excellent capabilities of placing and orienting complex structures, but the nanostructures are polycrystalline and highly defective at their edges. The plasmon resonance may suffer from damping due to the edge roughness. In contrast, colloidal nanoparticles are single-crystalline and have smooth edges comparing lithographically fabricated nanostructures. Hence, strong resonance is observed. Also, colloidal nanoparticles are easy to couple with any other structures as well as cost effective. Most importantly, coupling distance can be controlled with sub-nanometer accuracy using colloidal nanoparticles, which is not possible with lithographically fabricated nanostructures. To take all these benefits of colloidal nanoparticles, we utilize colloidal gold nanorods in this study to investigate the optical interactions of plasmon coupled systems. But colloidal nanoparticles are coated with surfactants, therefore there is an inherent spacer layer around the nanoparticles. For an example, the thickness measured for cetyltrimethylammonium bromide (CTAB) surfactants coated around the gold nanorods is ~ 3 nm (measured in solution).[11, 12] The properties of the surfactants determine the nature of the interaction, hence the plasmonic

response of the coupled system. This spacer due to surfactants may cause some difficulties in controlling the coupling distance for plasmonic systems.

1.3 **Plasmon coupled system**

The ability of plasmonic systems to localize light at sub-wavelength volumes has enabled a variety of applications, including nonlinear optics,[13] enhancement of spontaneous emission,[14] and surface enhanced Raman scattering.[15] A wide range of plasmonic systems have been studied intensely and are being actively considered for biomedical[16] and photonic[17,18] applications, because of their enormous potential as sensors and miniaturized photonic components. Since the surface plasmon resonance is strongly affected by the surrounding environment of the nanoparticles, the far-field scattering from the nanoparticle provides a convenient means to study the near-field coupling effects of the plasmonic systems.

The effective ways to couple, confine, enhance, and utilize light down to sub-nanometer scale have been prime concerns of nanophotonics. Plasmonic nanocavities made of noble metallic nanostructures play an important role in addressing these concerns. However, plasmonic response depends strongly on the morphology of the gap, especially when the gaps are sub-nanometer scales. Despite of having several reports on a number of geometries in the literature,[19–22] it is still unclear which are optimal for coupling light into emitters within these nanocavities. Therefore, parameters such as local field strength, far-field cross sections, spatial charge distributions around the geometry, and losses due to damping are needed to be investigated carefully. Controlling and tuning the optical properties of the plasmon coupled systems relies on the precise manipulation of the gap

size, which determines how strongly they are coupled. Hence, much effort has been devoted to precise control over this gap distance, yet, significant challenges remain. Usually, thin dielectric spacer layers are introduced between the two metallic interfaces to prevent conductive contact. As discussed earlier, precise top-down fabrication of such nanoscale gap is extremely challenging. In contrast, bottom-up approach allows precise control of the spacer layer thickness between nanoparticles and metal/semiconductor films coated with dielectric spacer layers. Charge oscillations in such nanoparticles deposited on metal/semiconductor films coated with thin dielectric spacer layers, couple with the image charges in the film,[19,23] providing equivalent enhancement and confinement to the plasmonic dimer systems. Thus, film coupled nanoparticle system separated by dielectric spacer layer is promising due to its remarkable precision and reproducibility.[24, 25]

1.4 **Motivation**

The localized surface plasmon resonance of metallic nanoparticle resulting in large field amplification cannot be employed unless it is coupled to another nanostructure or film. Once coupled, the nanoparticles can be used to improve the sensitivity of biosensors,[15,26,27] solar energy harvesting devices,[28] optoelectronic devices,[17,18,29] color printing[30] and drive chemical reactions,[31,32] to mention some applications. The characteristics of the plasmon resonance depend on particle size, shape, material, and the dielectric environment surrounding the nanoparticle. Therefore, to couple the plasmonic structure with another nanostructure, thin-film, molecule, or quantum dot, it is vital to understand the interaction of the plasmon coupled system, which has not been yet

completely understood for the widespread applications. In recent years, the plasmon coupled systems have been the subject of extensive research due to promising platform for various applications.[33–37] To this extent, we investigate the optical interaction of colloidal plasmon coupled III-V semiconductor quantum dots (QDs) both in near-field and far-field regime to enhance the emission efficiency of optoelectronic devices, improve material and device properties, and reduce the complexity of array detectors. For further understanding, temperature dependence of the plasmon coupled quantum dots is also investigated. The optimization of the coupling is also carried out for further improvement of the device performance which is really challenging. To this extent, the coupling gap has been controlled with dielectric spacer layer at sub-nanometer length scale using atomic layer deposition. Then, the plasmonic interactions are investigated varying coupling distance with sub-nanometer accuracy for different polarizable materials (III-V semiconductor, and metal).

1.5 **Outline of dissertation**

Chapter 2 focuses on systematic study for understanding the effect of localized surface plasmon resonances on enhancing the carrier generation and photon emission for the plasmonic system, colloidal gold nanorods and InAs semiconductor quantum dots as an emitter embedded in a InGaAs quantum well using GaAs as a capping layer, by monitoring the emission enhancement. The distance dependence of energy transfer, near-field confinement and carrier diffusion have been investigated both experimentally and

theoretically by analyzing the carrier dynamics through GaAs capping layer controlling the thickness with sub-nanometer accuracy.

Chapter 3 investigates the temperature and distance dependent plasmonic effect on emission enhancement for InAs/InGaAs/GaAs dot-in-a –well structure. Temperature dependent carrier dynamics have been investigated for the range 20 K-290 K.

Chapter 4 focuses on controlling the gap between plasmonic nanostructure and GaAs semiconductor to optimize the emission enhancement for InAs/InGaAs/GaAs dot-in-a –well structure. Organic and inorganic spacer layers are introduced to control the gap. Optical interaction utilizing inorganic spacer layer of Al_2O_3 dielectric using atomic layer deposition, is explored by measuring the dark-field scattering of the plasmonic nanoparticles varying the thickness in nanometer scale. The plasmon coupling effect for GaAs semiconductor and SiO_2 dielectric are compared for various Al_2O_3 spacer layer thicknesses.

In Chapter 5, optical interaction of the metallic gold particle-film separated by an inorganic dielectric spacer layer precisely controlled in Ångstrom length scale using atomic layer deposition, is examined by measuring the dark-field scattering of the nanoparticles. The optical interaction of the gold particle-film separated by Al_2O_3 spacer layer is explored experimentally in the classical and quantum mechanical regime by controlling the spacer layer thickness with sub-nanometer accuracy.

Chapter 6 discusses about the summary of the dissertation, and the future research directions for the plasmon coupled systems.

References

1. Maier, S. A. Surface Plasmon Polaritons at Metal / Insulator Interfaces. in *Plasmonics: Fundamentals and Applications* (ed. Maier, S. A.) 21–37 (Springer US, 2007). doi:10.1007/0-387-37825-1_2

2. Maier, S. A. Localized Surface Plasmons. in *Plasmonics: Fundamentals and Applications* (ed. Maier, S. A.) 65–88 (Springer US, 2007). doi:10.1007/0-387-37825-1_5

3. Maier, S. A. & Atwater, H. A. Plasmonics: Localization and guiding of electromagnetic energy in metal/dielectric structures. *Journal of Applied Physics* **98**, 011101 (2005).

4. Sönnichsen, C. *et al.* Drastic Reduction of Plasmon Damping in Gold Nanorods. *Phys. Rev. Lett.* **88**, 077402 (2002).

5. Habteyes, T. G. Direct Near-Field Observation of Orientation-Dependent Optical Response of Gold Nanorods. *J. Phys. Chem. C* **118**, 9119–9127 (2014).

6. Knight, M. W., Wu, Y., Lassiter, J. B., Nordlander, P. & Halas, N. J. Substrates Matter: Influence of an Adjacent Dielectric on an Individual Plasmonic Nanoparticle. *Nano Lett.* **9**, 2188–2192 (2009).

7. Xu, Z. Optical Properties of Metal Clusters By Uwe Kreibig (I. Physikalisches Inst. der RWTH Aachen, Gmermany) and Michael Vollmer (Technische Physik Brandenburg, Germany). Springer: New York. 1994. xvii + 532 pp. $69.00. ISBN 0-387-57836-6. *J. Am. Chem. Soc.* **118**, 6098–6098 (1996).

8. Sun, Y. & Xia, Y. Shape-Controlled Synthesis of Gold and Silver Nanoparticles. *Science* **298**, 2176 (2002).

9. Niklasson, G. A. & Craighead, H. G. Optical response and fabrication of regular arrays of ultrasmall gold particles. *Thin Solid Films* **125**, 165–170 (1985).

10. Craighead, H. G. & Niklasson, G. A. Characterization and optical properties of arrays of small gold particles. *Appl. Phys. Lett.* **44**, 1134–1136 (1984).

11. Hore, M. J. A. *et al.* Probing the Structure, Composition, and Spatial Distribution of Ligands on Gold Nanorods. *Nano Lett.* **15**, 5730–5738 (2015).

12. Gómez-Graña, S. *et al.* Surfactant (Bi)Layers on Gold Nanorods. *Langmuir* **28**, 1453–1459 (2012).

13. Scalora, M. *et al.* Second- and third-harmonic generation in metal-based structures. *Phys. Rev. A* **82**, 043828 (2010).

14. Anger, P., Bharadwaj, P. & Novotny, L. Enhancement and Quenching of Single-Molecule Fluorescence. *Phys. Rev. Lett.* **96**, 113002 (2006).

15. Moskovits, M. Surface-enhanced Raman spectroscopy: a brief retrospective. *Journal of Raman Spectroscopy* **36**, 485–496 (2005).

16. Xu, H., Bjerneld, E. J., Käll, M. & Börjesson, L. Spectroscopy of Single Hemoglobin Molecules by Surface Enhanced Raman Scattering. *Phys. Rev. Lett.* **83**, 4357–4360 (1999).

17. S. C. Lee, S. Krishna & S. R. J. Brueck. Plasmonic-Enhanced Photodetectors for Focal Plane Arrays. *IEEE Photonics Technology Letters* **23**, 935–937 (2011).

18. Senanayake, P. *et al.* 3D Nanopillar optical antenna photodetectors. *Opt. Express* **20**, 25489–25496 (2012).

19. Chikkaraddy, R. *et al.* How Ultranarrow Gap Symmetries Control Plasmonic Nanocavity Modes: From Cubes to Spheres in the Nanoparticle-on-Mirror. *ACS Photonics* **4**, 469–475 (2017).

20. Bosman, M., Anstis, G. R., Keast, V. J., Clarke, J. D. & Cortie, M. B. Light Splitting in Nanoporous Gold and Silver. *ACS Nano* **6**, 319–326 (2012).

21. Koh, A. L., Fernández-Domínguez, A. I., McComb, D. W., Maier, S. A. & Yang, J. K. W. High-Resolution Mapping of Electron-Beam-Excited Plasmon Modes in Lithographically Defined Gold Nanostructures. *Nano Lett.* **11**, 1323–1330 (2011).

22. Zhu, W. *et al.* Quantum mechanical effects in plasmonic structures with subnanometre gaps. *Nature Communications* **7**, 11495 (2016).

23. Aravind, P. K. & Metiu, H. Use of a perfectly conducting sphere to excite the plasmon of a flat surface. 1. Calculation of the local field with applications to surface-enhanced spectroscopy. *J. Phys. Chem.* **86**, 5076–5084 (1982).

24. Moreau, A. *et al.* Controlled-reflectance surfaces with film-coupled colloidal nanoantennas. *Nature* **492**, 86 (2012).

25. Akselrod, G. M. *et al.* Large-Area Metasurface Perfect Absorbers from Visible to Near-Infrared. *Advanced Materials* **27**, 8028–8034 (2015).

26. Xu, H., Bjerneld, E. J., Käll, M. & Börjesson, L. Spectroscopy of Single Hemoglobin Molecules by Surface Enhanced Raman Scattering. *Phys. Rev. Lett.* **83**, 4357–4360 (1999).

27. Chen, X., Ciracì, C., Smith, D. R. & Oh, S.-H. Nanogap-Enhanced Infrared Spectroscopy with Template-Stripped Wafer-Scale Arrays of Buried Plasmonic Cavities. *Nano Lett.* **15**, 107–113 (2015).

28. Atwater, H. A. & Polman, A. Plasmonics for improved photovoltaic devices. *Nature Materials* **9**, 205 (2010).

29. Guo, J., Wu, Z., Li, Y. & Zhao, Y. Design of plasmonic photodetector with high absorptance and nano-scale active regions. *Opt. Express* **24**, 18229–18243 (2016).

30. Stewart, J. W., Akselrod, G. M., Smith, D. R. & Mikkelsen, M. H. Toward Multispectral Imaging with Colloidal Metasurface Pixels. *Advanced Materials* **29**, 1602971 (2016).

31. Brongersma, M. L., Halas, N. J. & Nordlander, P. Plasmon-induced hot carrier science and technology. *Nature Nanotechnology* **10**, 25 (2015).

32. Tesema, T. E., Kafle, B., Tadesse, M. G. & Habteyes, T. G. Plasmon-Enhanced Resonant Excitation and Demethylation of Methylene Blue. *J. Phys. Chem. C* **121**, 7421–7428 (2017).

33. Atwater, H. A. & Polman, A. Plasmonics for improved photovoltaic devices. *Nature Materials* **9**, 205 (2010).

34. Zhu, Z. *et al.* Plasmon-Enhanced Fluorescence in Coupled Nanostructures and Applications in DNA Detection. *ACS Appl. Bio Mater.* **1**, 118–124 (2018).

35. Chen, W., Zhang, S., Deng, Q. & Xu, H. Probing of sub-picometer vertical differential resolutions using cavity plasmons. *Nature Communications* **9**, 801 (2018).

36. Nie, S. & Emory, S. R. Probing Single Molecules and Single Nanoparticles by Surface-Enhanced Raman Scattering. *Science* **275**, 1102 (1997).

37. Xu, H., Bjerneld, E. J., Käll, M. & Börjesson, L. Spectroscopy of Single Hemoglobin Molecules by Surface Enhanced Raman Scattering. *Phys. Rev. Lett.* **83**, 4357–4360 (1999).

Chapter 2

Active mediation of plasmon enhanced localized exciton generation, carrier diffusion and enhanced photon emission

Abstract

Understanding the enhancement of charge carrier generation and their diffusion is imperative for improving the efficiency of optoelectronic devices particularly infrared photodetectors that are less developed than their visible counterparts. Here, using gold nanorods as model plasmonic systems, InAs quantum dots (QDs) embedded in an InGaAs quantum well as an emitter, and GaAs as an active mediator of surface plasmons for enhancing carrier generation and photon emission, the distance dependence of energy transfer and carrier diffusion have been investigated both experimentally and theoretically. Theoretical study of the temporal-evolution of the electron-hole occupation number of the excited states of the QDs indicates that the emission enhancement trend is determined by the carrier diffusion and capture rates.

2.1 Introduction

Excitons and localized surface plasmons are the two important excitation characteristics of nanoscale materials. The coupling between excitonic and plasmonic materials promises control of photon emission[1–3] and creation of new metamaterial properties[4] that do not exist in nature. Fundamental understanding of exciton-plasmon interaction can lead to development of efficient photovoltaics,[5–7] photodetectors,[8–11] photocatalysis,[12,13] and other optoelectronic devices. Classic experiments on exciton-plasmon interactions have often used optically transparent spacer materials between the

plasmonic metal and excitonic semiconductor materials.[1, 3, 12, 13] Coupling through optically transparent spacers does not allow studying charge transport process. On the other hand, studies on plasmon enhanced near-infrared photo-detectors are focused on coupling metallic two-dimensional-hole-arrays with layered semiconductor materials such as InAs/InGaAs/GaAs dot-in-a-well (DWELL) structures.[8,16] This enhancement mechanism exploits the extraordinary optical transmission effect,[17] where the transmitted field extends to about 1 μm length covering the whole active region,[16] emission interfere with the surface plasmon waves, and does not allow fundamental understanding of localized exciton generation, charge carrier diffusion and recombination.

In this work,[18] energy transfer and charge carrier diffusion are investigated systematically taking advantage of the tight electric field localization at the interfaces of plasmonic gold nanorods (AuNRs) and semiconductor GaAs that is grown over the InAs/InGaAs DWELL with accurate control of the GaAs thickness. When excitation energy that is above the GaAs band gap is chosen, the localized electric field enhances generation of electron-hole pairs (excitons) in a defined spatial region away from the InAs QDs so that carrier diffusion and capture rates are studied by monitoring the emission intensity of the QDs. The fact that the GaAs thickness can be controlled with sub-nanometer accuracy allows us to study the distance dependencies of near-field confinement, carrier diffusion and excitation energy transfer to the metal surface that leads to quenching of photoluminescence (PL) at short AuNR-InAs separation distances.

We note that the AuNRs plasmon resonances that overlap with the excitation wavelength, $\lambda = 633$ nm (energy = 1.96 eV) are far from the emission wavelength, $\lambda \approx 1200$ nm (energy ~1.03 eV) of the QDs. Therefore, the PL enhancement originates

purely from the enhancement of photoabsorption and exciton generation inside the GaAs and InGaAs layers. All the optical measurements have been carried out at room temperature at which the thermal energy is larger than the exciton binding energy of GaAs (~4 meV, corresponding to thermal energy ~49 K). As a result, the excitons generated at the plasmonic hot spots of the AuNR-GaAs interface can dissociate, and the PL enhancement can be attributed to the diffusion of charge carriers (electrons and holes) to the InAs QDs. When the GaAs thickness is comparable to the near-field decay length, the near-field directly enhances the exciton generation inside the InAs/InGaAs, where electron-hole recombination may dominate over exciton dissociation because of the proximity to the emitting QDs.

2.2 Methods

2.2.1 Fabrication and integration of materials

The InAs/InGaAs/GaAs semiconductor materials are grown at Center for High Technology Materials (CHTM) using a molecular beam epitaxy (MBE) reactor on GaAs (001) substrates. First, the GaAs substrate is thermally treated at 630 °C for 20 min to remove the native oxide. The surface is then smoothed by growing a 150 nm thick GaAs layer at 580 °C. Subsequent growth of InGaAs, InAs and 1.5 nm GaAs at 475 °C results in InAs QDs confined within the higher band gap InGaAs and GaAs materials. An additional GaAs layer of different thickness is grown (at 580 °C) for studying the distance dependence of the charge carrier generation and diffusion. After removing the excess surfactants from the commercially obtained gold nanorods solution (Nanopartz Inc.) through centrifugation and re-suspension in water, the plasmonic gold nanorods are dispersed on the GaAs surface

by drop-casting and drying the aqueous solution. The AuNRs are applied only on a smaller portion of the sample covering 20% of the sample so that the emission intensity can be compared by recording the photoluminescence (PL) spectra from the two regions (with and without AuNRs).

2.2.2 Photoluminescence measurement and far-field optical characterizations

The photoluminescence spectra of the InAs/InGaAs/GaAs quantum dot- in-a-well are acquired at room temperature using a conventional lock-in technique and a modulated HeNe laser ($\lambda = 632.8$ nm, average power of 5 mW, and intensity of 0.16 W/cm^2) for excitation. Emission from the sample was dispersed by a 0.3 m grating monochromator and detected using a 2153 femtowatt InGaAs photoreceiver from Newport (wavelength range: 800-1700 nm).

The dark-field scattering images of the gold nanorods are obtained using a GX51 Olympus microscope objective of numerical aperture 0.9. The AuNRs are excited with 100W halogen lamp white light source. After the dark-field images are obtained, single particle scattering spectra are recorded by centering the individual gold nanorods in the focus of the collection objective and directing the scatted light into a spectrometer (Isoplane Spectrograph of Princeton Instruments) that is equipped with a thermoelectrically cooled (−75 °C) deep depleted CCD camera. The schematic of the dark-field set up is shown in Chapter 5.

2.2.3 Topographic and near-field optical characterizations

The topographic and near-field optical images are obtained using an integrated AFM/Near-field system (Neaspec, GmbH). To avoid distortion of the plasmon mode profiles of the samples, the near-field optical images of the gold nanorods are obtained implementing an orthogonal excitation and detection scheme. That is, the sample is excited with an incident laser ($\lambda = 632.8$ nm) that is polarized perpendicular to the AFM tip (Arrow-NCPt) and vertically polarized scattered light is selectively detected as described in ref. 16.

2.2.4 Electromagnetic simulation

The scattering and near-field experimental results are reproduced in electromagnetic simulation. The electromagnetic simulation is carried out using finite-difference time domain (FDTD) method, which is implemented using a commercial software package (Lumerical Solutions, Inc.). A total-field scattered field source scheme is used to introduce light energy into the simulation region, where the grid size is 0.5 nm for all x-, y- and z-axes.

2.3 Results and discussion

The interfacial and energetic structures of the integrated plasmonic and semiconductor materials are illustrated in the schematic shown in Figure 2.1 The spacing between the GaAs and the AuNR surfaces can vary depending on the amount of surface ligands (represented by short lines in Figure. 2.1a) on the colloidal AuNRs. The size of the AuNRs (nominal size: 40 nm diameter and 80 nm length; see ref.[19] for the size distribution) is chosen so that the plasmon resonances overlap with the 633 nm excitation wavelength. As illustrated in Figure 2.1b, the excitation energy of the laser ($hc/\lambda = 1.96$ eV, where h is

Planck's constant and *c* is the speed of light) is above the interband electronic transition energies of GaAs (~1.43 eV), InGaAs (~1.26 eV), and InAs (~1.03 eV) materials. Excitation of the localized surface plasmon resonances of the AuNRs interfaced with the GaAs further enhances the exciting electric field and improves the efficiency of exciton generation. The topographic atomic force microscope (AFM) image in Figure 2.1c shows that our molecular beam epitaxy crystal growth procedure produces close-packed self-assembled InAs QDs. The growth of the InGaAs and GaAs layers results in a planar surface as seen in Figure 2.1d. The topographic image of the region, where an aqueous solution of gold nanorods is drop-cast on the GaAs surface shows randomly distributed individual AuNRs and some aggregates as shown in Figure 2.1e.

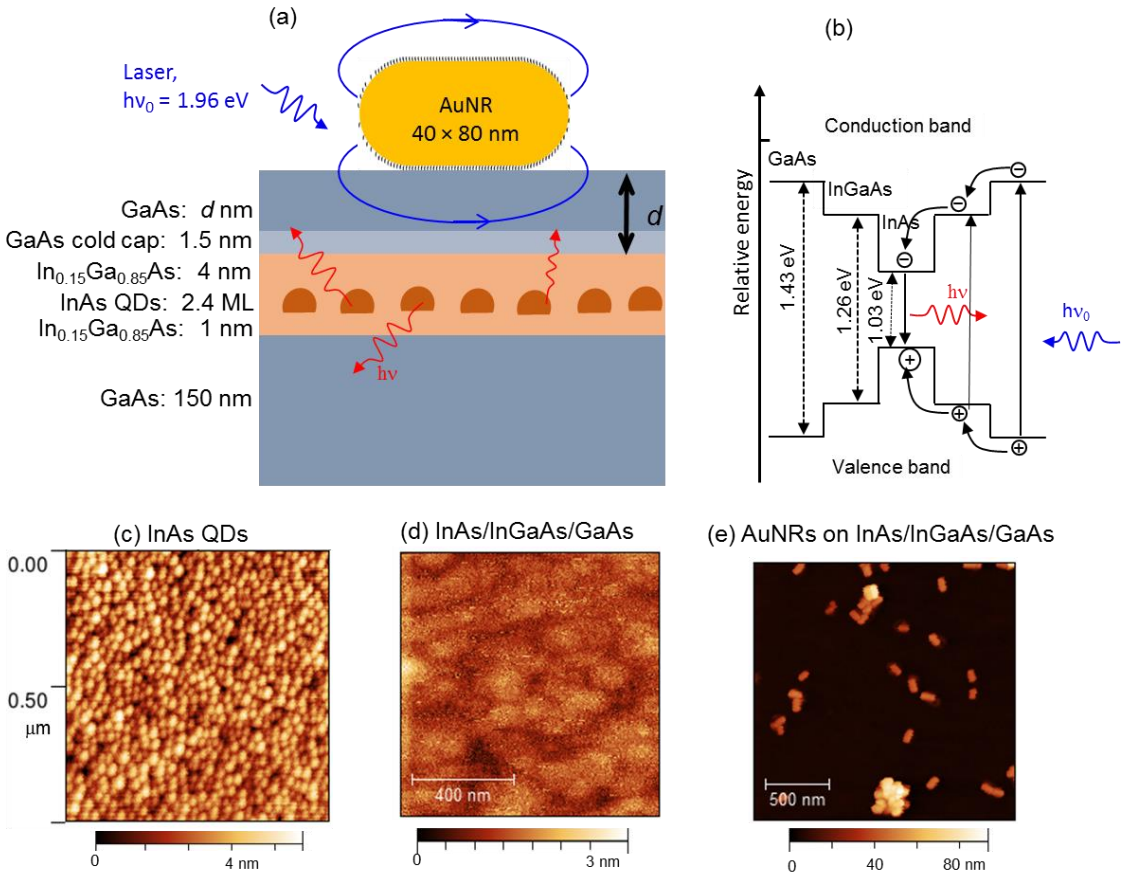

*Figure 2.1 Integration of semiconductor and plasmonic materials (**a**) Schematic showing the InAs quantum dots (QDs) confined in an InGaAs quantum well, capped with GaAs of variable thickness (d) and coupled to a single gold nanorod (AuNR). The short lines around the colloidal AuNR represent the surface ligands (cetyltrimethylammonium bromide). The plasmon near-field enhances electron-hole pair generation in the GaAs and InGaAs layers and the enhancement of photon emission by the InAs QDs depends on the carrier capture rates from the GaAs (black arrow) and from the InGaAs well (green arrow) by the QDs. (**b**) The energy level diagram shows that the excitation energy (1.96 eV) is high enough to promote electron from the valence band to the conduction band in any of the materials including the GaAs that has the highest band gap energy. (**c**–**e**) Topographic AFM scan images obtained (**c**) before the InGaAs and GaAs layers are grown, (**d**) after the InGaAs and GaAs layers are grown, and (**e**) after drop-casting the AuNRs on the GaAs surface. (Scientific reports, 7, 864, 2017)*[18]

The distribution of the AuNRs over a larger area is displayed in the diffraction limited dark-field scattering image in Figure 2.2a. In agreement with previous observations on silicon substrate,[20] the dark-field images of individual AuNRs on GaAs surface have doughnut shaped structures. Interestingly, the color of the scattering images of the individual AuNRs ranges from red to green (see the inset image in Fig. 2.2a, which can be

sorted as red, orange, yellow and green (ROYG). Single particle scattering spectra have been recorded from the particles that appear red, orange, yellow and green in the dark-field image, and representative results are presented in Fig. 2.2b (using the corresponding line color), along with the scattering spectrum of an ensemble of the AuNRs (black curve). The plasmon scattering spectra of the red particles have 666 ± 17 nm peak wavelength and 81 ± 5 nm full-width-at-half maximum (FWHM), compared to 628 nm average peak wavelength and 52 nm FWHM for the same size AuNRs on a glass substrate ($\varepsilon_{SiO2} = 2.25$ at 632.8 nm excitation wavelength), which have been characterized under the same optical settings. The significant red-shift and broader FWHM of the AuNR resonances on GaAs compared to that on glass, can respectively be attributed to the high refractive index (3.86 at wavelength 633 nm[21]) and the absorption property of the GaAs substrate as can be realized from its dielectric function ($\varepsilon_{GaAs} = 14.83 + i1.52$ at 632.8 nm excitation wavelength). As seen in Fig. 2.2b, the spectra are progressively broadened as the color changes from red to orange and to yellow. Finally, spectral splitting is observed for the green particles that have very weak overall scattering intensity. The theoretical scattering spectra (Figure 2.2c), calculated using finite-difference time domain (FDTD) method of electromagnetic simulation, agree with the measured spectra (Figure 2.2b) of the red particles when there is 0.5 to 1.0 nm gap between the AuNR and GaAs surfaces. The spectra of the green particles is reasonably reproduced in the simulation when the AuNR is in direct contact with the GaAs surface as shown by the green curve in Figure 2.2c: the longitudinal plasmon resonance shifts to the red by about 150 nm with respect to that supported on glass surface, and a substrate-induced plasmon resonance[20,22] appears around 600 nm. Based on this comparison of experimental and theoretical results, the ROYG color

can be attributed to different proximity of the AuNRs to the GaAs, R being the furthest from the surface and G the closest. The variation in the separation distances can mainly be attributed to different amounts of the surface ligands (cetyltrimethylammonium bromide) on the colloidal gold nanorods. In our study of plasmon enhanced exciton generation and carrier diffusion, the illumination area is relatively large (~3 mm^2), and therefore, the enhancement results from ensemble averaging represented by the black spectrum in Figure 2.2b.

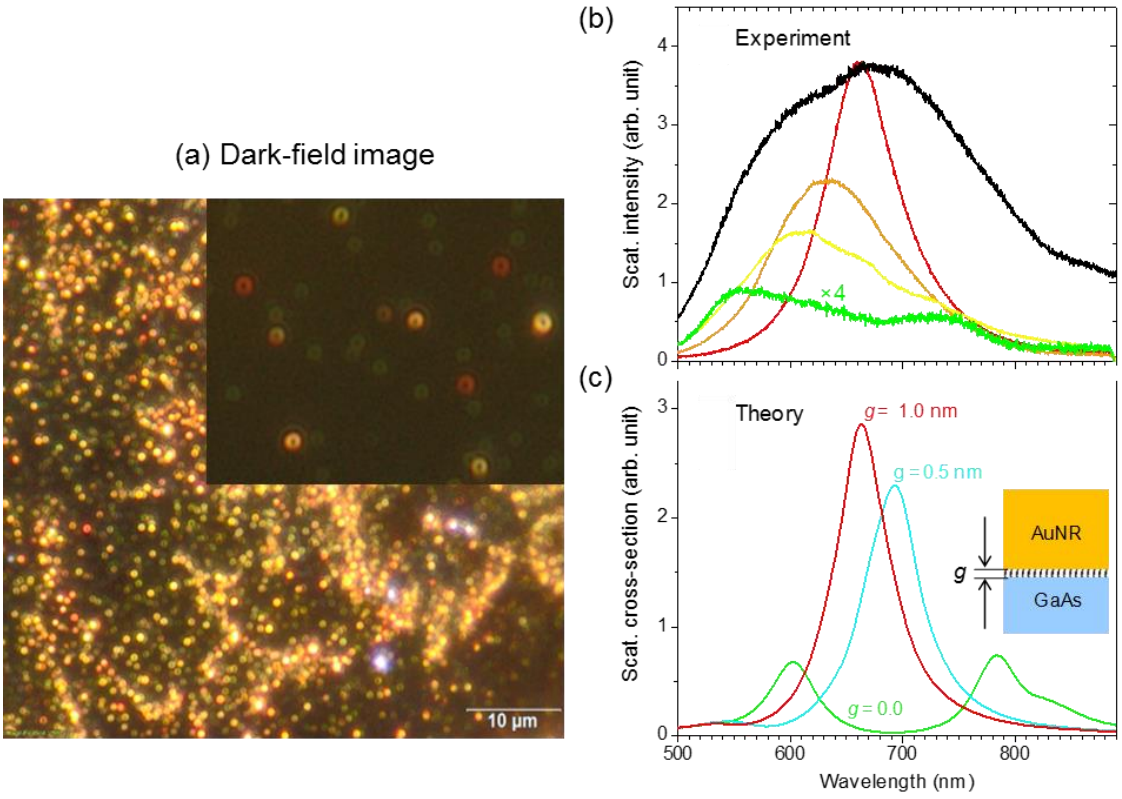

Figure 2.2 Optical properties of colloidal AuNRs deposited on GaAs surface. ***(a)*** *Dark-field image of AuNRs on GaAs surface. The color of the dark-field images of the individual AuNRs varies from red to green, depending on the proximity of the AuNRs to the GaAs surface.* ***(b)*** *Scattering spectra of individual AuNRs that appear red, orange, yellow and green in the dark-field image (shown with the corresponding colors) along with the scattering spectrum of collection of AuNRs (black curve). The black curve is recorded at lower acquisition time to avoid detector saturation and the intensity is adjusted to match its maximum to that of the red spectrum.* ***(c)*** *The calculated scattering cross-section of AuNR (40 nm × 80 nm) when the AuNR-GaAs gap is 0 (green line), 0.5 nm (cyan line) and 1.0 nm (red line). (Scientific reports, 7, 864, 2017)*[18]

High resolution electric field imaging using our apertureless near-field scanning optical microscope (ANSOM)[23,24] shows very weak near-field amplitude on the gold nanorods when supported on GaAs (Figure 2.3a), compared to the large near-field amplitude of the dipolar mode for the AuNRs supported on a silica surface (Fig. 2.3b), which shows orientation dependent near-field optical response in agreement with our previous results.[19] This weaker near-field amplitude for AuNR-GaAs than for AuNR-SiO_2 is in contrast to our observation of a much stronger scattering intensity for AuNRs on GaAs than for those on silica surfaces. The results of the FDTD simulation displayed in Figure 2.3c shows that the electric field is tightly localized at the AuNR-GaAs interfacial region. This tight electric field localization is significantly different from that observed when the AuNR are supported on the SiO_2 substrate, where the electric field amplitude at the AuNR-SiO_2 interface is comparable to the amplitude on the top surface (AuNR-air interface). This drastically different field localization results in weaker near-field amplitude in the ANSOM data for the AuNRs on the GaAs because the electric field localized at the AuNR-GaAs interfacial region is about 40 nm (the nominal diameter of the AuNRs) away from the near-field probing tip, and it is inaccessible by the ANSOM imaging technique. However, this electric field localization is advantageous for enhancing exciton generation in the GaAs layer very close to the interface and for studying energy transfer and carrier diffusion as discussed next.

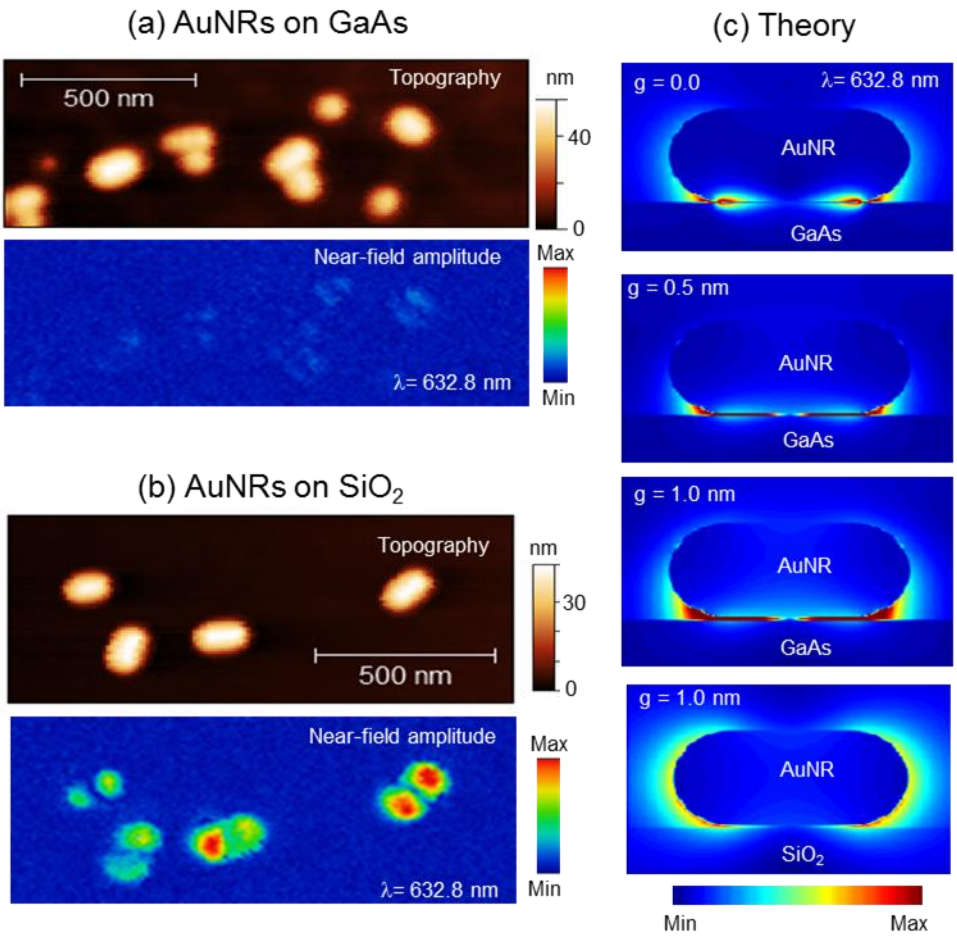

Figure 2.3 (a) Topography and measured near-field amplitude of AuNRs on GaAs surface. (b) Similar to (a) but the AuNRs are supported on silica surface. The results in (a) and (b) are obtained with the same experimental conditions and the near-field amplitudes are scaled to the same maximum. (c) The near-field amplitude calculated on a plane that cuts the AuNR through its center vertically for AuNR-GaAs separation distances of 0.0, 0.5 and 1.0 nm as labeled, compared to the field distribution when the AuNR is supported on a silica surface (bottom most panel). (Scientific reports, 7, 864, 2017)[18]

The PL enhancement/quenching as a function of GaAs thickness *d* is studied by comparing the PL intensity ($I_{InAs/AuNR}$) of the region where the AuNRs are deposited to the intensity (I_{InAs}) of the region where there are no AuNRs. Representative PL spectra of the two regions are compared in Figure. 2.4a considering a 6 nm GaAs thickness. In each case, 15 to 20 spectra are acquired by illuminating different areas in the respective regions, and the spectra with minimum and maximum peak intensities along with the average data are

plotted in Figure. 2.4a. In the absence of the AuNRs, no significant intensity fluctuation is observed as indicated by a standard deviation that is not much larger than the symbols (black triangle, in Figure. 2.4a, indicating the uniformity of the InAs QD number density within the illumination volume. Comparing the red and black curves in Figure. 2.4a, it can be seen that the weakest PL intensity obtained in the presence of the AuNRs is significantly stronger than the highest PL intensity obtained from the region without the AuNRs. The intensity fluctuation for the regions where there are AuNRs (red lines) is due to the difference in the number density and aggregation of AuNRs at different locations. However, this intensity fluctuation is minor considering the spatial variation of the gold nanorod orientation and number density at the nanoscale as shown in Fig. 2.1e. The reproducibility of the relative intensity at different locations is due to a large illumination area that provides statistical representation of the distribution of orientation and aggregation.

Similar comparison as presented in Figure 2.4a has been repeated for $d = 1.5$ nm to 196 nm and the results are discussed in terms of an emission enhancement factor (*EF*) as follows. The *EF* for the samples with different GaAs thicknesses is evaluated independently by calculating the integrated PL intensity ratio as follows.

$$EF = \frac{I_{InAs/AuNR}}{I_{InAs}} \qquad (1)$$

Both the average (black circles) and maximum (red triangles) *EF* values are plotted in Figure 2.4(b). As seen in the figure, the enhancement factor first increases exponentially with decreasing distance until $d = 6$ nm and then decreases rapidly for shorter distances. The general trend is in good agreement with the observation of fluorescence enhancement

and quenching by a gold nanosphere reported by Novotny and co-workers.[15] However, unlike in the previous report (where the spacing medium is air), in our study the emitter and the plasmonic nanostructures are separated by GaAs, whose dielectric and absorption property at the excitation wavelength can change the enhancement mechanism fundamentally. To be noted, the overall enhancement factor is low (maximum ~2.5), because the fraction of area covered by the AuNRs is ~15-20%. We can improve the enhancement factor by dense coverage of AuNRs on our model system. However, we focus on investigating the optical interactions of the plasmon coupled system in our study.

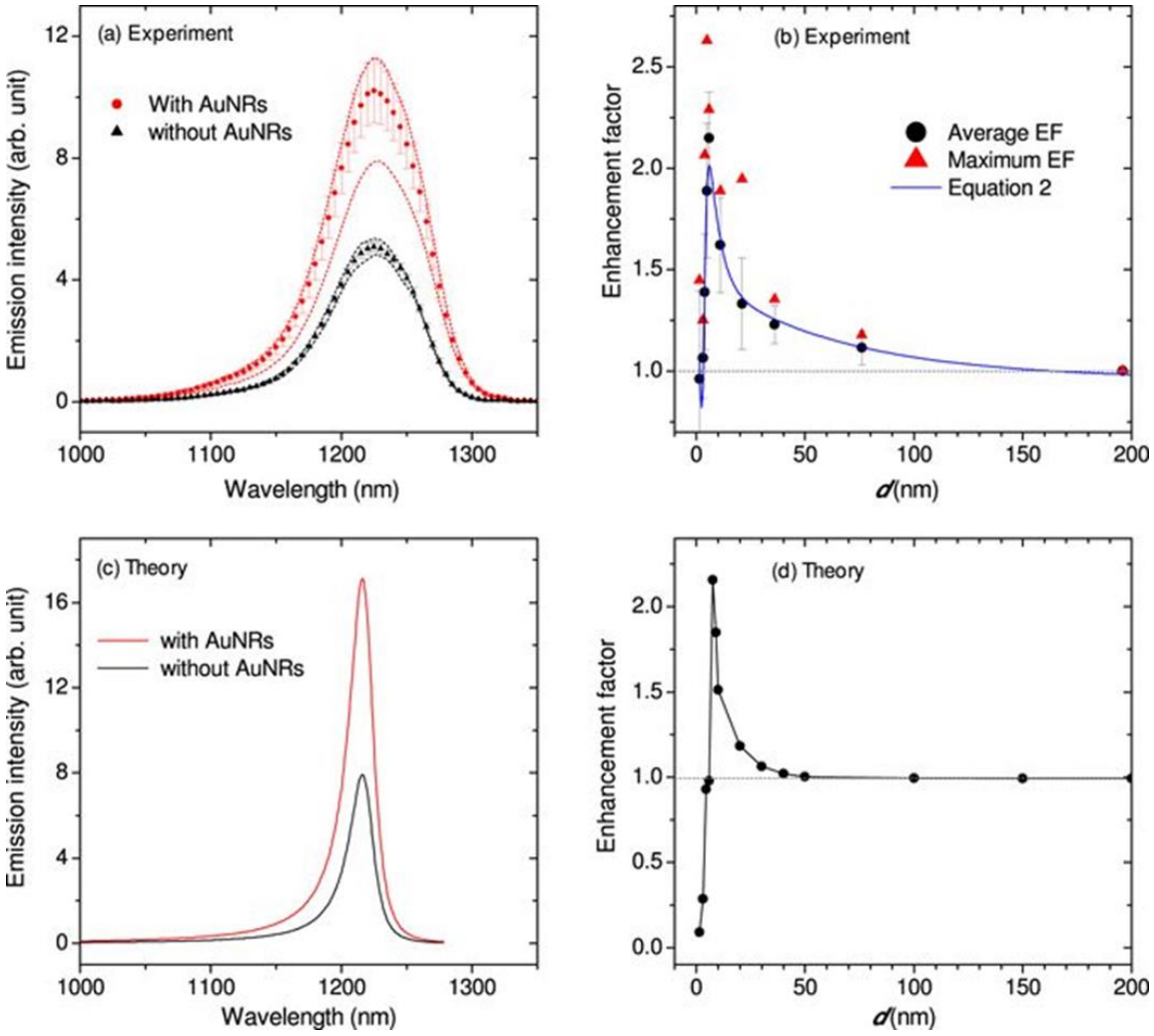

Figure 2.4 Emission enhancement and distance dependence. (a) Photoluminescence acquired from different locations where there are no AuNRs (black lines) and where there are AuNRs (red lines) for 6 nm GaAs thickness (d). (b) Integrated intensity ratio (enhancement factor) as a function of d. The error bars on the average data points (black circles) represent one standard deviation. The maximum enhancement factors (red triangles) represent the ratios of the integrated intensities of the highest intensity spectra obtained in the presence and absence of AuNRs for different GaAs thicknesses. The solid blue line is obtained by fitting equation (2) to the average data. (c) Calculated emission spectra of InAs QDs for d = 7.5 nm in the presence (red line) and absence (black line) of AuNRs. (d) Calculated enhancement factor (ratio of emission intensities) plotted as a function of d. (Scientific reports, 7, 864, 2017)[18]

The results presented in Figure 2.3c indicates a very short decay length of the plasmon near-field into the GaAs, which results in enhanced electron-hole generation close to the AuNR-GaAs interface. Based on the observation in Figure 2.4b and the tight near-field localization at AuNR-GaAs interface, the net emission enhancement is expected to

involve the following distance dependent processes: (i) Förster energy transfer – at short distances, excitation energy transfer from the QDs to the metal surfaces of AuNRs can be the dominant process, which results in reduced emission intensity, (ii) near-field enhanced electron-hole generation inside the InGaAs and efficient carrier capture by the QDs, and (iii) enhanced electron-hole generation at the AuNR-GaAs interface, carrier diffusion through the bulk GaAs and capture by InAs/InGaAs. To extract the length scales of these processes from the experimental enhancement factor (*EF*) presented in Figure 2.4b, we propose the following equation.

$$EF = a_0 + a_1 \frac{d^6}{d^6 + d_0^6} + a_2 e^{-d/D_1} + a_3 e^{-d/D_2} \qquad (2)$$

where a_0 is an arbitrary constant that displaces the theoretical values so that the experimental and theoretical values are plotted on the same scale. The second term is the Förster formula that describes the efficiency of excitation energy quenching at short distances; the third term accounts for the near-field decay length with distance away from the AuNR-GaAs interface; and the fourth term accounts for the net carrier diffusion length (rate of diffusion in the bulk GaAs and capture by the QD). The coefficients a_n $(n = 1 - 3)$ are amplitude adjustment constants. The parameter values $d_0 = 3.9 \pm 0.2$ nm (Förster radius), $D_1 = 4.8 \pm 0.1$ nm (near-field decay length), and $D_2 = 64 \pm 3$ nm (carrier diffusion length) produce a very good fit of Eq. 2 to the average enhancement factor as shown by the blue line in Figure 2.4 (b). It is important to note that the near-field felt by the InGaAs (and hence the electron-hole generation) increases exponentially with decreasing GaAs thickness according to the third term in equation (2). The spacer layer thickness that gives maximum enhancement is determined by the competition between the Forster quenching and the near-field enhancement terms.

The physical relevance of the parameters in equation (2) is further justified by reproducing the observed emission spectra theoretically in the absence and presence of the AuNRs, and accounting for the emission enhancement due to direct near-field excitation of the InAs/InGaAs and due to carrier diffusion as discussed next.

The net emission rate in the illumination area for all the QDs ($\tilde{R}$) results from the competition between the rates of spontaneous emission (R) and excitation energy quenching (Q), and can be calculated as $\tilde{R} = \sigma(R - Q)$, where σ is the areal density of the quantum dots. The net emission spectrum of the quantum dots in the region where the AuNRs are dispersed can be expressed as

$$\frac{d\tilde{R}(\omega)}{d\omega} = \sigma\left\{\eta\left[\frac{dR(\omega)}{d\omega} - \frac{dQ(\omega)}{d\omega}\right] + (1-\eta)\left[\frac{dR^0(\omega)}{d\omega} - \frac{dQ^0(\omega)}{d\omega}\right]\right\} \quad (3)$$

where η is the fraction of the area covered by the AuNRs, and R^0 and Q^0 represent the emission and quenching rates, respectively, of the QDs in the absence of the AuNRs. The details of the calculations are provided in Appendix A. In agreement with the experimental observation, for certain range of GaAs thickness, the theoretical calculation indicates enhanced emission intensity in the presence of AuNRs as illustrated in Figure 2.4c. Plotting the ratio of the peak intensities with respect to the GaAs thickness, the theoretical enhancement factor peaks at d = 7.5 nm as shown in Figure 2.4d, which is in good agreement with the experimental result presented in Figure 2.4b.

As mentioned above, enhanced electron-hole generation at the AuNR-GaAs interface, carrier diffusion through the bulk GaAs, direct excitation of the InGaAs quantum well and carrier capture by the InAs QDs are suggested as key processes that lead to enhanced photon emission by the QDs. Experimental evidence about the

emission enhancement mechanism can be obtained by analyzing the PL intensity dependence on the incident laser power for different thicknesses of GaAs as presented in Figure 2.5 a-c. For a thickness of 1.5 nm, the intensity is lower in the presence of AuNRs because of the dominance of excitation energy transfer from the QD to the metal surface that results in reduced QD PL intensity. However, in both cases (in the absence and presence of AuNRs), the PL intensity increases linearly with the incident laser power as shown in Figure 2.5 a. When the thickness of the GaAs is increased to 4 nm (Figure 2.5b) and 6 nm (Figure 2.5c), the PL intensity in the presence of the AuNR increases with laser power quadratically, while in the absence of the AuNRs, the trend remains linear for all thicknesses. Fitting a second order polynomial equation to the data, it can be seen that the quadratic character increases with increasing GaAs thickness as can be quantified from the relative values of the coefficients shown on the corresponding figures. The probability of photon absorption is proportional to the square of the local electric field inside the metal,[25] which can be contributed to this non-linear dependence of the PL intensity for thicker GaAs capping layer. To notice, maximum enhancement factor is observed for the GaAs thickness 6 nm. The high degree of nonlinear dependence of the PL intensity on laser power for thicker GaAs capping layer clearly indicates that the observed emission enhancement can be attributed to near-field enhanced exciton generation at the AuNR-GaAs interfaces, and direct near-field excitation of InAs/InGaAs. Here, the GaAs capping layer is mediating the exciton-plasmon coupling between the AuNR and InAs QDs through carrier diffusion, capture and recombination processes.

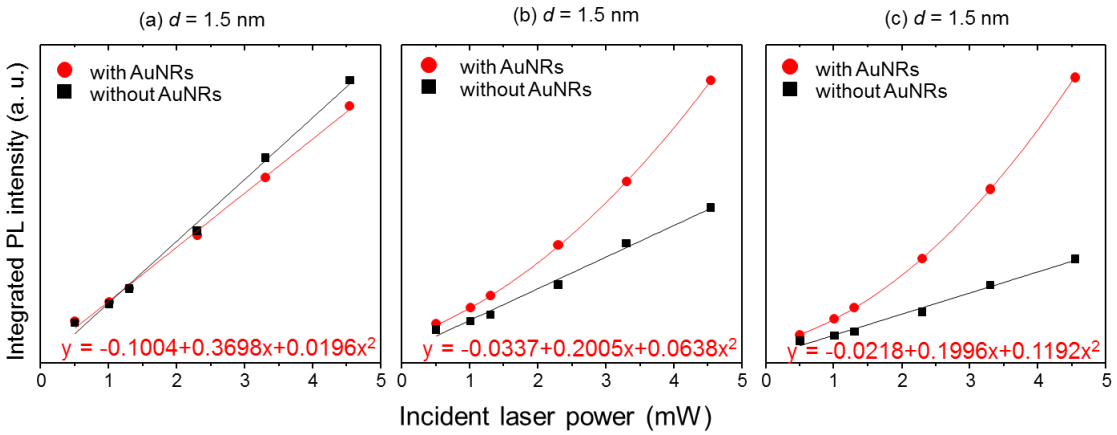

Figure 2.5 Incident laser power dependence and carrier diffusion. PL plotted as a function of laser power for GaAs thicknesses of (a) 1.5 nm, (b) 4 nm, and (c) 6 nm in the presence (red circles) and absence (black squres) of AuNRs. In the absence of the AuNRs, the PL intensity has a linear dependence on the incident power for all GaAs thicknesses. In the presence of the AuNRs, the intensity varies with laser power quadratically, and the degree of nonlinearity increases with the thickness of GaAs as can be seen by comparing the relative values of the coefficients of the linear and the quadratic terms in (a) to (c). (Scientific reports, 7, 864, 2017)[18]

The carrier diffusion and capture processes have been theoretically investigated by describing the temporal evolution of the electron-hole occupation number (N) of the QD excited states using a dynamical equation and including the plasmon near-field effect on the absorption and emission property of the QDs.[21, 22] For the first excited state of a QD, the temporal evolution of the occupation number (N_1) is described as

$$\frac{dN_1^{\alpha}}{\partial t} = \frac{\beta_1(\Omega, \mathrm{t}) I_0(\Omega, d)}{\hbar\Omega} - \mathcal{R}_1(t) + [1 - N_1^{\alpha}(t)]\left[\gamma_1^{\alpha}(t) + \kappa_1^{\alpha}(t) + \sum_{m=2}^{M} \frac{N_m^{\alpha}(t)}{\tau_0}\right] \quad \ldots\ldots\ldots (4)$$

where α represents electrons or holes, Ω is the angular frequency of the incident photons, $I_0(\Omega, d)$ is the electric field intensity experienced by the QD at a thickness d, $\hbar = \frac{h}{2\pi}$ (where h is Planck's constant), β is the absorption coefficient of the QD, $\mathcal{R}$ is the rate of

spontaneous emission, γ and κ are the rate of capturing carriers from the bulk GaAs and the InGaAs well by the QD, respectively, and $m = 1, 2, \ldots, M$ are quantum numbers of all the bound-state energy states. The detail calculations are provided in Appendix A. The capture rates of the carriers by the QD from the bulk GaAs and InGaAs well are plotted as a function of GaAs thickness in Figure 2.6 a and b, respectively. As shown in Figure 2.6 a, the carrier capture rate from the bulk GaAs decreases rapidly for $d < 10$ nm because for this thickness, the contribution of carrier diffusion is insignificant. The electron-hole (e-h) capture rates remain high up to 50 nm and decreases slowly as the thickness increases further, which is in agreement with the experimentally observed broad carrier diffusion profile in GaAs.[28] In contrast, the direct near-field excitation of InGaAs and the electron and hole capture rates increases exponentially as the GaAs thickness decreases as seen in Figure 2.6b. The theoretically calculated result (the trend in Figure 2.6b) justifies the physical relevance of the near-field decay length (D_1) defined in equation (2). Comparing the scales on the y-axes in Figure 2.6a and b, it can be seen that the magnitude of the capture rate from the InGaAs layer is significantly higher than that from the bulk GaAs, suggesting that the apparent emission enhancement trend is mainly determined by the carrier capture rate from the immediate capping layer. However, as shown in Figure 2.4d, the decay length of the emission enhancement is longer than that of the carrier capture rate from the InGaAs layer (Figure 2.6a), indicating that the net enhancement effect results from the contribution of the capture rates from the InGaAs and GaAs layers. Overall, the trend obtained from the theoretical calculations is in accordance with the parameterized equation (2), and further confirms the importance of the carrier capture rates from the InGaAs and GaAs in determining the observed enhanced photon emission by the InAs QDs. We note that the

experimental decay length of the emission enhancement (Figure 2.4b) is longer than that of the theoretical decay length (Figure 2.4d). Our theoretical modeling neglects the capture of carriers by the InGaAs quantum well from the GaAs layer, which becomes significant when direct excitation of the InGaAs quantum well is not dominant. This could enhance the diffusion current in the GaAs layer and slow down the rapid decay of the theoretical *EF* presented in Figure 2.4d.

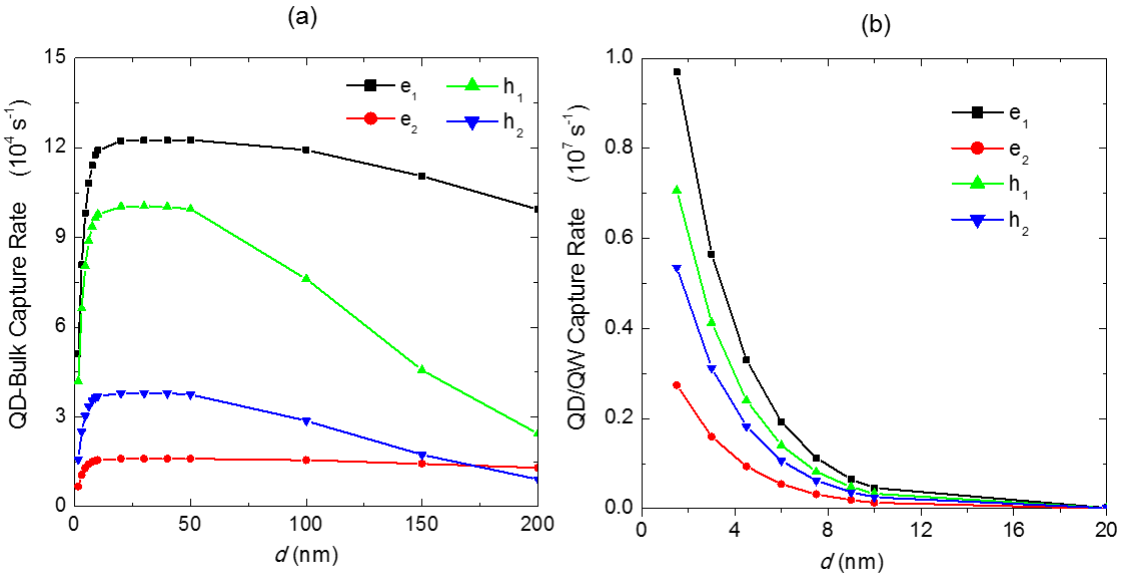

Figure 2.6 (a) Calculated capture rates by two lowest electron (e) and hole (h) energy levels of a QD for surface-photo-excited diffused electrons and holes in GaAs as a function of d. (e) Calculated d-dependence of capture rates by two lowest QD electron/ hole levels for directly photo-excited carriers in InGaAs quantum well. (Scientific reports, 7, 864, 2017)[18]

2.4 Conclusion

In summary, we have presented the first systematic study of enhanced localized exciton generation, carrier diffusion and recombination experimentally and theoretically. Using GaAs as an active mediator of interaction between plasmonic nanostructures and quantum dots embedded in InGaAs quantum well, we have observed a distance dependent emission enhancement that is attributed to enhanced exciton generation at the metal-

semiconductor interfacial regions. The experimental observations are reproduced theoretically describing the temporal evolution of charge carriers in the first and second excited states. The length scales of the near-field enhanced exciton generation, the Förster energy transfer that leads to excitation energy transfer to the metal surface at short distances, the electron and hole captures rates by the quantum dots from the bulk GaAs and InGaAs well are determined. The result presented here has a potential for opening new research directions and may lead to improved detection efficiency using the optical properties of particle plasmons.

References

1. Curto, A. G. *et al.* Unidirectional Emission of a Quantum Dot Coupled to a Nanoantenna. *Science* **329**, 930 (2010).

2. Fedutik, Y., Temnov, V. V., Schöps, O., Woggon, U. & Artemyev, M. V. Exciton-Plasmon-Photon Conversion in Plasmonic Nanostructures. *Phys. Rev. Lett.* **99**, 136802 (2007).

3. Akimov, A. V. *et al.* Generation of single optical plasmons in metallic nanowires coupled to quantum dots. *Nature* **450**, 402 (2007).

4. Zhang, W., Govorov, A. O. & Bryant, G. W. Semiconductor-Metal Nanoparticle Molecules: Hybrid Excitons and the Nonlinear Fano Effect. *Phys. Rev. Lett.* **97**, 146804 (2006).

5. Atwater, H. A. & Polman, A. Plasmonics for improved photovoltaic devices. *Nature Materials* **9**, 205 (2010).

6. Pillai, S. & Green, M. A. Plasmonics for photovoltaic applications. *Solar Energy Materials and Solar Cells* **94**, 1481–1486 (2010).

7. Arinze, E. S., Qiu, B., Nyirjesy, G. & Thon, S. M. Plasmonic Nanoparticle Enhancement of Solution-Processed Solar Cells: Practical Limits and Opportunities. *ACS Photonics* **3**, 158–173 (2016).

8. Chang, C.-C. *et al.* A Surface Plasmon Enhanced Infrared Photodetector Based on InAs Quantum Dots. *Nano Lett.* **10**, 1704–1709 (2010).

9. Miao, J. *et al.* Surface Plasmon-Enhanced Photodetection in Few Layer MoS2 Phototransistors with Au Nanostructure Arrays. *Small* **11**, 2392–2398 (2015).

10. Lee, S. C., Kang, J. H., Park, Q.-H., Krishna, S. & Brueck, S. R. J. Oscillatory penetration of near-fields in plasmonic excitation at metal-dielectric interfaces. *Scientific Reports* **6**, 24400 (2016).

11. Lee, S. C., Krishna, S. & Brueck, S. R. J. Quantum dot infrared photodetector enhanced by surface plasma wave excitation. *Opt. Express* **17**, 23160–23168 (2009).

12. Zhou, N. *et al.* Plasmon-enhanced light harvesting: applications in enhanced photocatalysis, photodynamic therapy and photovoltaics. *RSC Adv.* **5**, 29076–29097 (2015).

13. Fei, J. & Li, J. Controlled Preparation of Porous TiO2–Ag Nanostructures through Supramolecular Assembly for Plasmon-Enhanced Photocatalysis. *Advanced Materials* **27**, 314–319 (2014).

14. Pompa, P. P. *et al.* Metal-enhanced fluorescence of colloidal nanocrystals with nanoscale control. *Nature Nanotechnology* **1**, 126 (2006).

15. Anger, P., Bharadwaj, P. & Novotny, L. Enhancement and Quenching of Single-Molecule Fluorescence. *Phys. Rev. Lett.* **96**, 113002 (2006).

16. Runyu Liu and Puminun Vasinajindakaw and Guiru Gu and Jarrod Vaillancourt and Xuejun Lu. Optimizing light absorption in quantum dot infrared photodetectors by tuning surface confinement of surface plasmonic waves. *Journal of Physics D: Applied Physics* **46**, 015102 (2013).

17. Ebbesen, T. W., Lezec, H. J., Ghaemi, H. F., Thio, T. & Wolff, P. A. Extraordinary optical transmission through sub-wavelength hole arrays. *Nature* **391**, 667 (1998).

18. Haq, S. *et al.* Active Mediation of Plasmon Enhanced Localized Exciton Generation, Carrier Diffusion and Enhanced Photon Emission. *Scientific Reports* **7**, 864 (2017).

19. Habteyes, T. G. Direct Near-Field Observation of Orientation-Dependent Optical Response of Gold Nanorods. *J. Phys. Chem. C* **118**, 9119–9127 (2014).

20. Chen, H. *et al.* Observation of the Fano Resonance in Gold Nanorods Supported on High-Dielectric-Constant Substrates. *ACS Nano* **5**, 6754–6763 (2011).

21. Aspnes, D. E., Kelso, S. M., Logan, R. A. & Bhat, R. Optical properties of AlxGa1−x As. *Journal of Applied Physics* **60**, 754–767 (1986).

22. Wu, Y. & Nordlander, P. Finite-Difference Time-Domain Modeling of the Optical Properties of Nanoparticles near Dielectric Substrates. *J. Phys. Chem. C* **114**, 7302–7307 (2010).

23. Kiesow, K. I., Dhuey, S. & Habteyes, T. G. Mapping near-field localization in plasmonic optical nanoantennas with 10 nm spatial resolution. *Appl. Phys. Lett.* **105**, 053105 (2014).

24. Habteyes, T. G., Dhuey, S., Kiesow, K. I. & Vold, A. Probe-sample optical interaction: size and wavelength dependence in localized plasmon near-field imaging. *Opt. Express* **21**, 21607–21617 (2013).

25. Brongersma, M. L., Halas, N. J. & Nordlander, P. Plasmon-induced hot carrier science and technology. *Nature Nanotechnology* **10**, 25 (2015).

26. Huang, D. & Alsing, P. M. Many-body effects on optical carrier cooling in intrinsic semiconductors at low lattice temperatures. *Phys. Rev. B* **78**, 035206 (2008).

27. Huang, D. *et al.* Controlling quantum-dot light absorption and emission by a surface-plasmon field. *Opt. Express* **22**, 27576–27605 (2014).

28. Bieker, S., Kiessling, T., Ossau, W. & Molenkamp, L. W. Correct determination of low-temperature free-exciton diffusion profiles in GaAs. *Phys. Rev. B* **92**, 121201 (2015).

Chapter 3

Temperature and distance dependence of plasmon enhanced carrier generation and photoluminescence of dot-in-a-well semiconductor

Abstract

Here, the distance dependent photoluminescence (PL) in the near-infrared from InAs quantum dots (QDs) embedded in a strained $In_{0.15}Ga_{0.85}As$/GaAs quantum well (QW) has been investigated systematically. Then, the effect of localized surface plasmon resonances on enhancing carrier generation and photon emission is studied by analyzing the temperature dependence of the QDs' PL coupled to the plasmonic colloidal gold nanorods (AuNRs) through the GaAs capping layer. The temperature is varied from 20 K to room temperature for the two representative samples of the GaAs thicknesses of 6 nm and 76 nm. PL intensity enhancement factor (EF) of about 20 fold is experimentally determined at 200 K for the GaAs thickness of 6 nm, as a consequence of near-field enhanced absorption and carrier generation. The EF attains maxima with increasing temperature, which can be attributed to the competition between radiative and nonradiative carrier recombination processes.

3.1 Introduction

The extensive recent research effort in nano-plasmonics has been motivated by the potential for an outstanding diverse array of applications. Examples of such applications include biological spectroscopy in drastically reduced volumes,[1, 2] surface enhanced

spectroscopy,[3] near-field optical microscopy with unprecedented resolution,[4,5] photodetectors,[6–10] solar cells[11,12] and many other photonic and optoelectronic devices.[13] This expanding list of plasmonic applications, makes it necessary to have fundamental understanding about plasmon coupled system to control and engineer the plasmon response on the nanoscale that may open completely new possibilities in material science, communications, biochemistry and medicine. Understanding the temperature dependence of optical properties of plasmon coupled system is a precondition for the development of such applications, as plasmonic excitations are very sensitive to the variation of temperatures. The distance dependent plasmonic effect on the PL properties of the GaAs capped InAs QDs at 77 K has been reported.[14] Another report has been demonstrated the distance dependence of plasmon coupled InAs/GaAs QDs chains by measuring time-resolved and polarization-resolved PL at 10 K.[15] But these studies are restricted to a certain temperature, and the intensive analysis are not provided. In our previous study,[16] plasmon enhanced exciton generation, carrier diffusion, and carrier capture for InAs/InGaAa/GaAs QDs as discussed in Chapter 2 is examined by monitoring the QDs' PL intensity at room temperature. Systematic investigation of distance dependent temperature effect on photocarrier absorption and photon emission for plasmon coupled InAs/InGaAs/GaAs dot-in-a-well (DWELL) structure has not been reported yet, hence the interaction has not been completely understood for the coupled system.

In this chapter, we probe the coupling between localized surface plasmon and InAs QDs, by analyzing the temperature and distance dependent PL of the QDs in the near-infrared region. The temperature dependence is investigated varying the range 20 K to 290 K for the plasmon coupled InAs QDs embedded in an $In_{0.15}Ga_{0.85}As$/GaAs QW structure.

The effect of localized surface plasmon resonance on enhancing the photoabsorption and photon emission is investigated as a function of temperature for the DWELL structure, where colloidal AuNRs are used as plasmonic probes. This temperature dependent plasmonic effect on EF is examined for the representative samples of the GaAs thickness of 6 and 76 nm. These two samples are chosen, so that clear contrast can be studied for the plasmonic effect of direct near-field excitation (6 nm, strong plasmon coupling) and carrier diffusion (76 nm, weak plasmon coupling). The distance dependent properties of the DWELL heterostructures are also inspected by measuring the PL of the QDs without plasmonic structure at room temperature.

3.2 Sample fabrication and preparation

The layout for the coupling of the InAs/InGaAs/GaAs DWELL structure to the plasmonic AuNRs is shown in Figure 3.1 (a). The samples with different GaAs capping layer thickness (d) are grown using a molecular beam epitaxy (MBE) reactor on epi-ready semi-insulating GaAs (001) substrate. The bottom 200 nm smoothing GaAs layer is grown at 580 ^{o}C on GaAs (001) substrates, after desorption of the native oxide layer thermally at 630 ^{o}C for 20 minutes. The InAs/InGaAs and the 1.5 nm GaAs cold cap layers are grown at 475 ^{o}C, followed by growth of additional high-temperature GaAs layer of different thicknesses at 580 ^{o}C. Here, the total thickness of the GaAs capping layer = d, indicates total cap including both thin cold cap and high-temperature cap.

Commercially obtained gold nanorod solution (Nanopartz Inc.) is centrifuged and re-suspended in water to remove the excess surfactants. Then the AuNRs are dispersed on the GaAs capping layer surface by drop casting. The AuNRs are applied only on some

portion of the sample (covering ~15-20% of the sample), so that PL intensity can be compared by recording the PL spectra from the two regions-with and without AuNRs.

3.3 Optical measurements

The room temperature PL measurement for InAs/InGaAs/GaAs with different capping layer thicknesses without plasmonic structure is acquired by employing a conventional lock-in technique. Modulated HeNe laser pump with a wavelength of 632.8 nm (average power of 5 mW, and intensity of 0.16 W/cm^2) is used to excite the samples. Emission is dispersed by a 0.3 m grating monochromator and detected using a 2153 femtowatt InGaAs photoreceiver from Newport with wavelength range: 800-1700 nm.

For the low temperature PL measurement, the plasmon coupled InAs/InGaAs/GaAs sample is mounted on a cryostat chamber (CTI-Cryogenics, Model 22), two stage, closed-cycle helium refrigeration system. The schematic of the optical layout of the temperature-dependent PL measurement is shown in Figure 3.1. The temperature can be varied from 10 K to room temperature at user defined interval. The temperature-dependent PL setup is automatically controlled by developing LabVIEW program in-house. The photoluminescence signals are acquired at 10 K interval allowing 5 minutes to stabilize the temperature after each temperature change. The accuracy of temperature is within 0.2 K. The pump wavelength of 633 nm (1.96 eV) is above the GaAs bandgap for all temperatures within our measurement range. The PL spectra are obtained using conventional lock-in technique utilizing 50 cm focal length monochromator (ARC SpectraPro-500). The samples are excited using HeNe laser of wavelength, λ = 633 nm, at an incident angle of 10 degree with respect to the surface normal. The excitation light is focused using 0.2 NA

lens to a spot size of 400 μm as determined by knife-edge method. The PL signal is collected using the same lens and detected by IR femtowatt photoreceiver (New Focus, Inc., model 2153)

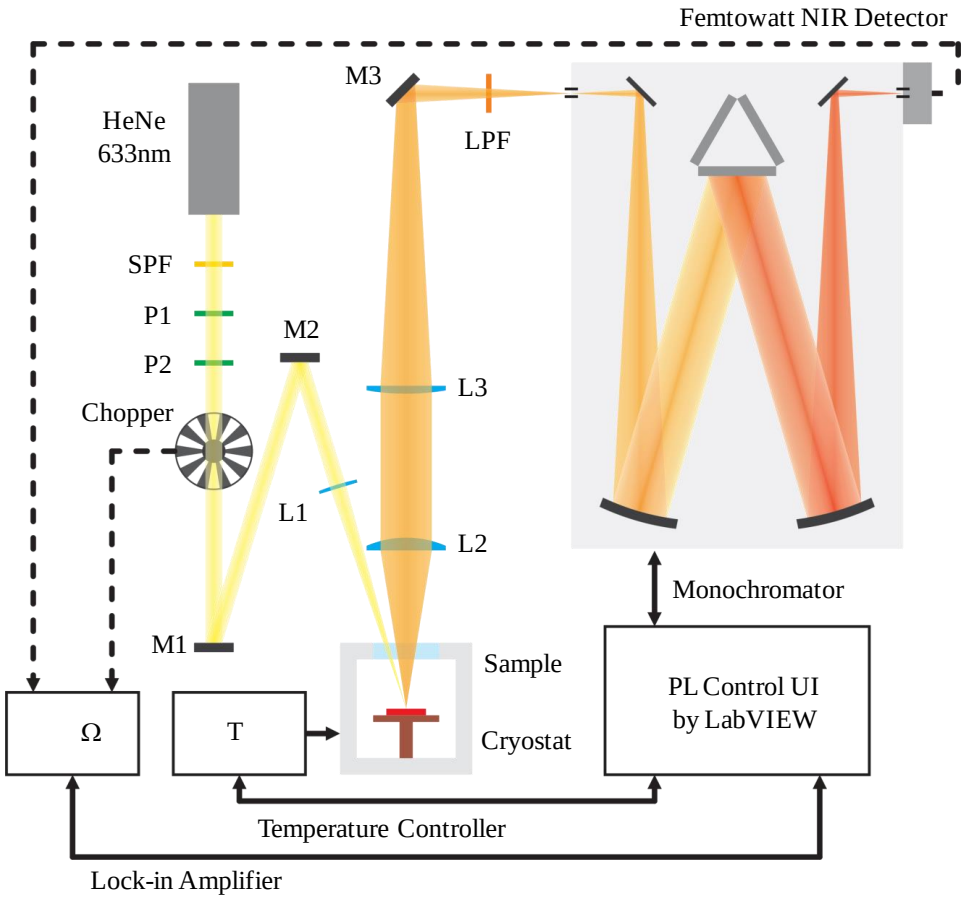

Figure 3.1 Schematic of the optical layout of the temperature-dependent PL measurement. SPF ≡ shortpass filter; P1, P2 ≡ polarizers; L1, L2, L3 ≡ lens; M1, M2, M3 = mirrors; LPF ≡ longpass filter.

The dark-field scattering intensity of the single Au nanorods and the aggregated Au nanorods are measured using a GX51 Olympus microscope objective of numerical aperture of 0.9. The AuNRs are excited with 100W halogen lamp white light source. The dark-field microscopy and spectroscopy setup is explained in detail with the schematic in Chapter 5.

3.4 Electromagnetic simulation

The electromagnetic simulation is carried out using finite-difference time domain (FDTD) method, which is implemented using a commercial software package (Lumerical Solutions, Inc.). A total-field scattered field source scheme is used to introduce light energy into the simulation region, where the grid size is 0.5 nm for all x-, y- and z-axes.

3.5 Results and discussion

3.5.1 Plasmon enhanced absorption by overlapping excitation and plasmon resonance

In this work, epitaxially grown InAs QDs confined in higher band gap InGaAs/GaAs quantum well is chosen as model excitonic system (like in Chapter 2). A schematic of the coupling geometry of the DWELL structure with a colloidal gold nanorod is shown in Figure. 3.2a. The emission wavelength of the quantum dot peaks in the near-infrared region ($\lambda \approx 1200$ nm) at room temperature. The size of the AuNRs (40 × 80 nm) is chosen so that the plasmon resonance overlaps with the excitation wavelength ($\lambda = 633$ nm). That is, the plasmonic effect enhances the absorption of light energy inside the InGaAs and GaAs capping layers, but there is no spectral overlap between the plasmon resonances of the AuNRs and the emission wavelength of the QDs (Figure 3.2c). When the plasmonic nanoparticles are excited on the high-index GaAs substrate, the near-field is tightly localized at the particle-substrate interface (shown in Figure. 3.2b), which is determined by the surface ligands coated around the colloidal AuNRs. As a result, exciton generation is enhanced at the AuNR-GaAs interface. This tight near-field localization is utilized to enhance the direct excitation of InAs/InGaAs, and carrier generation and

diffusion in GaAs, which causes PL intensity enhancement. Therefore, the plasmonic effect on the PL intensity of the InAs QDs depends on the GaAs capping layer thickness (d).

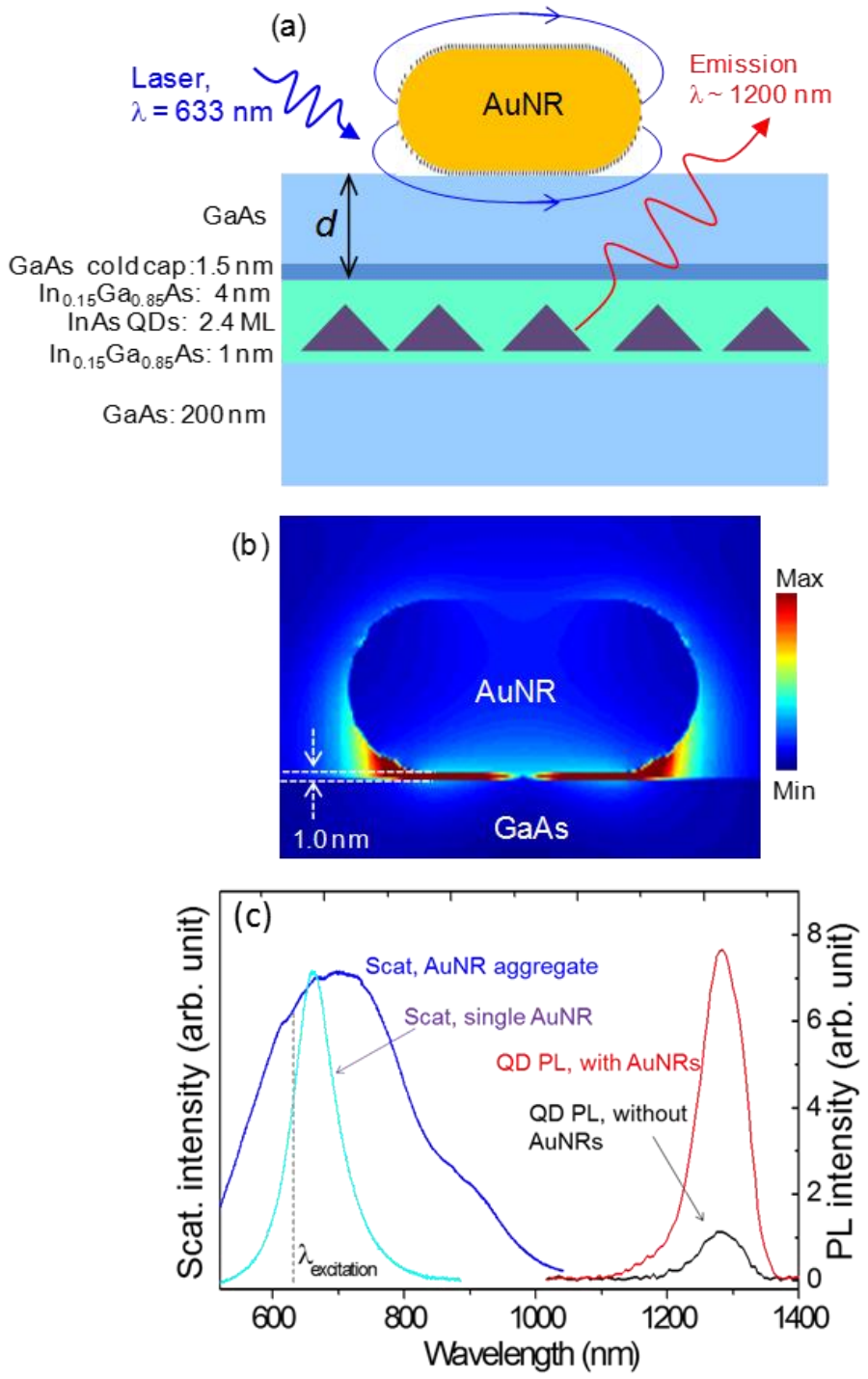

Figure 3.2 (a) Schematic of the DWELL semiconductor structure coupled to colloidal plasmonic gold nanorod. (b) FDTD simulation result showing the near-field localization at the AuNR-GaAs interface for 1 nm gap due to surfactants. (c) The scattering of the single particle (cyan line) and aggregates (blue line) of AuNRs showing the plasmon resonance overlaps with the 633 nm excitation laser line (indicated by the vertical dashed line) but not with the DWELL emission in the absence (black line) and presence (red lines) of the AuNRs.

3.5.2 Room temperature optical characterization without plasmonic structure

The distance dependent optical properties of the InAs/InGaAs/GaAs DWELL structure is studied monitoring the PL of the QDs as a function of GaAs thickness (d). The PL is measured at room temperature by varying the GaAs capping layer thickness, d = 1.5 nm to 196 nm without adding the AuNRs (schematic shown in Figure 3.3a) keeping the measurement condition constant for all samples. The excitation wavelength 633 nm with an average power of 5 mW and power density of 0.16 W/cm^2 is used. Working with a low power density avoids saturation of the QDs' ground state. The PL for different GaAs capping layer thicknesses are shown in Figure. 3.3b. Red-shift is observed with decreasing the GaAs capping layer thickness from 21 nm to 1.5 nm (Figure 3.3b, c). The red-shifting is more pronounced for the thickness less than 11 nm. This red-shift is attributed to strain in InAs QDs due to the GaAs capping layer. Effective QD size increases as a result of strain driven surface kinetics that leads to partial decomposition of the InGaAs during the growth due to preferential integration of In at existing InAs QDs.[8, 9] Thus increasing size alters electronic potential causes red-shifting. With thickness less than 11 nm, the strain has more impact on QD size as observed in Figure 3.3b, c. Red-shift is also observed when the GaAs capping layer thickness increases above 21 nm, which is noticeable for 76 nm. There is an energy shift of 12.86 meV from GaAs thickness d = 21 nm (1037.65 meV) to d = 76 nm (1024.79 meV). Probably, this red-shifting is attributed to relief of some strain inside the QD as the capping layer is thick enough for the strain relaxation.

The FWHM/linewidth of the PL as a function of GaAs capping layer thickness, d is plotted in Figure 3.3d. The linewidth values for different GaAs thicknesses are extracted by fitting the Gaussian function to the PL spectra. We observe, the FWHM increases as the

GaAs capping layer thickness reduces from d = 36 nm to d = 1.5 nm. The lowest linewidth of 45.71 meV is attained for the thickness of d = 36 nm. The linewidth increases about 11% (5 meV) with the reduction of GaAs thickness from d = 36 nm to11 nm. An abrupt increase of linewidth is detected in Figure 3.3d when the thickness, d reduces below 11 nm. The linewidth increases about 42% (from the minimum value) when the thickness reduces to 6 nm. Subsequent large broadening of the linewidth is observed as the thickness, d reduces further below 6 nm. To be precise, for d = 6 nm and 4 nm, measured FWHM are 65.51 meV and 74.08 meV, respectively which is raised by 8.57 meV for the reduction of 2 nm GaAs thickness. As we know, the increased total strain induced by decreasing the GaAs capping layer thickness can degrade the optical properties due to the formation of dislocations or the dissolution of the quantum dot structure.[17] Thus, increased strain in thinner GaAs capping layer causes to increase the FWHM as d reduces from 36 nm to 1.5 nm. Maximum broadening of about 92 % (FWHM 87.56 meV) is observed with the thinnest (d = 1.5 nm) GaAs capping layer, since with this thickness of the GaAs layer, the uniformity of quantum dot structure is highly disrupted. In Figure 3.3d-c, broadening of linewidth is also noticed with the increment of the GaAs thickness above 36 nm along with red-shift. For d = 76 nm and 196 nm, linewidth broadening of about 28% and 49% is observed, respectively. Since, carriers travel a longer distance in these thicker GaAs layer and encounter dislocations or impurities. The lower values of the FWHM for the samples of d = 36 nm, 21 nm and 11 nm testify the higher quality of self-assembled InAs QD structures, while larger values of the FWHM for d = 1.5 nm and 3 nm indicate a substantial QD size dispersion.

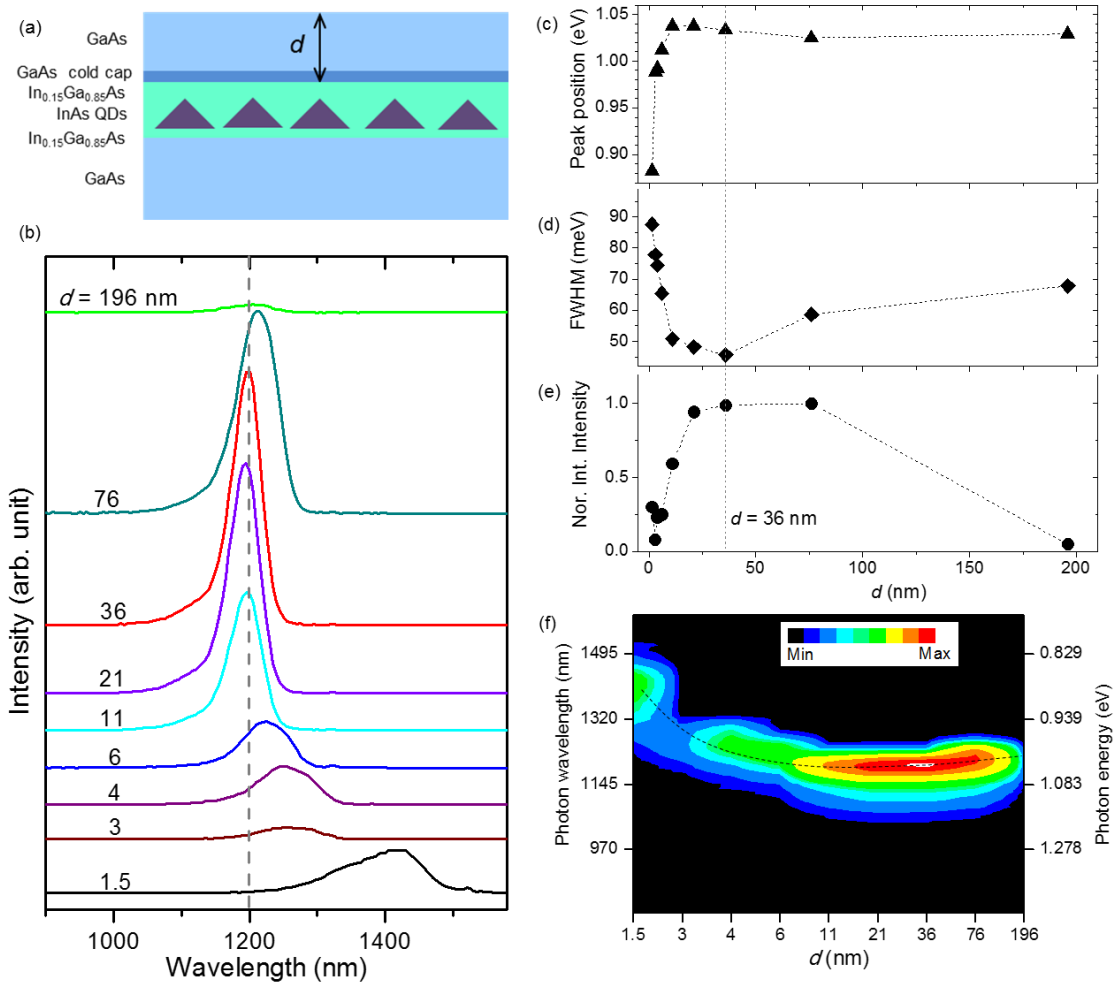

Figure 3.3 Room temperature characteristics without plasmonic structure (a) Schematic of the DWELL semiconductor structure (b) PL spectra for different GaAs capping layer thicknesses as labeled in the plot. Vertical dashed line indicates emission wavelength at maximum intensity with narrowest linewidth. (c) Emission energy (d) FWHM and (e) Normalized integrated intensity, as a function of GaAs capping layer thickness, d. Vertical dotted line indicates all corresponding values for the thickness, d = 36 nm. (f) PL intensity map as a function of GaAs capping layer thickness, d. Black dashed line is for guiding our eyes to follow the change in emission energy.

To investigate the DWELL structure further at room temperature without adding plasmonic nanoparticles, the normalized integrated PL intensity and the PL intensity map as a function of GaAs thickness, d is shown in Figure 3.3e and 3.3f, respectively. Highest intensity is observed for the GaAs thickness, d = 36 nm. We notice, intensity is fairly close for d = 76 nm, 36 nm and 21 nm. Intensity drops with decreasing GaAs thickness below

36 nm. In our previous report,[16] it is shown that the carrier capture rate by QDs from the bulk GaAs decreases rapidly for d <10 nm because diffusion of carriers shrinks significantly for thinner GaAs thickness. Therefore, the PL intensity severely decreased for d <10 nm, which is observed in Figure 3.2 e-f. The intensity also drops for d = 176 nm, as this distance is far away from the carrier diffusion length calculated ~64 nm in our previous work, [16] which is in good agreement with the experimentally observed exciton diffusion profile in GaAs.[19] Since, carriers may capture by impurities or annihilated by non-radiative decay when crossing across thicker GaAs capping layer, therefore the intensity drops.

3.5.3 Temperature and distance dependent optical properties of the plasmon coupled system

Plasmonic effect on optical properties of the InAs/InGaAs/GaAs DWELL structure depends on the GaAs capping layer thickness because of the near-field localization at the AuNR-GaAs interface. In this section, we will discuss about the temperature dependent plasmonic effect of the DWELL structure for the GaAs thickness of 6 nm and 76 nm, and compare their responses.

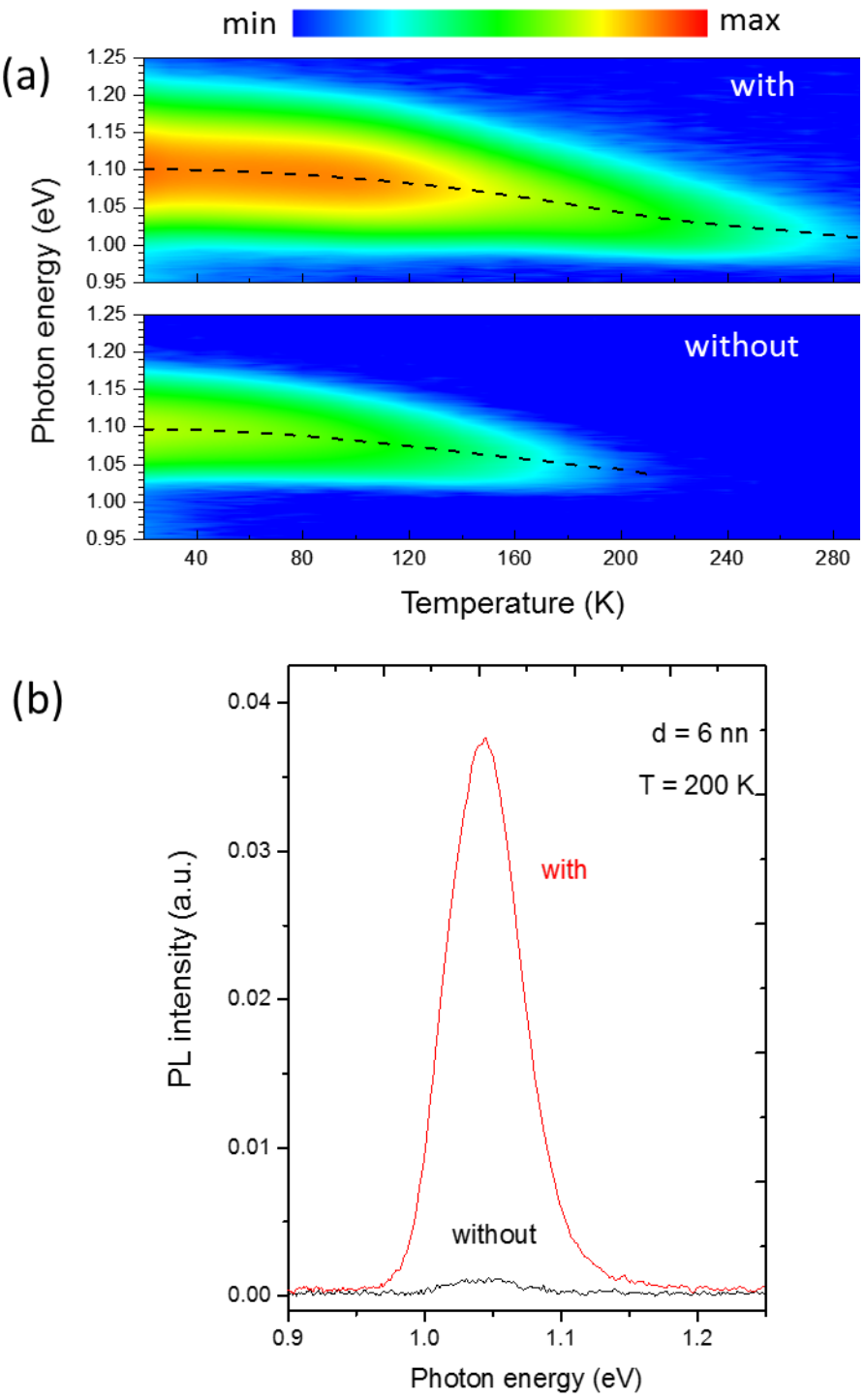

Figure 3.4 Temperature dependence of the plasmonic DWELL structure for the GaAs capping layer thickness of 6 nm at 0.68 W/cm^2 excitation energy. (a) PL intensity map with (top) and without (bottom) AuNRs. Dashed black lines indicate the change of peak emission energy with temperature. (b) Representative Photoluminescence of the system with (red line) and without (black line) AuNRs at 200 K.

Comparing the PL intensity map as a function of temperature in Figure 3.4a with (top) and without (bottom) AuNRs as well as the representative spectra in Figure 3.4b, acquired at 0.68 W/cm^2 excitation intensity, we see the plasmonic AuNRs enhance the PL intensity of the DWELL system radically for a GaAs thickness of d = 6 nm. The plasmonic effect extends the temperature range of the PL detection limit as can be seen comparing the intensity maps in Figure 3.4a. A strong plasmonic effect is observed for the thickness of 6 nm because of tight near-field confinement at the AuNR-GaAs interface that ensures appreciable photocarrier absorption in the InGaAs layer as well as in the GaAs barrier, as a result InAs QDs emission enhances.

For detail quantitative analysis, the integral PL (IPL) intensities acquired with (red circle) and without (black square) the plasmonic AuNRs for d = 6 nm are plotted as a function of temperature as shown in Figure 3.5a. As both types of recombination- radiative and non-radiative increase with increasing temperature,[20] therefore at a certain temperature, there is always a competition between radiative and non-radiative recombination, and the PL intensity dictates which type of recombination dominates. We observe, the IPL intensity decreases with increasing temperature for both with and without the plasmonic effect (Figure 3.5a), which is attributed to thermal quenching.[21, 22] In the case of the plasmonic effect, IPL intensity reduction at low temperature is extremely slow comparing without plasmonic effect. Because of proximity, the tight coupling between the plasmonic AuNRs and the InAs QD emitters, ensures appreciable direct capture of carriers in the InGaAs layer as well as in the GaAs barrier. This direct carrier capture in InGaAs quantum well along with carriers excited in GaAs enhance carrier confinement into QD emitters, as a result radiative recombination increases. We notice an inflection point in the

IPL intensity plot with AuNRs as a function of temperature, which is attributed to carrier diffusion that increases with temperature.

The plasmonic effect of the DWELL structure on the PL intensity could be better understood when the PL enhancement factor (IPL intensity ratio- with and without AuNRs) is plotted as a function of temperature as shown in Figure 3.5b. We notice, two peaks appear in enhancement factor curve. Using the Gaussian function to fit these peaks in the enchantment factor, we obtain the peak value at 128 ± 5 K and 200 ± 2 K for d = 6 nm. At lower temperature, there is rapid exponential increment of the enhancement factor (from ~6 to ~16) up to ~128 K. This can be attributed to direct carrier capture and carrier diffusion as mentioned earlier that increase with temperature. In this temperature region, the non-radiative recombination is less effective in the presence of AuNRs for d = 6 nm. To be noted, the enhancement peak at ~128 K corresponds to the inflection point of the IPL intensity as mentioned above. If the temperature increases further then a slow exponential increment (from ~16 to ~20) is observed from ~128 K up to ~200 K. For the DWELL structure, thermal escape of carries occurs from QW to GaAs barrier, and also from QDs to QW.[21,23,24] To be mentioned, the energy barrier is lower for QW-GaAs than QD-QW.[21] Increment of enchantment factor slows down above 128 K, which can be attributed to thermal escape of carriers from QW to GaAs barrier that undergo subsequent non-radiative recombination. As it is known that with increasing temperature the non-radiative recombination sites saturate due to increased carrier concentration.[25] Therefore, a sharp rise of enhancement factor is observed again with increasing temperature (peak appears at ~200 K) as a consequence of saturation of the non-radiative sites with increasing carrier concentration. This indicates that radiative recombination dominates up to this peak

temperature value of ~200 K where the maximum enhancement factor of ~20 is observed. After that the enhancement factor decreases promptly with increasing temperature. This can be contributed to thermal escape of carriers from QDs and subsequent non-radiative recombination as well as exciton dissociation in InAs QDs. At that point thermal equilibrium is reached, and carrier confinement to QDs decreases significantly with increasing temperature.[21,24,26] Moreover, with increasing temperature, the thermal energy approaches the exciton binding energy in InAs QD (~20 meV, corresponding to thermal energy ~232K).[26] Therefore, exciton dissociation can take place reducing the carrier confinement into the InAs QDs. As a result, non-radiative recombination takes over at temperature higher than ~200 K. This point is indicated by vertical blue dashed line as shown in Figure 3.5.

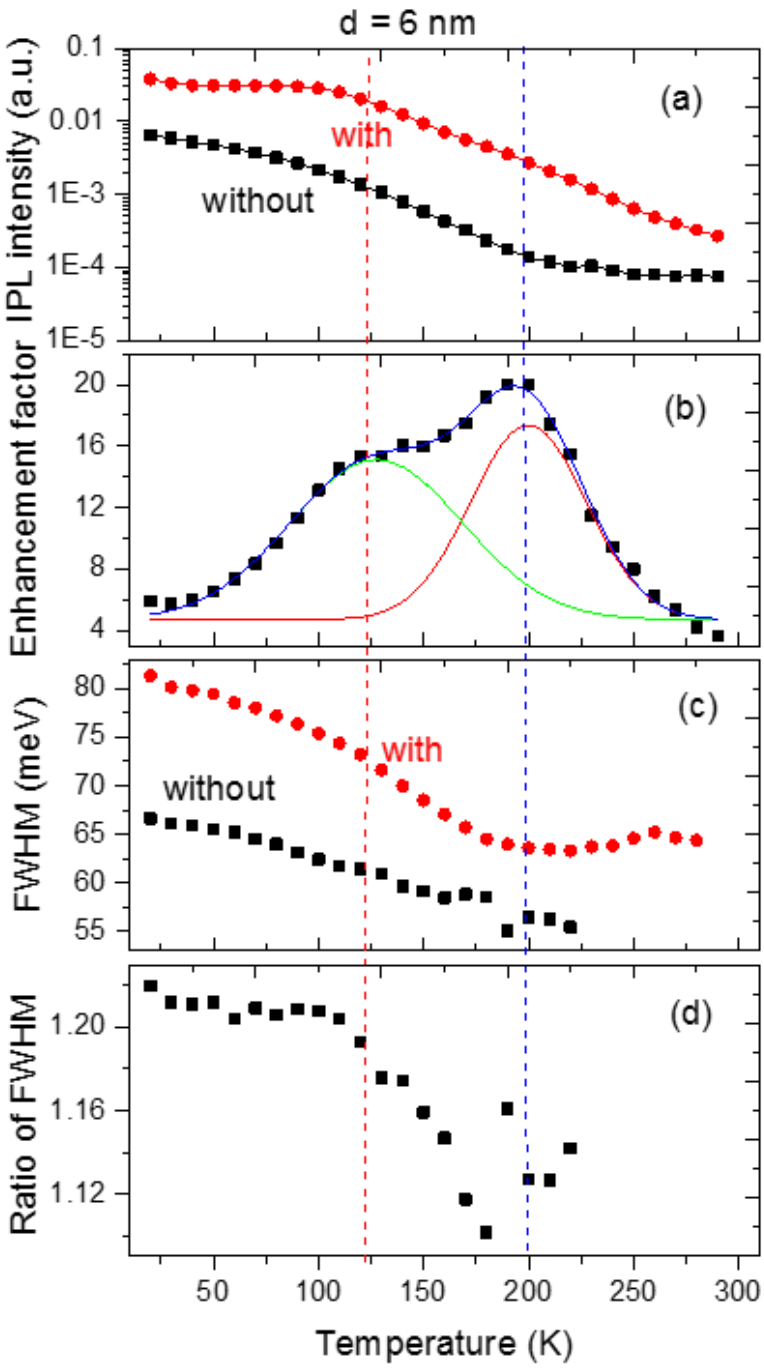

Figure 3.5 Temperature dependent plasmonic effect on DWELL structure for the GaAs capping layer thickness (d) of 6 nm at 0.68 W/cm^2 excitation intensity. (a) Integral PL intensity in logarithmic scale as a function of temperature (b) enhancement factor expressed as ratio of IPL with and without AuNRs. Fitting the Gaussian function indicates the enhancement factor peaks at 128 $\pm$ 5 K (solid green line) and at 200 $\pm$ 2 K (red solid line). (c) FWHM of the PL spectra with (red circle) and without (black square) AuNRs. The FWHM values are extracted from the PL spectra by fitting the Gaussian function. (d) Ratio of FWHM (with AuNRs and without AuNRs) as a function of temperature.

To extract further insight into the plasmonic effect of DWELL structure, the FWHM/linewidth acquired from the PL spectra by fitting Gaussian function is plotted as a function of temperature as shown in Figure 3.5c. It is obvious that with plasmonic effect FWHM broadens remarkably for all temperatures for d = 6 nm. For an example, at 20 K, the FWHM with AuNRs is ~82 meV, and without AuNRs is ~66.5 meV that leads linewidth broadening of ~23% with the plasmonic effect. This plasmon-induced linewidth broadening can result from increased carrier concentration in the presence of plasmonic AuNRs.[27, 28] The influence of plasmons on the FWHM is expressed as ratio of FWHM with plasmonic AuNRs and without AuNRs as shown in Figure 3.5d. We observe, the ratio of FWHM is almost constant at lower temperature until the inflection point (~128 K) is reached, indicated as red dashed vertical line in Figure 3.5. After crossing the inflection point, the ratio of FWHM decreases with increasing temperature as a result of decreasing carrier confinement into the QDs, because of losing carriers due to thermal effect. There is a slight increase of the ratio at ~200 K, which can be attributed to exciton dissociation in InAs QDs as mentioned earlier as well as carrier-phonon interaction.[26, 28]

To compare the interpretation as explained above, similar analysis is repeated for the GaAs capping layer thickness d = 76 nm. Because the AuNRs are far away from the InAs QDs, which is far beyond the near-field confinement regime, the coupling is extremely weak. As a result, the plasmonic effect on the InAs QDs system for d = 76 nm is insignificant. Studying the PL intensity map as a function of temperature for d = 76 nm shown in Figure 3.6a with (top) and without (bottom) AuNRs along with the representative spectra at 200 K in Figure 3.6b acquired at 0.28 W/cm^2 excitation intensity, we observe the plasmonic effect is not pronounced for the DWELL system. For this thicker GaAs cap,

the influence of AuNRs on InAs QD emitter is not significant. The minor change is observed in presence of AuNRs due to excess carrier generation at the interface between GaAs and AuNRs, but most of them vanish during diffusion through the GaAs capping layer for travelling longer distance. Therefore, overall the carrier confinement into the InAs QDs with plasmonic effect increases very smaller amount at higher temperature.

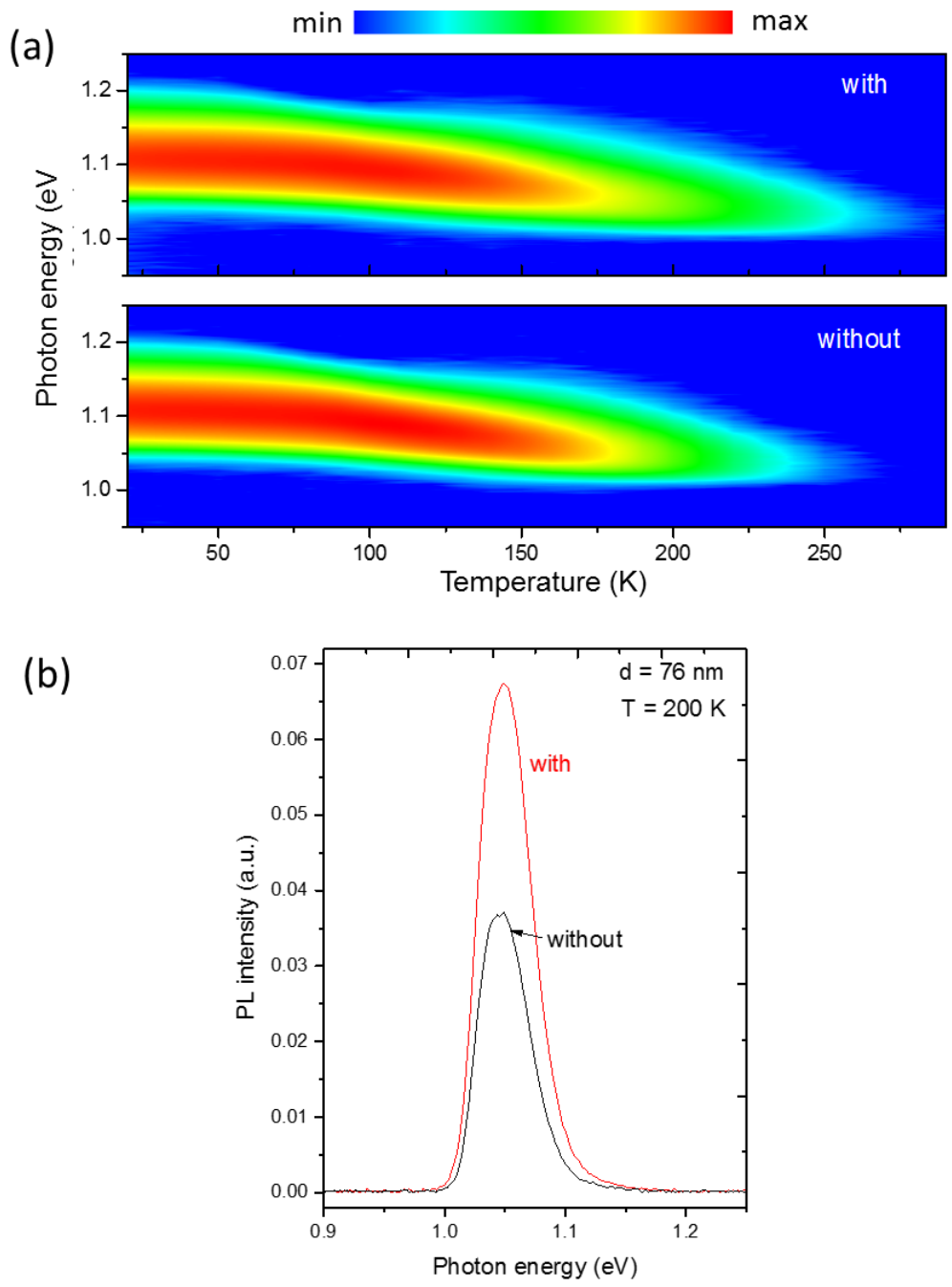

Figure 3.6 Temperature dependence of the plasmonic DWELL structure for the GaAs capping layer thickness (d) of 76 nm at 0.28 W/cm^2 excitation energy. (a) PL intensity map with (top) and without (bottom) AuNRs. (b) Representative Photoluminescence of the system with (red line) and without (black line) AuNRs at 200 K.

As shown in Figure 3.7a, the IPL intensity for d = 76 nm obtained at 0.28 W/cm^2 excitation intensity with (red circle) and without (black square) the AuNRs are very close. The slight increase in the IPL intensity with plasmonic effect is attributed to increased photocarrier absorption at the AuNR-GaAs interface. But most of the carriers annihilated by the non-radiative recombination sites when crossing this large thickness, and very few carriers generated in the GaAs barrier in the presence of AuNRs are able to confine into the QDs to emit. In addition to that, plasmonic effect of direct near-field excitation of the InGaAs layer is not effective, because of large capping layer thickness. Therefore, overall the PL intensity enhancement with plasmonic effect is very low for d = 76 nm.

The enhancement factor as a function of temperature is plotted in Figure 3.7b for d = 76 nm. As can be seen, the highest enhancement factor is observed ~2.8, which is much smaller than the value of ~20 observed for d = 6 nm, because of the increase of the GaAs capping layer thickness from 6 to 76 nm. Here, two peaks are also observed similar to the results at d = 6 nm. At lower temperature wide peak at 68 ± 4 K, and another peak at higher temperature at 233.5 ± 0.5 K, are extracted by fitting the Gaussian function to the enhancement factor curve. In contrast, the lower temperature peak appears at ~128 K (EF value of ~16), and the higher temperature peak appears at ~200 K (EF value of ~20) for the GaAs capping layer thickness of 6 nm. As we mentioned earlier, for d = 76 nm, there is no plasmonic effect on direct excitation of carriers in the InGaAs QW, and also plasmonic effect on carrier confinement into the InAs QDs from the GaAs barrier decreases because of the increase of the GaAs thickness, therefore very small enhancement factor value of ~1.6 at ~68 K is achieved at lower temperature. Besides, the enhancement factor increases very slowly at lower temperature, which is attributed to carrier diffusion that

increases with temperature. If the temperature increases further then the enhancement factor decreases slowly approaching towards unity, which can be attributed to exciton dissociation in the GaAs layer. The exciton binding energy in the GaAs semiconductor is 4.2 meV corresponding to the thermal energy of ~49 K.[30] Therefore, exciton dissociation can take place in the GaAs capping layer above 68 K, and the fraction of free electrons/holes, instead of excitons (electron-hole pairs), are diffused through the GaAs capping layer reducing the carrier confinement into the QDs. Another possibility of this trend might be related to the presence of defects in proximity to the QDs, acting as channels for non-radiative recombination of carriers escaping from QDs with increasing temperature.[25, 26] The enhancement factor approaches to unity with increasing temperature which can be attributed to thermal escape of carriers from the InGaAs QW and go through non-radiative recombinations. As the carrier generation and emission do not increase significantly with the plasmonic effect for d = 76 nm, hence the enhancement factor severely affected by all these non-radiative recombination processes. In case of the GaAs thickness of 6 nm, the carrier generation and emission enhance significantly with plasmonic effect, therefore radiative recombination dominates mostly upto the temperature ~200 K, and the dip does not appear in EF as observed for d = 76 nm. The EF reaches minimum (~1.1) at ~160 K, which is attributed to saturation of non-radiative recombination sites with increasing carrier concentration with increasing temperature. Once the non-radiative recombination sites saturate, the enhancement factor begins to increase again with increasing temperature. Now, the increased carrier concentration with increasing temperature can contribute to radiative recombination to dominate till the maxima of EF appears at temperature 233.5 ± 0.6 K. A falloff in the enhancement factor is observed again

with increasing temperature further as the non-radiative recombination starts to dominate indicated by the blue dashed vertical line in Figure 3.7. This reduction of EF is attributed to thermal escape of carriers from InAs QDs to QW as well as exciton dissociation in InAs QDs as mentioned earlier. The falloff in enhancement factor after 233.5 ± 0.6 K is sharp (relatively slower decay for d = 6 nm) because the plasmonic effect does not enhance PL intensity significantly. As a result, losing carrier confinement with subsequent non-radiative recombination severely impacts the EF. The enhancement factor peak temperature shifts at ~233 K compared to ~200 K for d = 6 nm. This shift of the enhancement factor peak temperature is attributed to the suppression of the non-radiative recombination processes with increasing capping layer.

The competition between radiative and non-radiative recombination, can be better understood if we investigate the plasmonic effect on the FWHM as a function of temperature as plotted in Figure 3.7c, d. We observe, the FWHM with and without plasmonic effect remains unchanged at lower temperature. That means spectral broadening is negligible at low temperature regime in the presence of AuNRs as the increment of carrier concentratio is insignificant due to weak coupling. The ratio of the FWHM with and without AuNRs is plotted in Figure 3.7d shows constant value towards unity with increasing temperature until the non-radiative recombination dominates. The ratio of the linewidth increases when the non-radiative recombination processes start to dominate above ~68 K because of exciton dissociation in the GaAs, the presence of defects nearby QDs, and escaping carriers from QDs due to thermal effect as mentioned above, and is indicated by the red dashed vertical line in Figure 3.7. This ratio attains maxima at ~125 K where the linewidth broadening is ~3 meV (6%) with plasmonic effect compared to 23%

broadening at 20 K for d = 6 nm. Then, the ratio decreases to lower value as the carrier concentration decreases with temperature due to thermal effect, which is also observed for d = 6 nm (Figure 3.5d). The FWHM with plasmonic effect is getting narrower at higher temperature (above ~230 K) as shown in Figure 3.7c, because of the reduction of carrier confinement. The plasmon-induced linewidth broadening is significantly smaller for 76 nm compared to 6 nm, which is attributed to reduced plasmonic enhancement effect on non-radiative recombination rates as well as less carrier generation due to weak coupling between plasmonic AuNRs and InAs emitters.

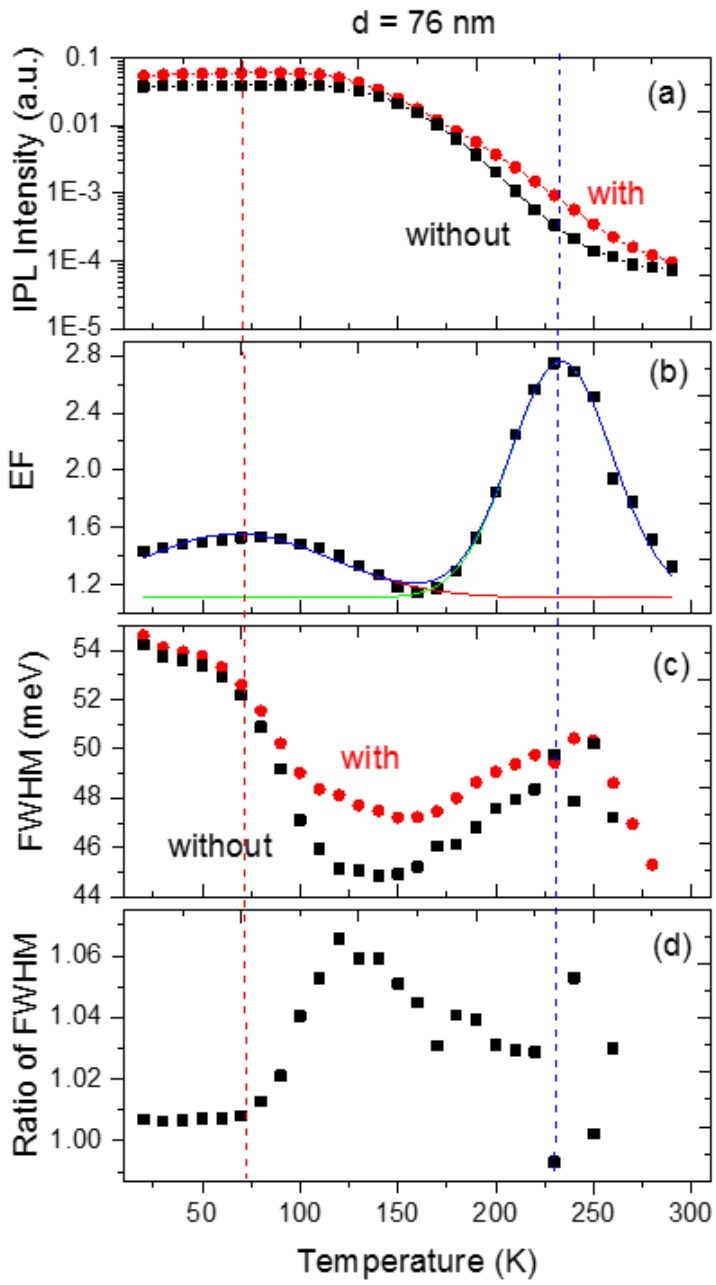

Figure 3.7 Temperature dependent plasmonic effect on DWELL structure for GaAs capping layer thickness d = 76 nm at 0.28 W/cm2 excitation intensity. (a) Integral PL intensity in logarithmic scale as a function of temperature (b) enhancement factor expressed as ratio of IPL with and without AuNRs. Fitting the Gaussian function indicates the enhancement factor peaks appear at 68 ± 4 K (solid red line) and at 233.5 ± 0.6 K (green solid line). (c) FWHM of the PL spectra with (red circle) and without (black square) AuNRs. FWHM values are extracted from the PL spectra by fitting Gaussian function. (d) Ratio of FWHM as a function of temperature.

In the discussion so far, there is a distinct plasmonic effect for d = 6 nm and d = 76 nm because of diverse coupling strength in between AuNRs and InAs QDs emitter. The overall enhancement factor is higher for d = 6 nm (highest value ~20) comparing with d = 76 nm (highest value ~2.8). Even at 20 K the enhancement factor ~6 is obtained for d = 6 nm, which is higher than the highest enhancement factor (~2.8) attained for d = 76 nm. This is attributed to strong coupling between the InAs emitter and the AuNRs due to proximity of near field confinement. As a result, the radiative recombination wins over the non-radiative recombination mostly because of generation and confinement of huge carrier concentration in the presence of plasmonic structure. The plasmonic effect on carrier generation and confinement is attributed to both- direct carrier capture into InGaAs and carrier diffusion from GaAs barrier. In case of d = 76 nm, the direct carrier capture to InGaAs in presence of AuNRs is not operative, and a mild coupling exists between plasmonic structure and InAs emitter as observed in enhancement factor.

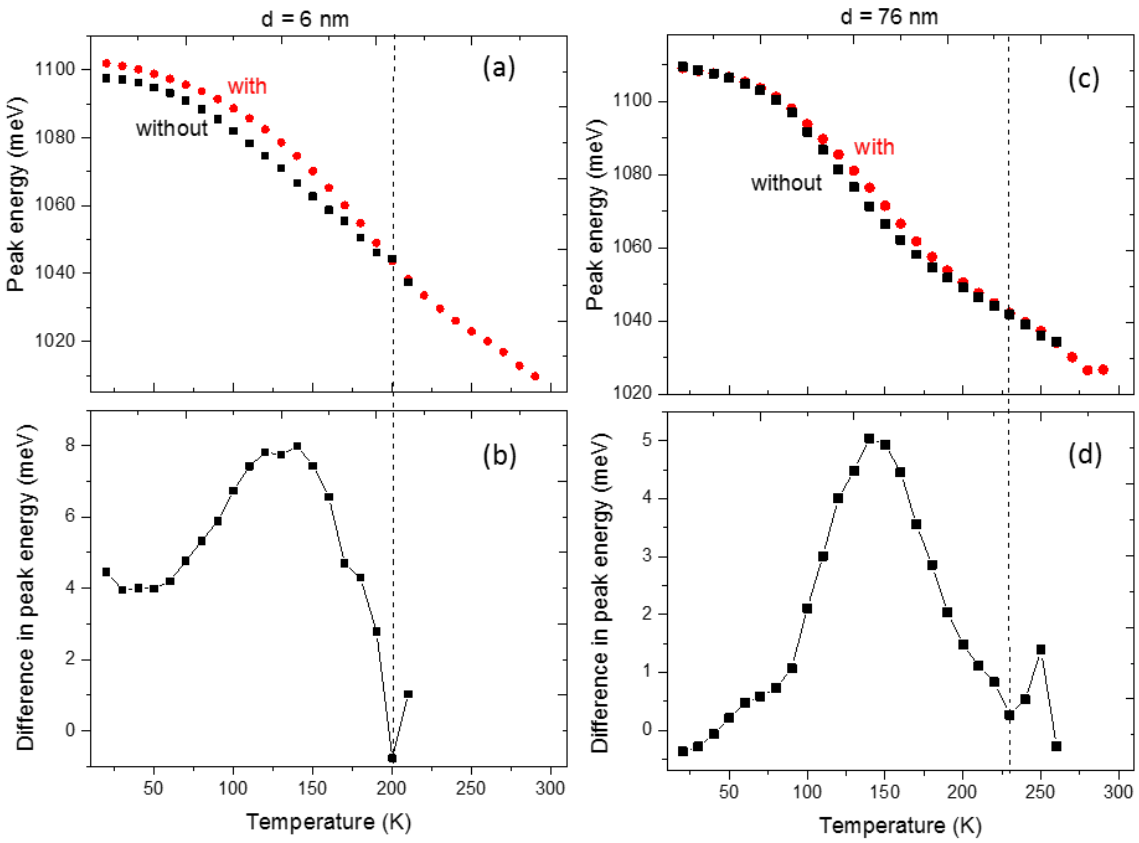

Figure 3.8 Temperature dependence of PL energy (a) peak energy for d = 6 nm with AuNRs (red circle) and without AuNRs (black square) (b) difference in the PL peak energy with AuNRs and without AuNRs for d = 6 nm (c) peak energy for d = 76 nm with AuNRs (red circle) and without AuNRs (black square) (d) difference in PL peak energy with AuNRs and without AuNRs for d = 76 nm

We also investigate emission peak energy with and without plasmonic AuNRs, hence plotted as a function of temperature in Figure 3.8a and c, for d = 6 nm and 76 nm, respectively. For both GaAs capping layer thicknesses, with and without AuNRs, the overall emission energy red shifted with temperature because of bandgap narrowing that originates from electron-phonon interaction and thermal expansion,[33,34] and the thermal escape of carriers from QDs and recaptured by the lower energy QDs with increasing temperature.[24] For d = 6 nm, the emission energy blue-shifts with plasmonic effect until the non-radiative recombination dominates as discussed earlier, which is indicated by the

vertical dashed line in Figure 3.8a. The difference of emission peak energy with AuNRs and without AuNRs is plotted as a function of temperature in Figure 3.8b for d = 6 nm, where we observe, emission energy peak rises by ~4.5 meV at 20 K and keeps rising to maximum value of ~8 meV at ~128 K in presence of AuNRs. To be noticed, the deflection point in the IPL intensity plot with plasmonic effect due to carrier diffusion appears at ~128 K. Then the difference in peak energy decreases rapidly and hits towards minimum at ~200 K where there is almost no difference in peak energy with AuNRs and without AuNRs. We notice, peak energy difference keeps increasing with increasing carrier concentration at lower temperature up to ~128 K, and then this value decreasing since reducing carrier confinement with increasing temperature. This blue-shift of peak emission energy in presence of AuNRs is attributed to Moss-Burstein effect which causes shift of optical absorption to higher energy due to carrier confinement with increasing carrier concentration.[28,35–37]

In contrast with strong plasmonic coupling for d = 6 nm, PL peak energies for d = 76 nm with and without AuNRs are almost the same at lower energy as shown in Figure 3.8c and d. There is a rise of peak energy with plasmonic effect as the carrier concentration increases with increasing temperature. The maximum energy shifting towards higher energy is ~5 meV at around 128 K shown in Figure 3.8d. The difference decreases rapidly with reducing the carriers due to thermal escape and the difference becomes negligible at ~230 K where non-radiative recombination starts to dominate as indicated by the vertical dashed line in Figure 3.8d. This observation also noticed for d = 6 nm which is due to Moss-Burstein effect as mentioned earlier. The maximum value for the difference in peak energy is observed at around the same temperature (~128 K) for d = 6 nm and 76 nm. This

indicates, with plasmonic effect higher carrier concentration is attained at that temperature due to carrier diffusion.

3.6 Conclusions

Temperature dependent photocarrier dynamics has been investigated for III-V semiconductor DWELL structure using colloidal gold nanorods as plasmonic structure. We have studied photoluminescence intensity, enhancement factor, carrier confinement, linewidth, and emission energy peak for InAs/InGaAs/GaAs QDs under the influence of strong local field due to plasmonic AuNRs as a function of temperature. PL intensity increases significantly for strong near-filed plasmon coupled system because of increased carrier absorption in InGaAs and GaAs layer. Due to strong coupling, the enhancement factor increases continually until the non-radiative recombination dominates because of thermal escape of carriers. In the enhancement factor two peaks appear due to the domination of radiative recombination. These two peaks correspond to carriers escaping from InGaAs to GaAs barrier at lower temperate, and carriers escaping from InAs QDs to InGaAs well at higher temperature where radiative recombination still dominates. Therefore, carrier confinement reduces with increasing temperature causes to win non-radiative recombination over radiative one. Significant linewidth broadening is observed in all temperatures in case of strongly coupled plasmonic system, which is attributed to increased carrier concentration with plasmonic effect. It is also noticed that plasmonic effect introduces blue-shift in the emission peak energy, which is due to Moss-Burstein effect that originates from carrier confinement with increasing carrier concentration. These insights into photo excited carrier dynamics can be useful for plasmonic device fabrication, and for future directions of research.

References

1. Kneipp, K. *et al.* Single Molecule Detection Using Surface-Enhanced Raman Scattering (SERS). *Phys Rev Lett* **78**, 1667–1670 (1997).

2. Nie, S. & Emory, S. R. Probing Single Molecules and Single Nanoparticles by Surface-Enhanced Raman Scattering. *Science* **275**, 1102 (1997).

3. Willets, K. A. & Van Duyne, R. P. Localized Surface Plasmon Resonance Spectroscopy and Sensing. *Annu. Rev. Phys. Chem.* **58**, 267–297 (2007).

4. Novotny, L. & Hecht, B. *Principles of Nano-Optics*. (Cambridge University Press, 2006). doi:10.1017/CBO9780511813535

5. Kalkbrenner, T. *et al.* Optical Microscopy via Spectral Modifications of a Nanoantenna. *Phys Rev Lett* **95**, 200801 (2005).

6. Quantum selection rule dependent plasmonic enhancement in quantum dot infrared photodetectors. *J. Appl. Phys.* **119**, 193103 (2016).

7. Mojaverian, N., Gu, G. & Lu, X. A plasmonic dipole optical antenna coupled quantum dot infrared photodetector. *J. Phys. Appl. Phys.* **48**, 475102 (2015).

8. Two-dimensional metallic square-hole array for enhancement of mid-wavelength infrared photodetection. *Opt. Quantum Electron.* **48**, (2016).

9. Wavelength tuning of surface plasmon coupled quantum well infrared photodetectors. *Opt. Express* **26**, 552 (2018).

10. Miao, J. *et al.* Surface Plasmon-Enhanced Photodetection in Few Layer MoS2 Phototransistors with Au Nanostructure Arrays. *Small* **11**, 2392–2398 (2015).

11. Atwater, H. A. & Polman, A. Plasmonics for improved photovoltaic devices. *Nat. Mater.* **9**, 205 (2010).

12. Arinze, E. S., Qiu, B., Nyirjesy, G. & Thon, S. M. Plasmonic Nanoparticle Enhancement of Solution-Processed Solar Cells: Practical Limits and Opportunities. *ACS Photonics* **3**, 158–173 (2016).

13. S. A. Maier. Plasmonics: The Promise of Highly Integrated Optical Devices. *IEEE J. Sel. Top. Quantum Electron.* **12**, 1671–1677 (2006).

14. Wu, J. *et al. Photoluminescence plasmonic enhancement in InAs quantum dots coupled to gold nanoparticle*. **65**, (2011).

15. Hakkarainen, T. *et al.* Site-controlled InAs quantum dot chains coupled to surface plasmons. *Optica* **3**, 139–142 (2016).

16. Haq, S. *et al.* Active Mediation of Plasmon Enhanced Localized Exciton Generation, Carrier Diffusion and Enhanced Photon Emission. *Sci. Rep.* **7**, 864 (2017).

17. Schumann, O. *et al.* Effects of strain and confinement on the emission wavelength of InAs quantum dots due to a $\mathrmGa\mathrmAs_1\ensuremath-x\mathrmN_x$ capping layer. *Phys Rev B* **71**, 245316 (2005).

18. Maximov, M. V. *et al.* Tuning quantum dot properties by activated phase separation of an InGa(Al)As alloy grown on InAs stressors. *Phys Rev B* **62**, 16671–16680 (2000).

19. Bieker, S., Kiessling, T., Ossau, W. & Molenkamp, L. W. Correct determination of low-temperature free-exciton diffusion profiles in GaAs. *Phys Rev B* **92**, 121201 (2015).

20. Bharadwaj, P. & Novotny, L. Robustness of Quantum Dot Power-Law Blinking. *Nano Lett.* **11**, 2137–2141 (2011).

21. Torchynska, T. V. *et al.* Thermal activation of excitons in asymmetric InAs dots-in-a-well InxGa1−xAs⁄GaAs structures. *J. Appl. Phys.* **101**, 024323 (2007).

22. Songmuang, R., Kiravittaya, S., Sawadsaringkarn, M., Panyakeow, S. & Schmidt, O. G. Photoluminescence investigation of low-temperature capped self-assembled InAs/GaAs quantum dots. *Proc. Twelfth Int. Conf. Mol. Beam Epitaxy* **251**, 166–171 (2003).

23. Seravalli, L. *et al.* Quantum dot strain engineering of InAs⁄InGaAs nanostructures. *J. Appl. Phys.* **101**, 024313 (2007).

24. Dan P Popescu and Peter G Eliseev and Andreas Stintz and Kevin J Malloy. Temperature dependence of the photoluminescence emission from InAs quantum dots in a strained Ga 0.85 In 0.15 As quantum well. *Semicond. Sci. Technol.* **19**, 33 (2004).

25. Lambkin, J. D., Dunstan, D. J., Homewood, K. P., Howard, L. K. & Emeny, M. T. Thermal quenching of the photoluminescence of InGaAs/GaAs and InGaAs/AlGaAs strained-layer quantum wells. *Appl. Phys. Lett.* **57**, 1986–1988 (1990).

26. Heitz, R., Mukhametzhanov, I., Madhukar, A., Hoffmann, A. & Bimberg, D. Temperature dependent optical properties of self-organized InAs/GaAs quantum dots. *J. Electron. Mater.* **28**, 520–527 (1999).

27. Yoshimura, H., Bauer, G. E. W. & Sakaki, H. Carrier-induced shift and broadening of optical spectra in an $\mathrmAl_\mathrmx$$\mathrmGa_1\mathrm\ensuremath-\mathrmx$As/GaAs quantum well with a gate electrode. *Phys Rev B* **38**, 10791–10797 (1988).

28. Ullrich, B., Wang, J. S. & Brown, G. J. Photoluminescence under high-electric field of PbS quantum dots. *AIP Adv.* **2**, 042132 (2012).

29. Le-Van, Q. *et al.* Temperature dependence of quantum dot fluorescence assisted by plasmonic nanoantennas. *Phys Rev B* **91**, 085412 (2015).

30. Nam, S. B. *et al.* Free-exciton energy spectrum in GaAs. *Phys Rev B* **13**, 761–767 (1976).

31. Mazzucato, S. *et al.* Defect passivation in strain engineered InAs/(InGa)As quantum dots. *Curr. Trends Nanosci. - Mater. Appl. Proc. Eur. Mater. Res. Soc. 2004 - Symp. G* **25**, 830–834 (2005).

32. Seravalli, L. *et al.* Quantum dot strain engineering of InAs⁄InGaAs nanostructures. *J. Appl. Phys.* **101**, 024313 (2007).

33. Fan, H. Y. Temperature Dependence of the Energy Gap in Semiconductors. *Phys Rev* **82**, 900–905 (1951).

34. Varshni, Y. P. Temperature dependence of the energy gap in semiconductors. *Physica* **34**, 149–154 (1967).

35. Yogamalar, N. R. & Chandra Bose, A. Burstein–Moss shift and room temperature near-band-edge luminescence in lithium-doped zinc oxide. *Appl. Phys. A* **103**, 33–42 (2011).

36. T S Moss. The Interpretation of the Properties of Indium Antimonide. *Proc. Phys. Soc. Sect. B* **67**, 775 (1954).

37. Burstein, E. Anomalous Optical Absorption Limit in InSb. *Phys Rev* **93**, 632–633 (1954).

Chapter 4

Optimization of spacer layer thickness between plasmonic structure and III-V semiconductor

Abstract

Optimization of spacer layer thickness with nanometer scale is vital for the development of plasmonic devices. In this work, we focus on optimization of spacer layer thickness between plasmonic gold nanorods and III-V semiconductor InAs/InGaAs/GaAs dot-in-a-well structure. To do that, we emphasize on optimization of spacer between the gold nanorods and the top layer of the semiconductor heterostructure that is GaAs. Organic and inorganic both type of spacer layer has been utilized to control the thickness.

4.1 Introduction

Plasmon enhanced carrier dynamics through GaAs as an active mediator at room temperature is discussed in Chapter 2 for the semiconductor heterostructure InAs/InGaAs/GaAs. In the dark-field microscope image, we observed green, yellow, orange, and red doughnut shape gold nanorods (AuNRs) when placed directly on the GaAs substrate as discussed in Chapter 2 (Figure 2.2a). We explained this color variation is attributed to distance variation due to the amount of surface ligands cetyl trimethylammonium bromide (CTAB) coated around the gold nanorods. Green particles correspond to direct contact of the AuNRs with the GaAs substrate, and yellow to red depends upon proximity to the substrate.[1] In the dark–field image, most of the AuNRs are

green. When we measured the scattering spectra from different color AuNRs, we observe green AuNRs have multiple peaks with very low intensity. The red particles with farthest proximity from the GaAs substrate have sharp single scattering spectra with high intensity (~10 times higher than the green particles). This indicates, field confinement is larger in the case of the red particles, and reduces significantly for the green particles. As we know, the characteristics of a plasmon resonance are determined by the shape, size, and orientation, material properties of the nanoparticle as well as by the dielectric environment in which the nanoparticle is located.[2–5] The changes of the plasmonic response of the nanoparticle become strong when a thin spacer layers on the nanometer scale are used, as the field enhancement is particularly large in the gap between nanoparticle and film.[6–9] This implies, controlling or optimization of the coupling distance is vital for taking the advantage of field confinement, as the energy/charge transfer can take place reducing the field enhancement if the gap is not optimized.[1, 10]

Therefore, we can improve the plasmon coupled system if the green doughnut shape particles in the dark-field image can be minimized, and the red particles can be maximized. To do that, an ultra-thin spacer layer is required with precise control in-between AuNRs and GaAs i.e. at the AuNR-GaAs interface. To achieve this goal, we deposit different types of spacer layers both organic and inorganic and try to control the thickness with nanometer accuracy. Here, we demonstrate all the deposition techniques we tried to control the spacer layers and show how that impacts to control the proximity of AuNRs and alters the optical properties.

4.2 Sample preparation

4.2.1 Gold nanorods (AuNRs) solution preparation and drop casting

Commercially available colloidal gold nanorods suspended in DI water from Nanopartz Inc. were used in our experiments. The AuNRs are coated with cetyl trimethylammonium bromide (CTAB) surfactants. The nanorods solution is diluted 100 times by taking 10 µl of nanorods and adding it into 1 ml of DI water using micropipettes. Then 20 µl of the diluted AuNRs solution is drop cast onto a cleaned GaAs substrate purchased from University Wafer (undopped with orientation 100), and placed on a shaker for 1 minute. Then the solution is blown off with N_2 gun before it dries completely to avoid particle aggregation and accumulation of excess surfactant molecules. The GaAs substrate is cleaned using the standard cleaning procedure – dipping in Aceton, IPA and DI water, respectively for 5 minutes in a sonicator.

4.2.2 Spin coating poly(methyl methacrylate) (PMMA)

PMMA (0.5%) in Tolune is spin coated on a GaAs substrate. Laurell spin coater (model WS-650MZ-23NPP) is used at speed 12000 rpm for 1 minute. Thickness of the PMMA is ~5 nm confirmed by atomic force microscopy. To measure the thickness, one sample is scratched by sharp bamboo stick, and another sample is immersed partly into acetone to remove PMMA from that certain part of the sample. Both the samples gave approximately the same thickness value.

4.2.3 Ultraviolet/ozone (UVO) treatment

UVO treatment on GaAs is performed using Novascan PSD Pro Series- Digital Ozone system. The sample is illuminated from the top by Mercury lamp ~2 mm away from the surface. The sample is UVO treated for 1 minute at 30 ^{0}C.

4.2.4 Silanization of GaAs substrate

To form a spacer layer on the GaAs substrate, the surface is functionalized with (3-mercaptopropyl)trimethoxysilane (MPTMS). In order to do that GaAs surface is activated applying UVO cleaning for 1 minute at 60 ^{0}C followed by vapor deposition of MPTMS for 24 hours. The MPTMS can covalently bind gold nanostructure with GaAs. Since, the MPTMS reacts with the GaAs surface, making the thiol group (-SH) available for S-Au bonding when AuNRs solution is drop casted on the top[2, 3] creating a spacer of thickness ~0.8 nm.

4.2.5 Atomic layer deposition (ALD)

Al_2O_3 film is deposited on the GaAs substrate using ALD system of Picosun. Trimethylaluminium (TMA) and H_2O vapors are pulsed alternately through the reaction chamber utilizing N_2 as carrier gas at a flow rate of 150 sccm and 200 sccm for TMA and H_2O, respectively. The pressure inside the reaction chamber is 4 Torr with the growth temperature of 150 ^{0}C. TMA reactant exposure time (pulse time) is 1 s and N_2 purge following TMA exposure time is 10 s. H_2O reactant exposure time is 1.5 s and N_2 purge following H_2O exposure time is 20 s for Al_2O_3 growth on GaAs. Long purge times are necessary at low temperature to prevent chemical vapor deposition of Al_2O_3.[13] This growth temperature and pulse/purge time for TMA and H_2O have been optimized carefully to

obtain uniform and conformal deposition of Al_2O_3 on GaAs substrate. TMA and H_2O yield ALD Al_2O_3 growth according to the following two self- limiting surface reactions,[13,14]

$$AlOH^* + Al(CH_3)_3 \rightarrow AlOAl(CH_3)_2^* + CH_4 \quad \ldots\ldots\ldots\ldots\ldots\ldots A$$

$$AlCH_3^* + H_2O \rightarrow AlOH^* + CH_4 \quad \ldots\ldots\ldots\ldots\ldots\ldots B$$

where the * denotes the surface species. The overall reaction for ALD Al_2O_3 is,

$$2Al(CH_3)_3 + 3H_2O \rightarrow Al_2O_3 + 3CH_4$$

4.3 Al_2O_3 film thickness measurement by variable angle spectroscopic ellipsometry (VASE)

Al_2O_3 spacer layer thicknesses are measured by J. A. Woolam Co., Inc. V- VASE using WVASE32 software. Spectroscopic scans of 600-800 nm by 10 nm interval for each spacer layer are performed at 60^0 -70^0 with 10^0 interval relative to the normal of the surface of the sample. Ellipsometry data are analyzed using a layer model where Al_2O_3 spacer layer thickness is fitted using Cody-Lorentz oscillator provided by VASE software. Cody-Lorentz oscillator modeling of the VASE data yields a refractive index for ALD Al_2O_3 of n_{min} = 1.6603 and n_{max} = 1.6675 for the wavelength range 600 - 800 nm. In the layer model, 0.8 nm thick oxide layer is added on top of the GaAs substrate.

4.4 Dark-field microscopy

The AuNRs are excited by white light using dark-field microscope objective of numerical aperture 0.9. The dark-field scattering measurement is carried out using the GX51F5 Olympus microscope. The schematic is shown in Figure 5.6 in Chapter 5. The sample mounted on top of the objective was excited with 100W halogen lamp white light

source. Dark-field images of the individual AuNRs are obtained by directing 10% of the signal to the camera (Olympus UC30) attached to the microscope. The corresponding scattering spectra are recorded by centering the particle to the focus of the objective, and directing 90% of the light collected from the sample to the spectrometer (IsoPlane Spectrograph of Princeton Instruments), which uses a thermoelectrically cooled (-75^0C) and back-illuminated deep depletion CCD camera.

4.5 Electromagnetic simulation

Electromagnetic simulation is carried out to reproduce the experimental results obtained for dark-field scattering and to have an idea about the field localization in the near-field proximity. The electromagnetic simulation is carried out using finite-difference time domain (FDTD) method, which is implemented using a commercial software package (Lumerical Solutions, Inc.). A total-field scattered field source scheme is used to introduce light energy into the simulation region, where the grid size is 0.5 nm for all x-, y- and z-axes.

4.6 Results and discussion

4.6.1 Controlling the gap by organic spacer layer using spin coating

In order to increase the efficiency of the plasmonic coupling to the III-V semiconductor emitter, we try to control the gap between AuNRs and GaAs using organic spacer layer. To this extent, about 5 nm thick PMMA (0.5 % in Toluene) is spin coated on the GaAs and the AuNRs with the aspect ratio of 2 (80 nm × 40 nm) are drop cast above the PMMA coated GaAs. In the dark-field microscope image, we observe the number of red color doughnut shape AuNRs increases significantly as shown in Figure 4.1b

comparing with AuNRs applied directly on the GaAs surface shown in Figure 4.1a. The green and yellow color AuNRs are also present in the dark-field image, but they are not the majority as before without PMMA. The representative dark-field scattering spectra of the corresponding color AuNRs are presented in Figure 4.1c. However, we have figured out that this system is not stable. When the same sample is observed again under dark-field microscope after 12 hours, the majority of the particles turn into green. This is attributed to interaction between CTAB coated AuNRs and organic PMMA. PMMA (formula $(C_5O_2H_8)n$) is an organic polymer that interacts with the CTAB (formula $C_{19}H_{42}BrN$) which is a long chain carbon molecule. Therefore, the CTAB penetrates through the PMMA and the spacer between GaAs and AuNRs collapses.

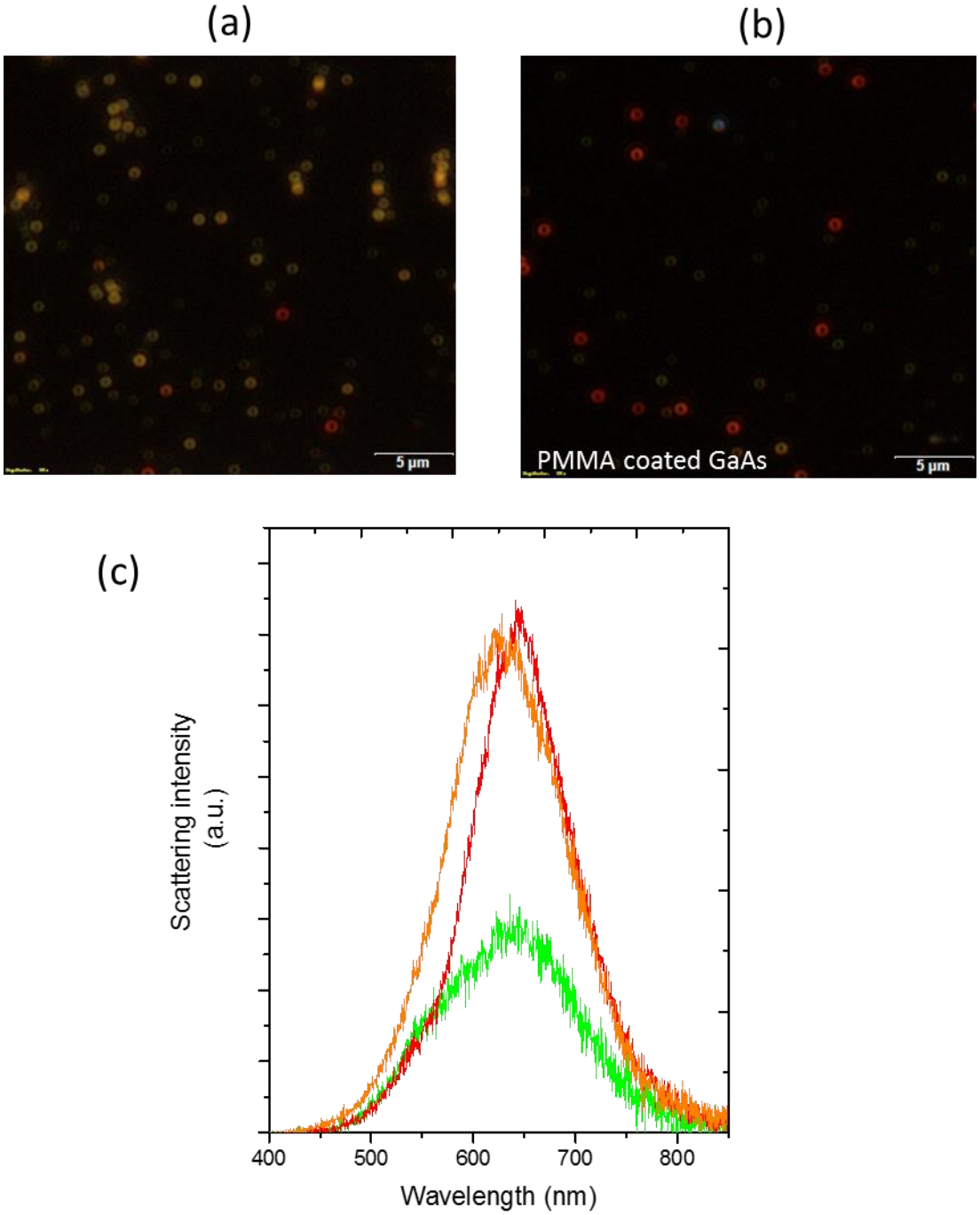

Figure 4.1 (a), (b) Dark-field images of AuNRs (80 nm × 40 nm) capped by CTAB surfactants (a) on GaAs substrate (b) on ~5 nm thick PMMA coated GaAs. Comparing (a) and (b), it is apparent that number of red color AuNRs increases. (c) Representative scattering spectra of green, yellow, and red color AuNRs on PMMA (~5 nm) coated GaAs.

4.6.2 Spacer layer control by UVO treatment and silanization of GaAs

To control the spacer layer thickness between GaAs and AuNRs, the surface is treated with ultraviolet/ozone (UVO). We observe, the number of doughnut shape red color AuNRs increases nominally (around 5 %) as shown in Figure 4.2a, and the representative dark-field scattering spectra from the red color AuNRs is plotted in Figure 4.2b.

Therefore, the GaAs surface is silanized using MPTMS to create gap (~0.8 nm) between AuNRs and GaAs. The number of doughnut shape red color AuNRs increases around 56 % shown in the dark-field image in Figure 4.3 a, and b comparing with AuNRs directly dispersed on the GaAs substrate. The representative scattering spectra for red color AuNRs is presented in Figure 4.3c.

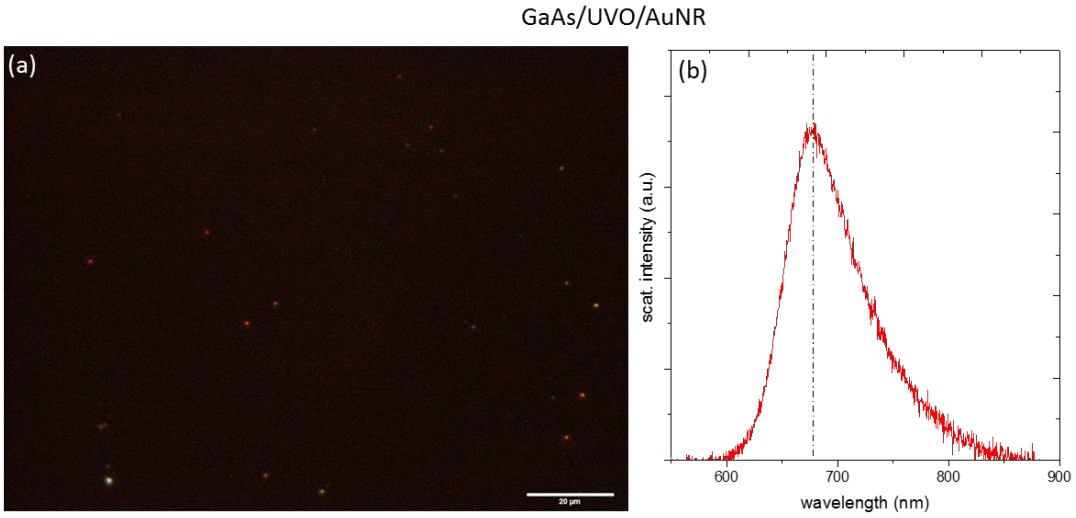

Figure 4.2 (a) Dark-field image of AuNRs (80 nm × 40 nm) on UVO treated GaAs showing nominal increment of number of red particles. Green particles are not prominent here due to color contrast. The scale bar at the bottom showing 20 µm. (b) Representative dark-field scattering spectra obtained from red color AuNRs. The vertical dashed line indicates average emission wavelength for 21 measured particles at 674 ± 13 nm.

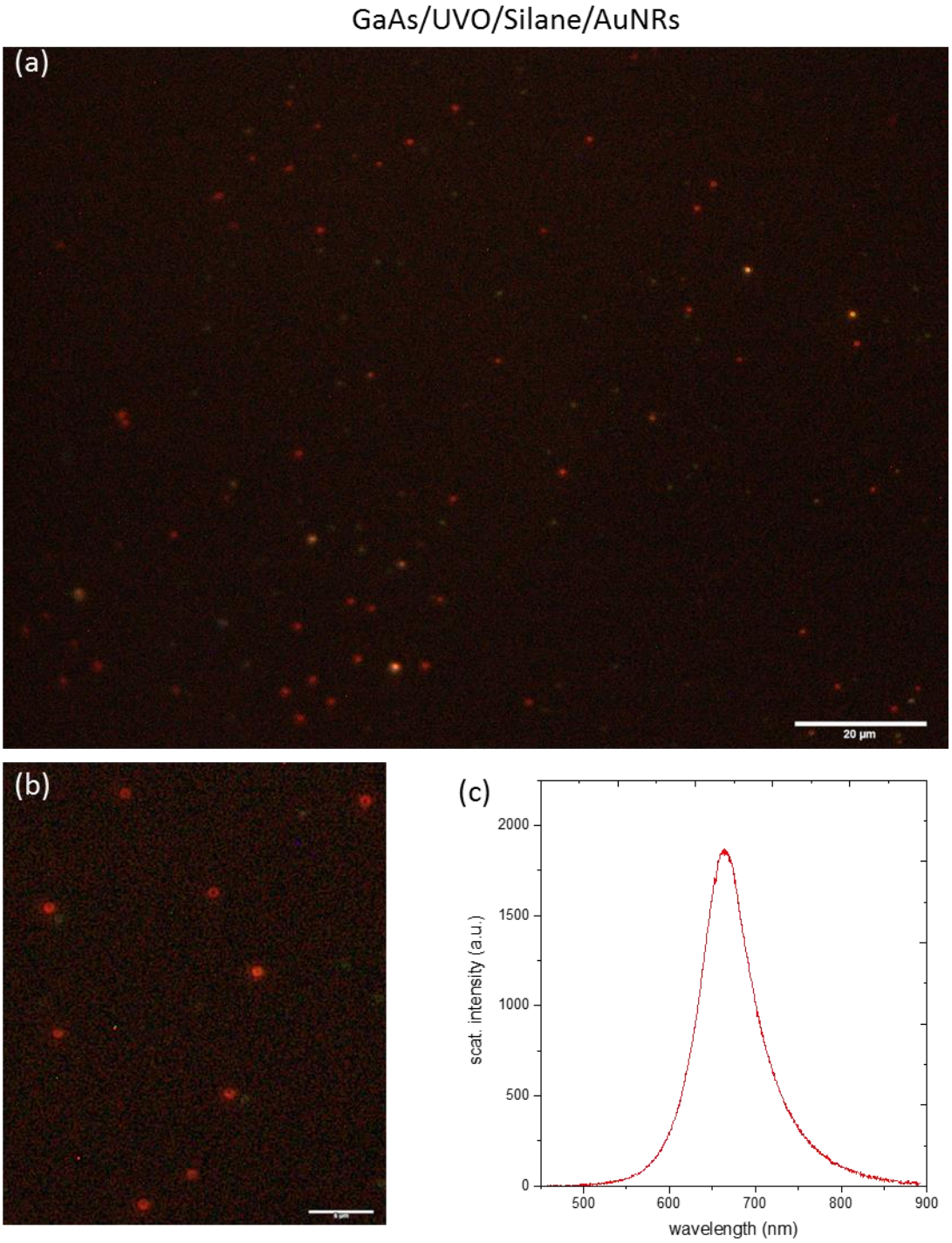

Figure 4.3 (a) Dark-field image of AuNRs (80 nm × 40 nm) on UVO treated GaAs followed by silanization showing increment of number of red particles. The scale bar at the bottom showing 20 µm. (b) Dark-field image of the same sample used for (a) with higher magnification. The scale bar at the bottom showing 5 µm. (c) Representative dark-field scattering spectra obtained from red color AuNRs. The average emission wavelength for 22 measured particles is at 666 ± 16 nm.

The effect of UVO treatment and silanization of the GaAs substrate in changing the color of the AuNRs in the dark-field image due to creating gap, is presented in Table 4.1. The corresponding color radiation pattern of the AuNRs are shown on the top panel in Table 4.1. The increment (in percent) of red color AuNRs is also compared in Figure 4.4 (a) for 3 different samples, where AuNRs are i) directly applied on GaAs ii) on UVO treated GaAs, and iii) on silane treated GaAs. The scattering spectra from the red particles after surface treatment of GaAs with UVO and silanization does not change as shown in Figure 4.4b.

Table 4.1 AuNRs on UVO and silane treated GaAs

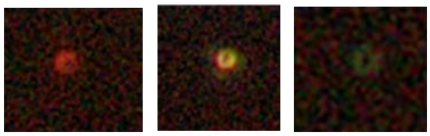

#	Sample	Measured area (µm)	Red	Yellow	Green
1	GaAs/AuNR	148*100	1%	7%	92%
2	GaAs/UVO/AuNR	148*100	5%	4%	91%
3	GaAs/UVO/Silane/ AuNR	148*100	56%	7%	37%

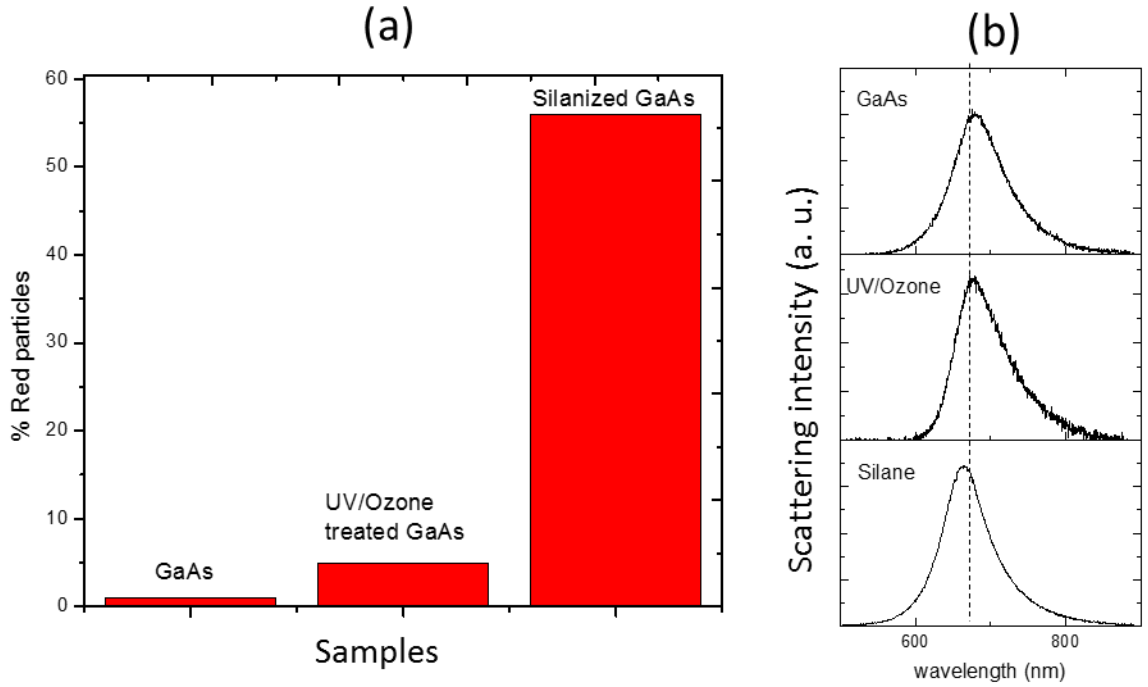

Figure 4.4 (a) Increment in red color AuNRs (in percent) after surface treatment of GaAs by UVO treatment and silanization comparing with AuNRs directly applied on GaAs substrate. (b) Representative scattering spectra of red color AuNRs (80 nm × 40 nm) from 3 different samples as labeled in the Figure. The vertical dashed line indicating average resonance for red color AuNRs directly applied on GaAs.

It is important to note that, if the GaAs substrate is cleaned with hydrofluoric acid (HF) to remove native oxides from the surface and then treated with silane, it does not help to increase the number of red Au particles. The dark-field image of AuNRs on silane treated GaAs with prior HF cleaning and without HF cleaning is shown in Figure 4.5a, b. It is obvious from the dark-field image that removing native oxide using HF makes the GaAs surface rough, and is not useful for creating gap between GaAs and AuNRs. Presence of native oxide supports to control the distance (i.e. increase number of red particles) between AuNRs and GaAs.

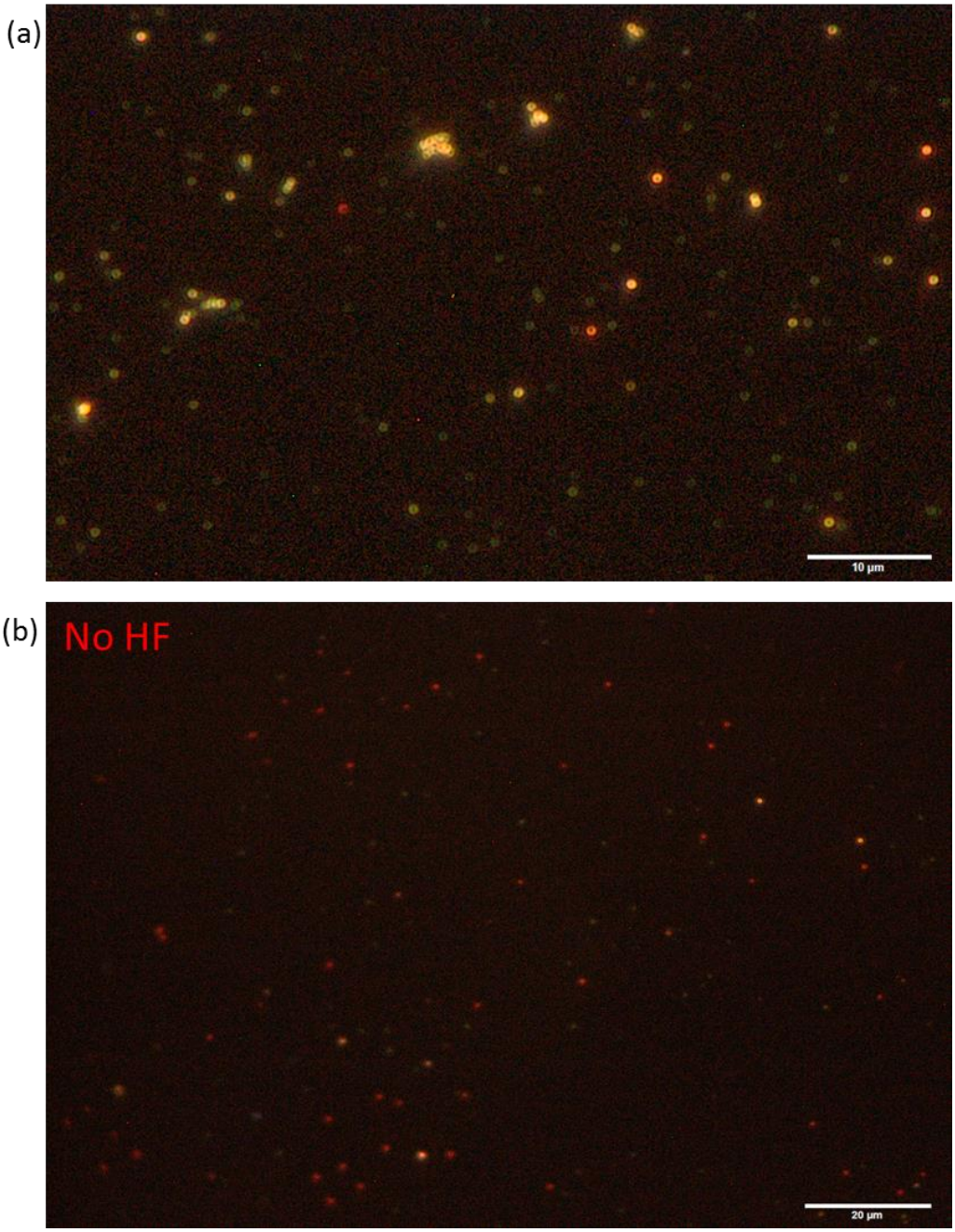

Figure 4.5 Dark-field images of AuNRs (80 nm × 40 nm) on silane treated GaAs (a) prior surface cleaning with HF (b) no HF cleaning before silanization.

As discussed above, the silanization of GaAs surface using MPTMS can improve the emission efficiency by increasing the number of red particles because of creating spacing between AuNRs and GaAs. But the green color AuNRs are also present (~37 %)

in the dark-field image. Besides, the spacing created between the AuNRs and the GaAs surface is not uniform. Furthermore, controlling of spacer layer thickness is another issue with the silane treated surface. Therefore, we need to implement alternative approach to control the spacing between plasmonic AuNRs and the semiconductor which can provide uniform, conformal deposition of spacer layer with sub-nanometer accuracy.

4.6.3 Influence of dielectric layer on Si

A dielectric SiO_2 layer of thickness ~1-2 nm forms naturally on Si substrate at room temperature. To understand the influence of SiO_2 dielectric layer on Si substrate, we remove the oxide layer by cleaning the Si substrate with HF. To be mentioned, Si has high index which is close to GaAs. Therefore, the influence of SiO_2 dielectric layer on Si can provide some insight for AuNR-GaAs system separated by Al_2O_3 dielectric layer. To that extent, we measure the dark-field scattering of AuNRs (92 nm × 40 nm) deposited directly on Si, and on HF cleaned Si as shown in Figure 4.6c and d, respectively. The dark-field images of AuNRs of the corresponding samples are shown in Figure 4.6a and b, respectively. We observe more green particles in the dark-field image, when the substrate is cleaned with HF. This indicates etching SiO_2 layer from Si substrate which makes Si surface closer to AuNRs. In the scattering spectra (Figure 4.6c), red shifting is observed when the SiO_2 layer is etched, which is due to high refractive index of Si.

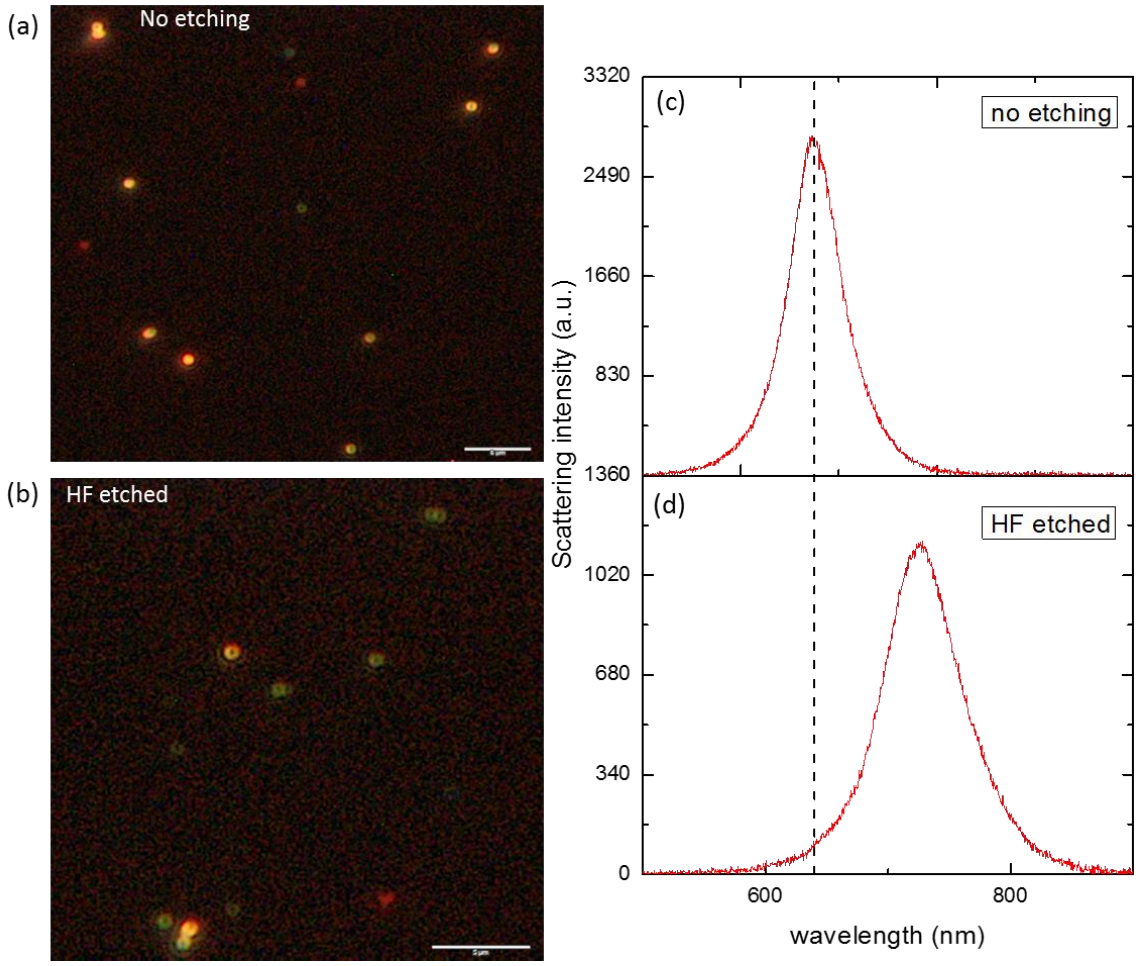

Figure 4.6 (a)-(b) Dark-field images of AuNRs (92 nm × 40 nm) on (a) Si substrate (b) HF etched Si substrate. The scale bar at the bottom is 5 µm. (c) - (d) The representative scattering spectra obtained from individual red color AuNRs on (c) Si substrate (d) HF etched Si substrate. The vertical dashed line indicates the resonance of AuNRs (92 nm × 40 nm) for ~1 nm - 2 nm thick oxide coted Si.

4.6.4 Spacer layer control by atomic layer deposition (ALD) of Al_2O_3

The spacer layer between the AuNRs and the GaAs can be controlled more precisely with sub-nanometer accuracy using ALD for the deposition of Al_2O_3 dielectric spacer. Moreover, ALD provides uniform and conformal deposition of Al_2O_3. Topography image obtained by atomic force microscopy (Veeco Quadrex D3100) in Figure 4.7 shows the uniform, conformal deposition of 3.54 ± 0.03 nm Al_2O_3 film on the GaAs substrate.

The surface roughness (rms) of the Al_2O_3 film grown on the GaAs substrate is 0.23 nm. We do not observe any island formation in the atomic force microscopy (AFM) image due to chemical vapor deposition (CVD) which may occur for the deposition of very thin layer of Al_2O_3.

The dark-field images of the AuNRs on ~3.5 nm thick Al_2O_3 coated GaAs and AuNRs directly applied on GaAs substrate are compared in Figure 4.8a and b, respectively. We observe, the number of red color AuNRs increases significantly for ~3.5 nm thick Al_2O_3 film deposited on GaAs. To be noted, the radiation pattern for all the AuNRs are doughnut shaped.

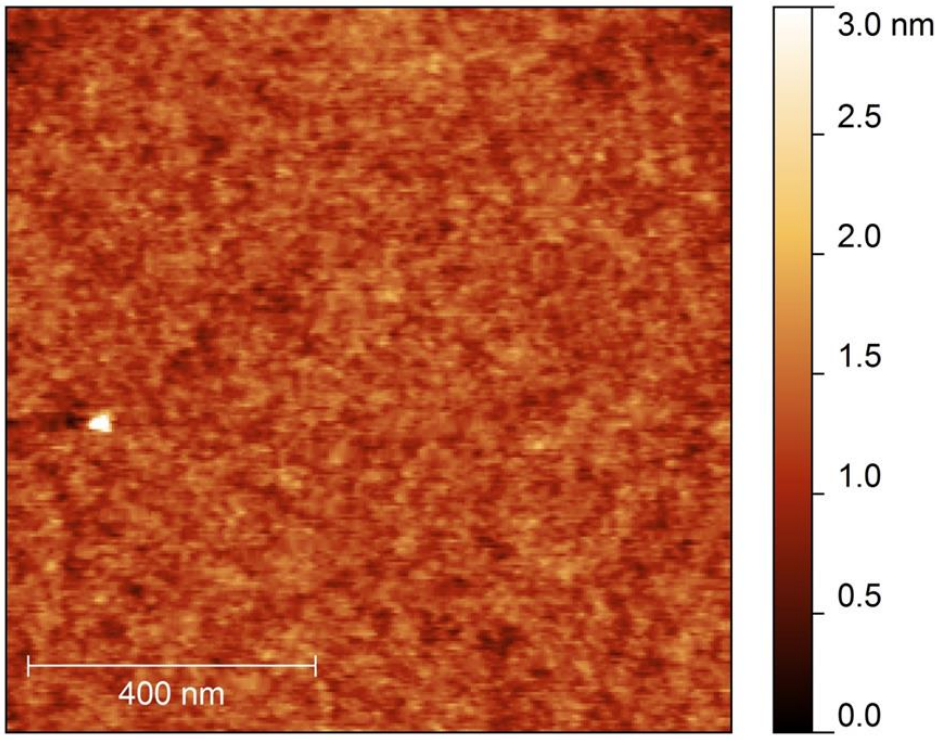

Figure 4.7 AFM topography image of ~3.5 nm thick Al_2O_3 grown on GaAs substrate by ALD at 150 ^{0}C. The surface roughness (rms) of this Al_2O_3 film is 0.23 nm.

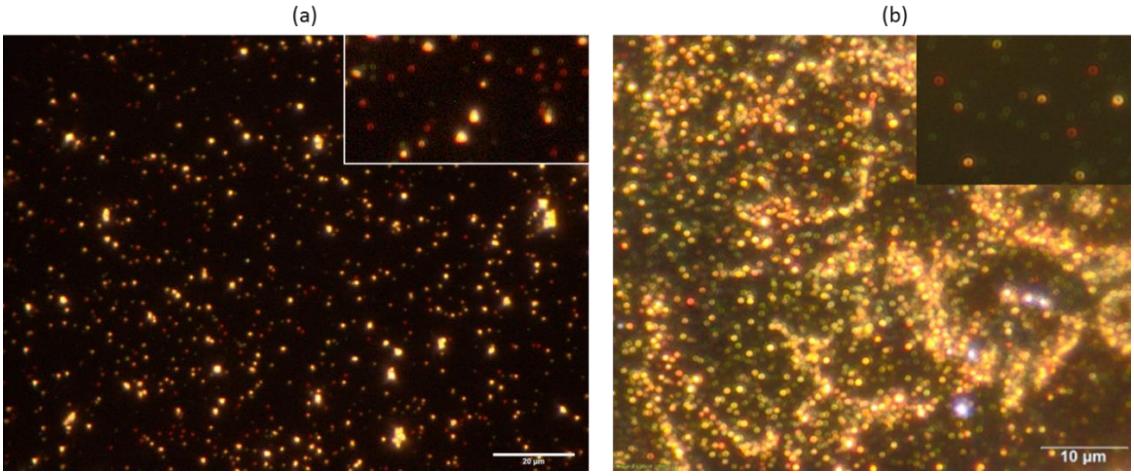

Figure 4.8 Dark-field images of AuNRs (a) on ~3.5 nm thick Al_2O_3 coated GaAs (b) on GaAs substrate. Inset showing zoomed view of the dark-field image.

To explore the distance dependence of the optical interaction for the AuNRs on GaAs semiconductor, the Al_2O_3 film thickness is varied from 3.5 nm up to 25 nm. The dark-field images of AuNRs on the GaAs separated by different Al_2O_3 film thicknesses are shown in Figure 4.9 and their corresponding thicknesses are labeled on the top. We observe, the radiation pattern of the AuNRs are still doughnut shape for 8.5 nm thick Al_2O_3 spacer layer, and turn into solid spot for the spacer layers thickness of 21 nm and 25 nm. This indicates, the GaAs has strong capacitive coupling with plasmonic AuNRs through Al_2O_3 spacer even up to 8.5 nm. This strong coupling in AuNR-GaAs system for such a thicker spacer is attributed to high index value of the GaAs.

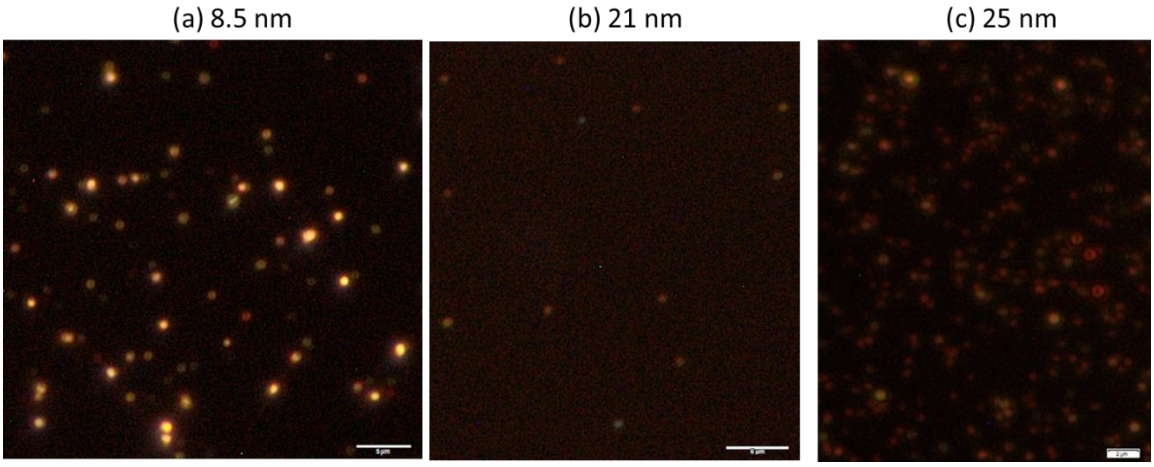

Figure 4.9 Dark-field images of AuNRs on ALD Al_2O_3 coated GaAs for different thicknesses of Al_2O_3 spacer layer (a) 8.5 nm (bottom scale bar 5 μm) (b) 21 nm (bottom scale bar 5 μm) (c) 25 nm (bottom scale bar 2 μm).

To investigate the coupling for the AuNR-GaAs system more detail, the scattering intensity map of AuNRs for different Al_2O_3 spacer layer thicknesses are plotted in Figure 4.10a. The normalized scattering spectra measured for individual AuNRs coupled to GaAs semiconductor through Al_2O_3 dielectric spacer layers of different thicknesses are shown in Figure 4.10b. The normalized spectra for individual nanorod is chosen that represents the average characteristics for that particular sample. To be noted, we need to prepare more samples by varying the spacer layer thickness to have a comprehensive idea about the coupling property for this system. Until then, we can have a rough estimate about the AuNR-GaAs system, so that we can fine tune our spacer layers thickness in future.

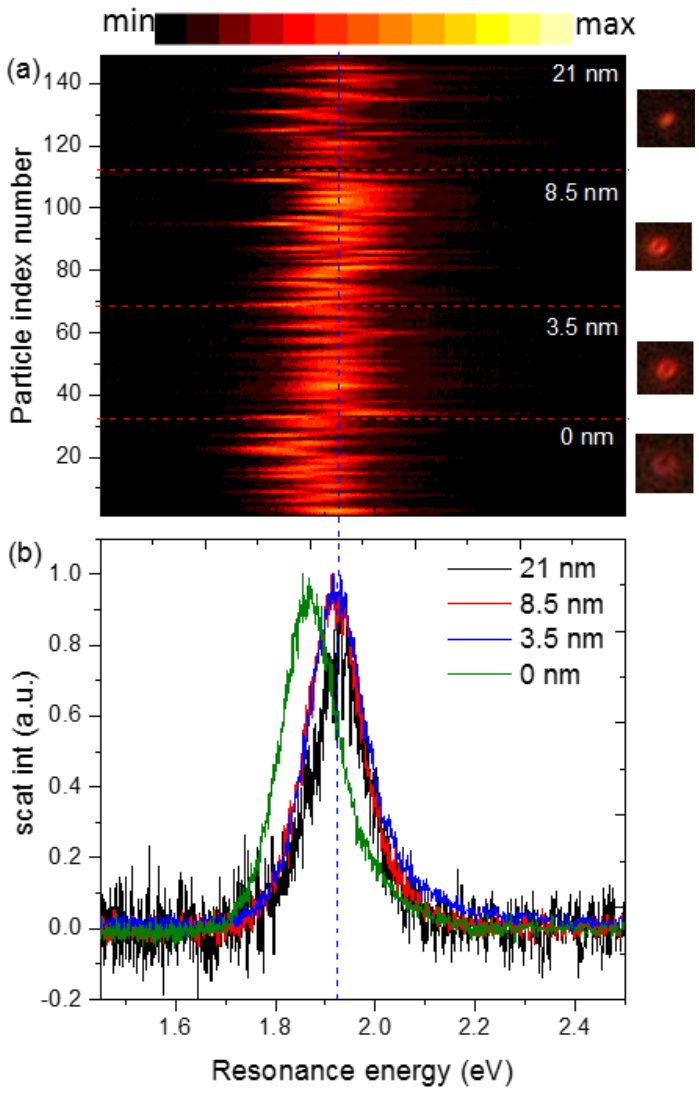

Figure 4.10 (a) Intensity map of scattering spectra of AuNRs (80 nm × 40 nm) for AuNR-GaAs system with different Al_2O_3 dielectric spacer layer thicknesses as labeled in the plot. The corresponding radiation pattern of individual AuNR for each thickness is shown on the right panel. (b) Representative normalized scattering spectra. The vertical blue dashed line indicates the average gap resonance energy observed for the Al_2O_3 spacer layer thicknesses 3.5 nm to 21 nm. All these scattering spectra are obtained on the same day to maintain the same experimental condition.

For each spacer layer thickness, single particle scattering spectra of around 40 different AuNRs of red color are acquired so that we can obtain a good estimate of average characteristics of the plasmon scattering. We observe, strong scattering intensity for the Al_2O_3 spacer layer thickness of 3.5 nm, 8.5 nm and without any spacer layer (0 nm) in the

intensity map (Figure 4.10a). The scattering intensity is relatively weaker for Al_2O_3 dielectric spacer layer thickness of 21 nm. Hence, the radiation pattern also evolves from doughnut to solid shape for this thickness. This indicates, the AuNRs couples strongly with the GaAs through Al_2O_3 dielectric spacer even up to 8.5 nm. We also notice, the coupled resonance energy does not change significantly after coating Al_2O_3 on the GaAs substrate due to high refractive index (3.86 at wavelength 633 nm). As indicated by the blue dashed line in Figure 4.10, average resonance energy (~1.92 eV) for the AuNR-GaAs system separated by the Al_2O_3 spacer layer thickness of 3.5 nm, 8.5 nm and 21 nm, are comparable.

To have more insight into AuNR-GaAs system with different thicknesses of Al_2O_3 spacer layer, we investigate the resonance energy and the FWHM/linewidth for individual red color AuNRs for each sample, which is shown in Figure 4.11 a, and b, respectively. The resonance energy and the FWHM values are extracted from the single particle spectra by fitting the Lorentzian function to the experimental data. The gap plasmon resonance energy does not shift significantly for the Al_2O_3 spacer layer thickness of 3.5 nm to 21 nm as observed in Figure 4.11a. Slight red-shift is detected with decreasing the spacer layer thickness, for example ~15 meV red-shift is observed when the spacer layer thickness reduces from 8.5 nm to 3.5 nm.

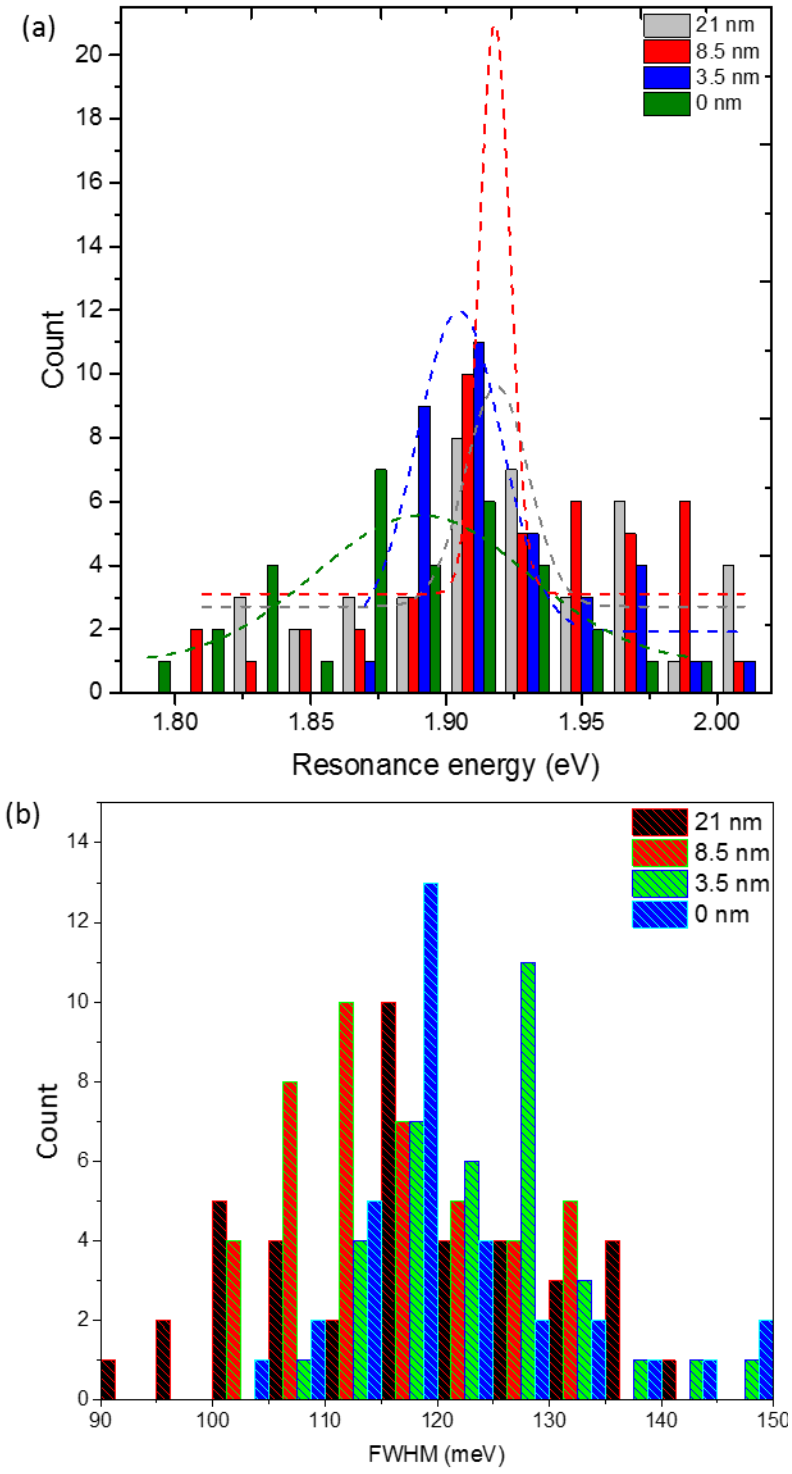

Figure 4.11 (a) Resonance energy, and (b) FWHM of AuNRs (80 nm × 40 nm) for AuNR-GaAs system with different Al_2O_3 thicknesses. These values are extracted from the single particle spectra by fitting Lorentzian function to the experimental data. The grey, red, blue, and green dashed line in (a) indicate the Gaussian fit to resonance energy obtained from single AuNR for Al_2O_3 thickness 21 nm, 8.5 nm, 3.5 nm, and 0 nm, respectively.

We observe, the FWHM decreases for the Al_2O_3 thickness of 21 nm, comparing with thinner Al_2O_3 spacer and no Al_2O_3 spacer shown in Figure 4.11b. This indicates, for a 21 nm thick dielectric spacer, the coupling for the AuNR-GaAs system is weak, hence the AuNRs feel the Al_2O_3 spacer layers rather than the GaAs substrate. Therefore, the linewidth narrowing for 21 nm spacer is contributed from the low loss Al_2O_3 dielectric rather than coupling with lossy GaAs substrate. To be noted, extinction co-efficient for Al_2O_3 is $3.5 \times e^{-6}$ (at $\lambda = 600$ nm), and for GaAs is 0.23 (at $\lambda = 600$ nm). Here, extinction = absorption + scattering. The broadening of FWHM is observed when the spacer layer thickness reduces from 8.5 nm to 3.5 nm or even for no spacer layer (Figure 4.11b), which indicates strong interaction between plasmonic AuNRs and the GaAs substrate with decreasing gap. This interaction increases non-radiative losses which are associated with the material losses of the system, and dependent on the dielectric function, as the resonance energy does not shift significantly as well as the scattering intensity does not drop.

As we know, capacitive coupling strength decreases with increasing distance, therefore the AuNR-GaAs system with an Al_2O_3 spacer layer thickness of 21 nm is not effective, since the substrate effect is minimal for this thicker spacer layers. The linewidth narrowing along with weaker scattering intensity, and evolution of radiation pattern to solid shape for the Al_2O_3 spacer layer thickness of 21 nm support this observation.

We have another observation to support the coupling strength as discussed above for the AuNR-GaAs system. We measure the scattering from Al_2O_3 coated GaAs, and GaAs substrate without any plasmonic structure as shown in Figure 4.12. We notice, strong scattering from the GaAs substrate (Figure 4.12a), and a sharp scattering peak is observed just below the GaAs band gap energy (1.42 eV). This strong scattering also exists for

Al_2O_3 coated GaAs of Al_2O_3 thicknesses 3.5 nm and 8.5 nm (Figure 4.12b, and c, respectively), but does not occur for 21 nm (Figure 4.12d). This indicates, the influence of the GaAs substrate for 21 nm thick dielectric spacer layer on top, is extremely weak when the plasmonic AuNRs are coupled.

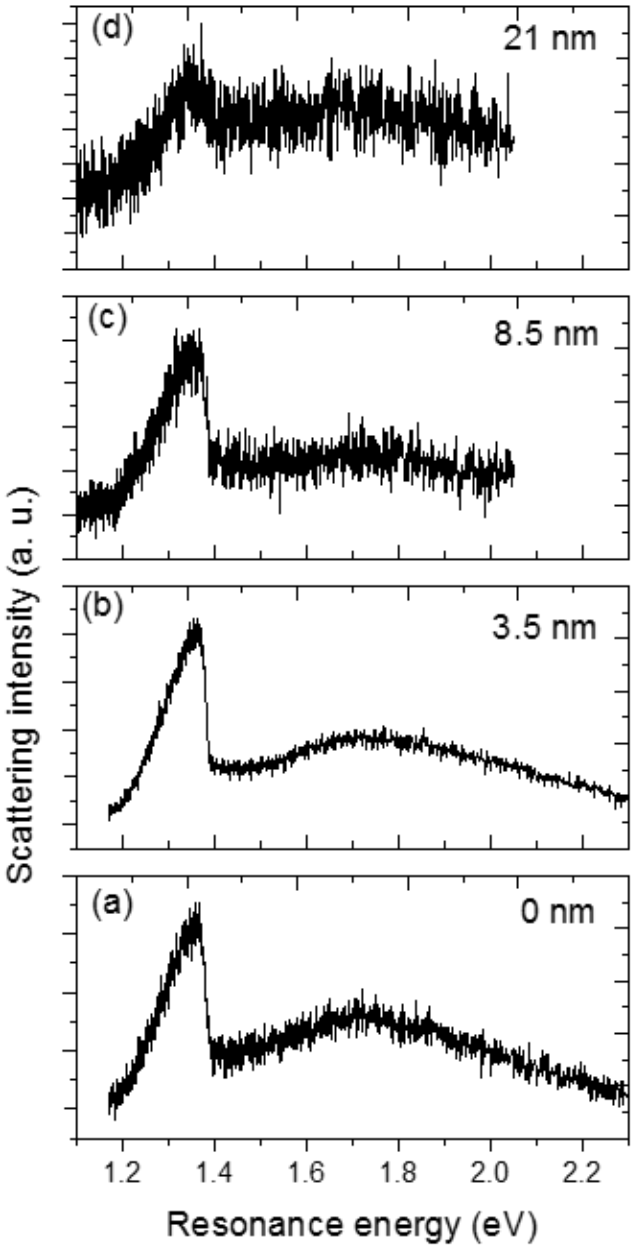

Figure 4.12 Scattering spectra without plasmonic AuNRs from (a) GaAs (no spacer layer = 0nm) (b) Al_2O_3 spacer layer = 3.5 nm (c) Al_2O_3 spacer layer = 8.5 nm, and (d) Al_2O_3 spacer layer = 21 nm.

It is important to note, we observe greenish color particles in the dark-field image shown in Figure 4.13a after deposition of ALD Al_2O_3 on the GaAs substrate. We distinguish these particles from the AuNRs by measuring the scattering as shown in Figure 4.13b, c. We observe similar scattering property for the Al_2O_3 thickness 8.5 nm (Figure 4.13 b) and 21 nm (Figure 4.13 c) because these particles are inherent in ALD Al_2O_3 and does not depend on distance.

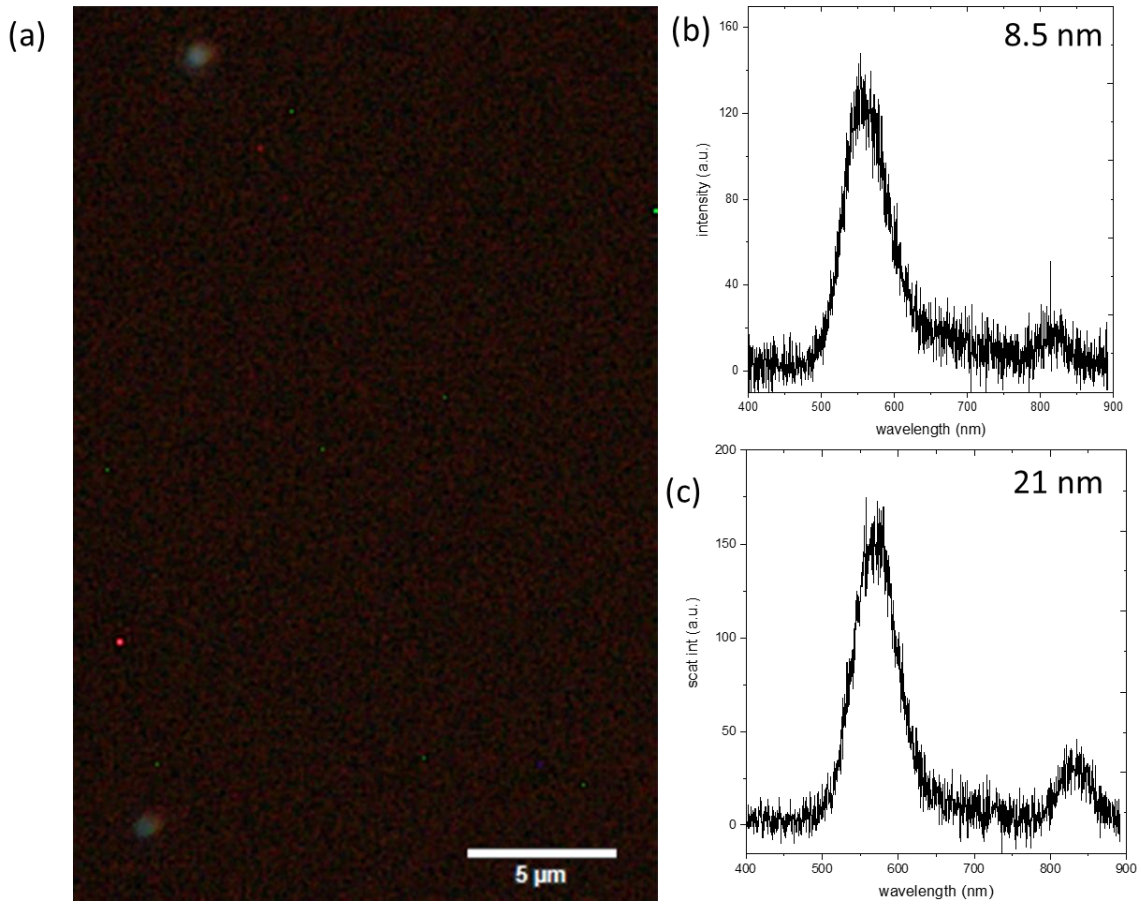

Figure 4.13 (a) Dark-field image of Al2O3 coated GaAs. Greenish particles are found after Al_2O_3 deposition. (b), (c) Scattering spectra from single greenish particles shown in (a) for Al_2O_3 thickness 8.5 nm and 21 nm, respectively.

In addition, the results of electromagnetic simulation (see Figure 4.14) represent the near-field amplitude and localization for AuNR-GaAs system of different spacer layer thicknesses at 633 nm. The tight near-field localization at the AuNR-GaAs interface gradually vanishes with increasing Al_2O_3 thickness and for 20 nm thickness (Figure 4.14a)) the field distribution is similar to AuNR-SiO2, which supports our experimental results as discussed above.

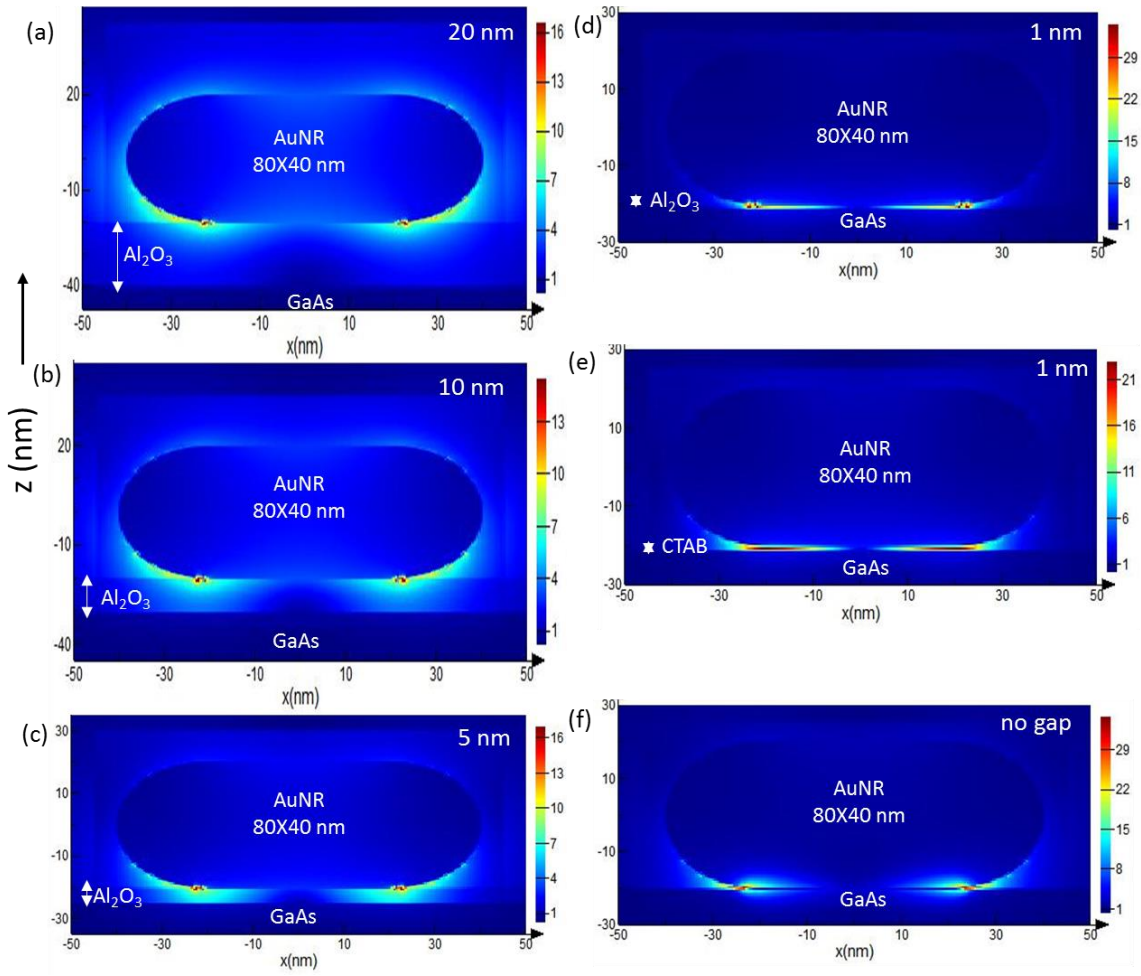

Figure 4.14 Calculated near-field amplitude and localization at wavelength 633 nm in xz plane for AuNR-GaAs system through spacer layer thickness of (a)-(d) Al_2O_3 20, 10, 5, and 1.0 nm, respectively (e) CTAB 1.0 nm, and (f) no gap.

Furthermore, the substrate's effect on plasmonic properties for 21 nm thick Al_2O_3 spacer layer deposited on GaAs, and on SiO_2 is compared in Figure 4.15. The dark-field images and calculated near-field distribution for AuNRs on Al_2O_3 coated GaAs (see Figure 4.15a, c) and on SiO_2 (see Figure 4.15b, d) indicate the substrate's effect is negligible, and the plasmonic properties are dominated by the properties of spacer layer. The FWHM and resonance energy (fitting Lorentz function to experimentally obtained scattering from ~40 different single AuNR) are compared for the AuNR-Al_2O_3-GaAs and the AuNR-Al_2O_3-SiO_2 systems, where Al_2O_3 spacer thickness is 21 nm as shown in Figure 4.15e, and f, respectively. As observed, the resonance energies for both systems merge (Figure 4.15 f). However, the linewidth broadens for the SiO_2 substrate compared to the GaAs substrate, because AuNRs suffers higher radiation loss in SiO_2.

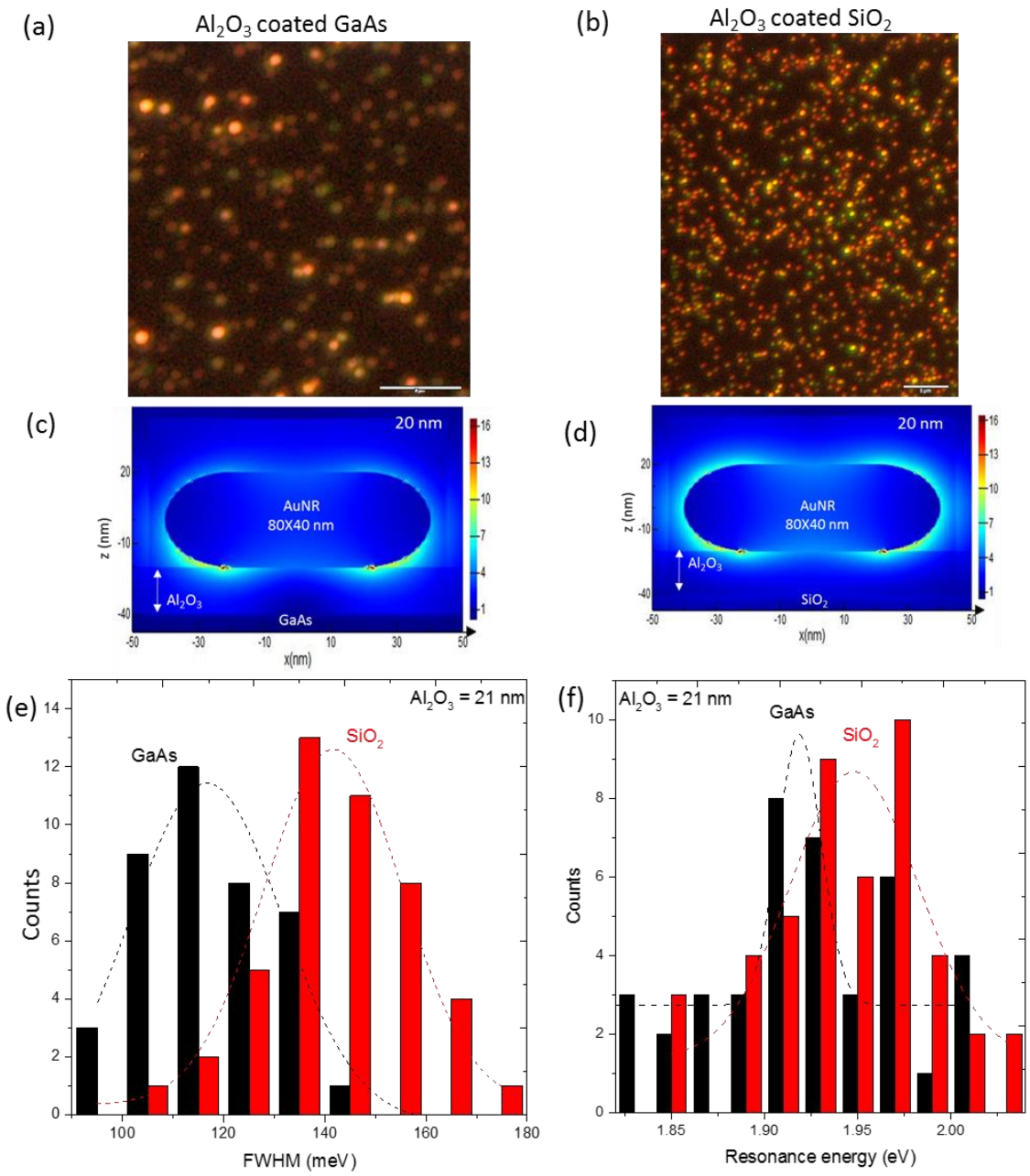

Figure 4.15 (a), (b) Dark-field images of AuNRs on 21 nm thick Al_2O_3 coated (a) GaAs (b) SiO_2. Scale bar at the bottom showing 5 µm. Calculated field distribution is compared when the AuNR is supported on 20 nm thick Al_2O_3 coated (c) GaAs (d) SiO_2 surface. (e) FWHM, and (f) resonance energy for AuNRs supported on 21 nm thick Al_2O_3 coated GaAs and SiO_2. The dashed black and red line (for GaAs and SiO_2, respectively) indicate the average value for FWHM and resonance energy obtained by Gaussian function.

Finally, 3.5 nm of ALD Al_2O_3 is deposited on InAs/InGaAs/GaAs dot-in-a-well structure with the GaAs capping layer thickness of 6 nm to study how the spacer layer

effects the optical properties of the plasmon coupled InAs/InGaAs/GaAs DWELL structure. To be noted, strongest near-field interaction is observed between the InAs QD emitters and the AuNRs for the GaAs capping layer thickness of 6 nm as discussed in detail in Chapter 2. We measure the photoluminescence at room temperature to calculate the enhancement factor (integrated PL intensity ratio with AuNRs to without AuNRs) for the InAs/InGaAs/GaAs and Al_2O_3 coated InAs/InGaAs/GaAs as shown in Figure 4.16b and d, respectively. Enhancement factor is measured 1.6 for the InAs/InGaAs/GaAs, and 3.1 for the Al_2O_3 coated InAs/InGaAs/GaAs. Hence, enhancement factor improves 2.5 times after depositing Al_2O_3 (~3.5 nm) on the dot-in-a-well semiconductor. The dark-field images of the AuNRs are compared for no Al_2O_3 spacer and with the Al_2O_3 spacer in Figure 4.16c and c, respectively. It is important to note that, overall the PL intensity drops after coating Al_2O_3 dielectric spacer on the DWELL semiconductor heterostructure in both case with and without AuNRs. Therefore, Al_2O_3 dielectric spacer is not a good choice for the InAs/InGaAs/GaAs DWELL structure.

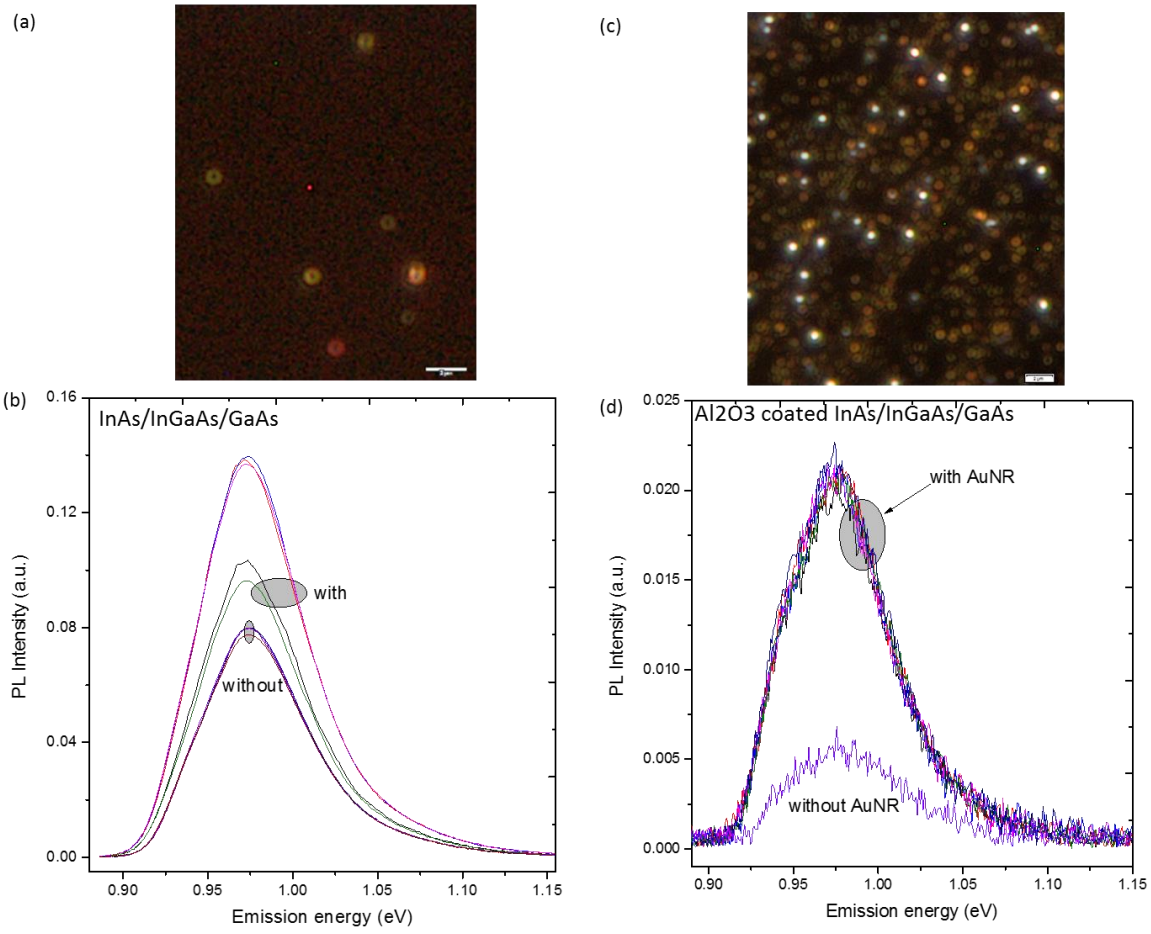

Figure 4.16 (a), (c) Dark-field images of AuNRs on InAs/InGaAs/GaAs (a) no Al_2O_3 spacer (c) with ~4 nm Al_2O_3 spacer layer. Scale bar at the bottom is 2 µm. PL of InAs/InGaAs/GaAs with and without AuNRs (b) no Al_2O_3 spacer (d) with ~4 nm Al_2O_3 spacer layer.

4.7 Conclusion

Controlling the spacer layer and understanding the optical properties after depositing spacer layer between plasmonic structure and InAs/InGaAs/GaAs dot-in-a-well structure is vital for the advancement of optoelectronic devices. Hence, organic and inorganic spacer layers are used to control the thickness. The plasmonic gold nanorods are coated with organic CTAB molecule. Therefore organic spacer layer is not useful, since it interacts with the CTAB. Inorganic dielectric spacer can be a good candidate to control the

thickness. Atomic layer deposition of Al_2O_3 dielectric can precisely control the thickness in sub-nanometer scale. We observe, the scattering property does not change significantly after Al_2O_3 spacer layer deposition because of strong interaction between gold nanorods and GaAs due to high refractive index of GaAs. It has been shown that enhancement factor improves 2.5 folds for plasmon coupled InAs/InGaAs/GaAs after depositing ~3.5 nm Al_2O_3 spacer layer. Further optimization is required to control the thickness to achieve better performance.

References

1. Haq, S. *et al.* Active Mediation of Plasmon Enhanced Localized Exciton Generation, Carrier Diffusion and Enhanced Photon Emission. *Scientific Reports* **7**, 864 (2017).

2. Chikkaraddy, R. *et al.* How Ultranarrow Gap Symmetries Control Plasmonic Nanocavity Modes: From Cubes to Spheres in the Nanoparticle-on-Mirror. *ACS Photonics* **4**, 469–475 (2017).

3. Habteyes, T. G. Direct Near-Field Observation of Orientation-Dependent Optical Response of Gold Nanorods. *J. Phys. Chem. C* **118**, 9119–9127 (2014).

4. Knight, M. W., Wu, Y., Lassiter, J. B., Nordlander, P. & Halas, N. J. Substrates Matter: Influence of an Adjacent Dielectric on an Individual Plasmonic Nanoparticle. *Nano Lett.* **9**, 2188–2192 (2009).

5. Maier, S. A. & Atwater, H. A. Plasmonics: Localization and guiding of electromagnetic energy in metal/dielectric structures. *Journal of Applied Physics* **98**, 011101 (2005).

6. Ciracì, C. *et al.* Probing the Ultimate Limits of Plasmonic Enhancement. *Science* **337**, 1072 (2012).

7. Tserkezis, C. *et al.* Hybridization of plasmonic antenna and cavity modes: Extreme optics of nanoparticle-on-mirror nanogaps. *Phys. Rev. A* **92**, 053811 (2015).

8. Hill, R. T. *et al.* Plasmon Ruler with Angstrom Length Resolution. *ACS Nano* **6**, 9237–9246 (2012).

9. Lassiter, J. B. *et al.* Plasmonic Waveguide Modes of Film-Coupled Metallic Nanocubes. *Nano Lett.* **13**, 5866–5872 (2013).

10. Kafle, B. *et al.* Robust Charge Transfer Plasmons in Metallic Particle–Film Systems. *ACS Photonics* **5**, 4022–4029 (2018).

11. Mahapatro, A. K., Scott, A., Manning, A. & Janes, D. B. Gold surface with sub-nm roughness realized by evaporation on a molecular adhesion monolayer. *Appl. Phys. Lett.* **88**, 151917 (2006).

12. Habteyes, T. G. *et al.* Metallic Adhesion Layer Induced Plasmon Damping and Molecular Linker as a Nondamping Alternative. *ACS Nano* **6**, 5702–5709 (2012).

13. Dillon, A. C., Ott, A. W., Way, J. D. & George, S. M. Surface chemistry of Al2O3 deposition using Al(CH3)3 and H2O in a binary reaction sequence. *Surface Science* **322**, 230–242 (1995).

14. Groner, M. D., Fabreguette, F. H., Elam, J. W. & George, S. M. Low-Temperature Al2O3 Atomic Layer Deposition. *Chem. Mater.* **16**, 639–645 (2004).

Chapter 5

Transition from ultra-narrow gap resonances to tunneling effects via atomic scale variation of dielectric spacer

Abstract

Plasmon resonances associated with the coupling between metal films and particle plasmons have been suggested for use in applications such as sensing, novel nanoantennas, spectroscopy, solar energy harvesting, molecular rulers and non-linear optical devices. Understanding the particle-film optical interaction and how this interaction modifies the resonance properties of the coupled system is of fundamental interest. In this work, we examine the optical response of surface ligand coated colloidal gold nanorods positioned above a gold film, separated by an inorganic dielectric spacer layer precisely controlled at angstrom length scales using atomic layer deposition. Controlling the separation in this film-coupled nanoparticle geometry accurately allow us to experimentally explore the transition in the particle-film optical interaction from the classical to quantum mechanical regime. The fundamental understanding gained from this study is important for conceiving and engineering future nanoplasmonic and nanophotonic devices.

5.1 Introduction

Light impinging on metallic nanoparticles can excite resonant oscillations of the conduction free electrons, known as localized surface plasmon resonances.[1] These resonances couple the excitation light so strongly, resulting in significant enhancement of electric field around the nanoparticles. The unique properties of these localized surface plasmon resonances are attractive for a wide array of applications, such as high sensitivity

chemical and biological sensors,[2] enhancing molecular spectroscopy,[3,4] improving photovoltaic devices,[5] and nonlinear optical devices.[6] The properties of these plasmon resonances depend on the shape, size, material properties of the metallic nanostructure, as well as the material composition of the the nanostructure, and the dielectric environment surrounding the nanostructure.[7–9] Usually uncoupled nanoparticles cannot achieve sufficiently strong field enhancement for various applications. Large near-field enhancement and broadly tunable resonances become possible when two or more nanostructures are coupled due to dipole-dipole and higher order optical interactions. Similarly strong field enhancement with tunable resonances can be achieved by coupling plasmonic nanoparticles to a polarizable metallic film due to dipole-image dipole optical interaction. Particularly, extraordinary field enhancement has been observed when a spacer layer with nanometer scale is used between the nanoparticles and the film.[10–13] Hence, metallic film coupled nanostructures geometry has become the subject of extensive research in recent years as many emerging nanophotonic technologies depend on the precise control of the plasmonic coupling. Radical changes occur for the subnanometer particle-film gaps, where quantum tunneling becomes possible.[14–17] These properties could be exploited for the improvement of nonlinear optoelectronic devices,[18,19] tunable quantum optical antennas[20] and sensors.[21] However, creating sub-nanometer gap for accessing plasmonic modes in the quantum tunneling regime (<0.5 nm) is extremely challenging. Quantum tunneling effect has been studied by state-of-the-art lithography[22] , self-assembly[13, 23] and other high tech methods for example scanning tunneling microscopes, [16] tip-to-tip orientation of atomic force microscope.[17] But more detail investigation with atomic length scale control of the sub-nanometer gap remains unexplored.

A plasmonic system consists of two metallic nanoparticles separated by a small gap is known as a plasmonic "dimer". This plasmonic dimer supports hybridized plasmon resonances as a result of the capacitive coupling between the plasmon modes of each nanoparticle.[24,25] For the bonding dipolar dimer plasmon, this coupling strongly localizes charges at the junction between the two nanoparticles, giving rise to large field enhancements and enable a wide range of applications. If the junction between the two nanoparticles is conductive, allowing direct charge transfer from one nanoparticle to the other across the inter-particle gap, then the plasmons would change profoundly enabling a distinct type of plasmon resonances, named as charge transfer plasmon (CTP).[26, 27] A key distinctive feature of the CTP is the oscillating charges between the two nanostructures through the junction.[28, 29] A CTP is a characteristic signature of electron transport at optical frequencies, by quantum tunneling or a classical conductive path, depending on the type of nanostructure.[30,31] The appearance of the CTP causes a drastic modification in both the near- and far-field properties of the plasmonic system, which has potential for applications in active devices, such as terahertz (THz) frequency photonic devices,[32] ultrafast nanoswitches,[33,34] and sensors.[26,35] The properties of the CTP, such as the energy, intensity, and line width of the CTP resonances depend strongly on the junction conductance,[28,29] which can be altered by changing junction geometry (length, width) or material composition.[26] A more comprehensive understanding of CTP properties is still necessary that can lead to two new advances: (i) a unique tool for studying the charge transport of molecules at optical frequencies, which are not accessible electronically, and (ii) a new route to attaining tunable plasmon resonances into the infrared region.

Here, we have investigated how the optical response of colloidal gold nanorods (AuNRs) coupled to gold film is modified as the dielectric spacer layer thickness decreases below 0.5 nm. To this end, the scattering spectra of individual AuNRs coupled gold film at different thicknesses of dielectric (alumina) spacer have been analyzed. The spacer layer thickness is controlled with angstrom precision using atomic layer deposition (ALD). This accurate variation of spacer layer offers a smooth transition from the classical to quantum tunneling regime. In the classical regime, the coupling is capacitive and fundamental gap plasmon mode is observed in the scattering spectra. When the spacer layer thickness decreases to the touching limit, charge transfer plasmon becomes important. Thus, the fundamental gap plasmon mode disappears and complex higher order modes are observed for the nanorods coupled to the goldfilm in the tunneling regime.

5.2 Sample preparations and measurement techniques

5.2.1 Conformal evaporation of gold

Electron-beam evaporation is used to deposit ~50 nm gold film. The Au has been evaporated on Si substrate with 2 nm Ti adhesion layer. We have tried template-stripping method to get the ultra-smooth Au film. However, dark-field scattering measurement reveals inherent scatterers that have similar spectral characteristics as the colloidal nanoparticles conductively coupled to the film. The result is similar for films prepared following conventional e-beam evaporation of Au with very low deposition rate (Figure 5.1 a) without template stripping. The inherent scattering property is attributed to structural defects. As shown in Figure 5.1 b, these defects have similar scattering spectra as that of the gold nanorods on Au film, creating ambiguity in acquiring the dark-filed measurement.

This ambiguity is avoided by using a conformal deposition procedure. In this procedure, the mount is not on top of the crucible, rather the sample is mounted in a holder rotating at an angle from a closer distance with respect to the crucible. For the evaporation, the rate 0.3 Å/s and 0.5 Å/s for the Au and Ti, respectively are used keeping the pressure at 5e-7 Torr. In the dark-field image, we observe that the Au film does not suffer from high density of scattering defects as shown in Figure 5.1 c. The surface roughness (rms) of the Au film is 1.2 nm as determined using atomic force microscope (Veeco Quadrex D3100) (Figure 5.2 a)).

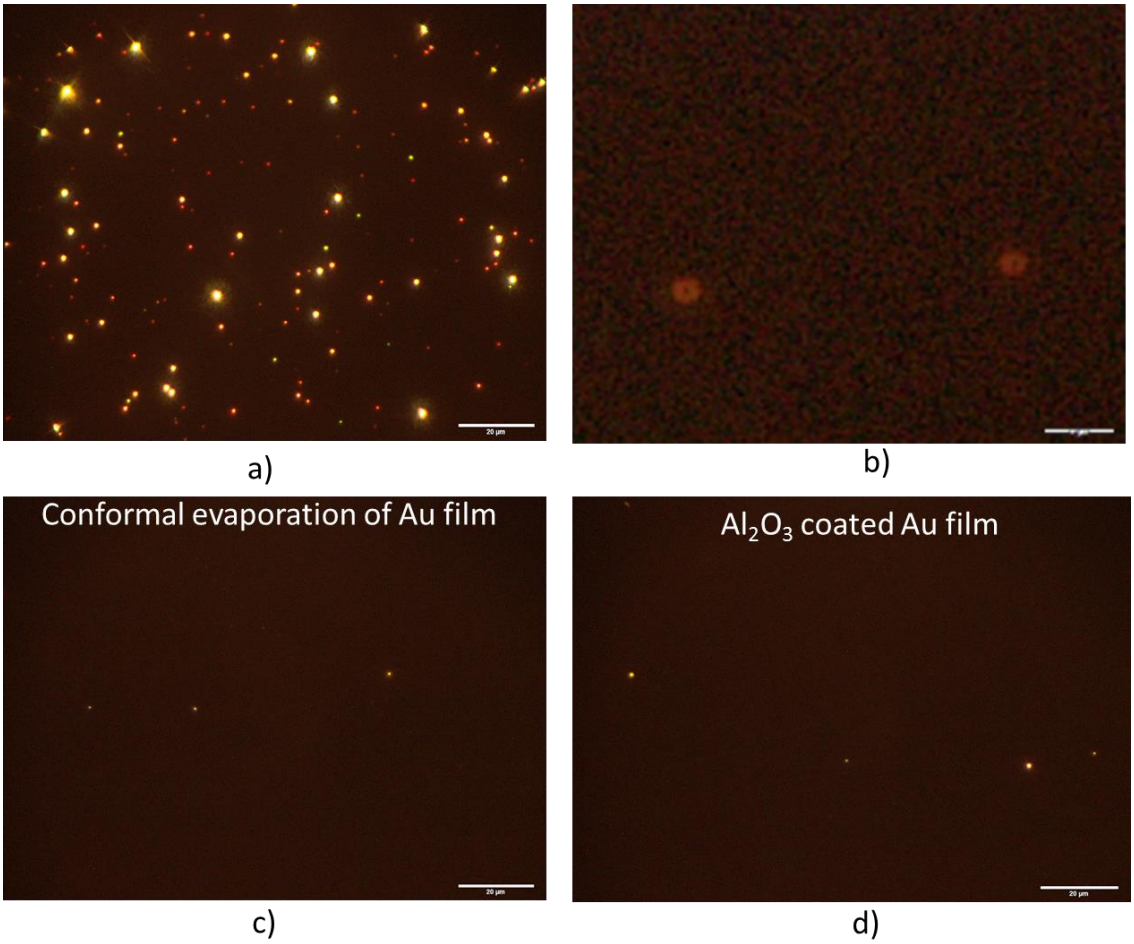

Figure 5.1 Dark-field images of a) Conventional e-beam evaporation of 100 nm Au film. Bright particles are defects on the film b) zoomed view of defects on Au film which have similar radiation pattern of AuNRs on Au film. c) Almost defects free conformal deposition of 50 nm Au film with 2 nm Ti adhesion layer achieved by tilted mount. d) 2.2 nm ALD Al_2O_3 coated conformal Au film showing no further evidence of defects during ALD growth.

5.2.2 Atomic layer deposition (ALD) of Al_2O_3 dielectric spacer

Al_2O_3 film is deposited on the Au film using the ALD system of Picosun. Trimethylaluminium (TMA) and H_2O vapors are pulsed alternately through the reaction chamber utilizing N_2 as carrier gas at a flow rate of 150 sccm and 200 sccm for TMA and H_20 respectively. The pressure inside the reaction chamber is 4 Torr with the growth temperature of 100 ^{0}C. TMA reactant exposure time (pulse time) is 0.5 s and N_2 purge following TMA exposure time is 10 s. H_20 reactant exposure time is 0.7 s and N_2 purge following H_20 exposure time is 20 s for Al_2O_3 growth on Au film. Long purge time are necessary at low temperature to prevent chemical vapor deposition of Al_2O_3.[36] This growth temperature and pulse/purge time for TMA and H_20 has been optimized carefully, since uniform and conformal deposition of Al_2O_3 bellow sub-nanometer length scale is challenging. TMA and H_2O yield ALD Al_2O_3 growth according to the following two self-limiting surface reactions,[24, 25]

$$AlOH^* + Al(CH_3)_3 \rightarrow AlOAl(CH_3)_2^* + CH_4 \quad \ldots\ldots\ldots\ldots\ldots\ldots A$$

$$AlCH_3^* + H_2O \rightarrow AlOH^* + CH_4 \quad \ldots\ldots\ldots\ldots\ldots\ldots\ldots\ldots B$$

where the * denotes the surface species. The overall reaction for ALD Al_2O_3 is,

$$2Al(CH_3)_3 + 3H_2O \rightarrow Al_2O_3 + 3CH_4$$

The AFM topography image in Figure 5.2b shows the uniform, conformal deposition of 1.2 nm Al_2O_3 film on 50 nm Au film. As the Al_2O_3 film thickness is so thin, it follows the roughness of the Au film. We do not observe any island formation in the AFM image due to chemical vapor deposition (CVD) which might be possible for running

few AB cycles to grow very thin layer of Al_2O_3. It has been demonstrated that ALD Al_2O_3 can be deposited directly on 50 nm Ag film even for the first cycle with a linear growth rate, and there are no indication of inhibited initial growth as might be expected for ALD Al_2O_3 on noble metal surface.[38] These TMA and H_2O sequential reactions yield atomic-layer controlled linear Al_2O_3 ALD on Au film.[39] Many previous studies have confirmed linear and conformal growth using TMA and H_2O.[24, 25,41] The Al_2O_3 film thickness per ALD cycle is 1.1 Å/s. However, this rate is not achieved for the initial cycles, and more accurate in later cycles as the TMA interact only with hydroxylated Al_2O_3 sites (see Figure 5.3).

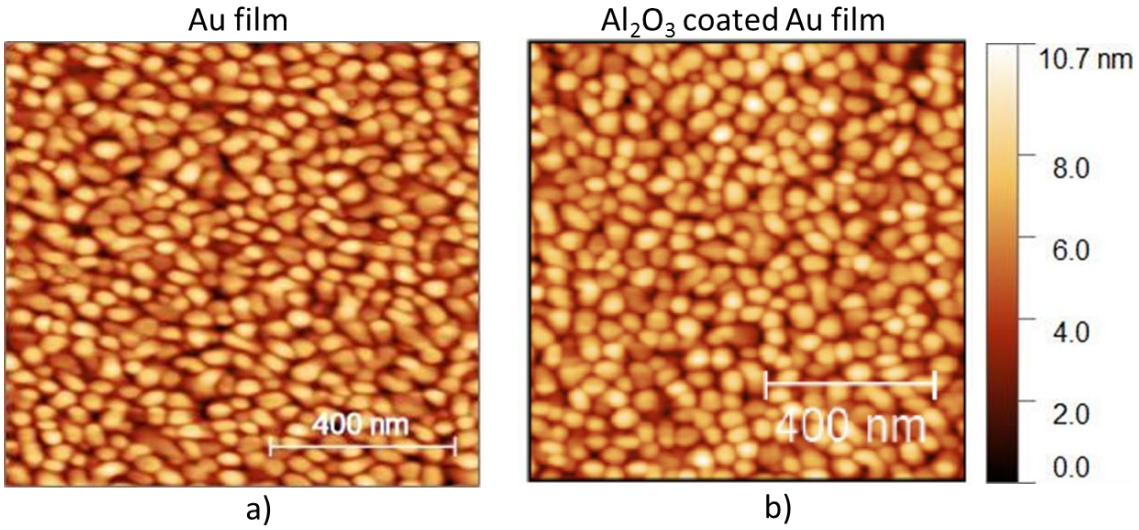

Figure 5.2 Atomic force microscopy topography images of a) 50 nm Au film with surface roughness 1.2 nm (rms). b) 1.2 nm ALD Al_2O_3 coated Au film showing no change after Al_2O_3 deposition on Au film.

5.2.3.1 Al_2O_3 film thickness measurement by variable angle spectroscopic ellipsometry (VASE)

Al_2O_3 spacer layer thicknesses are measured by J. A. Woolam Co., Inc. V- VASE using WVASE32 software. Spectroscopic scans of 600-800 nm by 10 nm interval for each

spacer layer are performed at 60^0 -70^0 with 10^0 interval relative to the normal of the surface of the sample. Ellipsometry data are analyzed using a layer model where Al_2O_3 spacer layer thickness is fitted using Cody-Lorentz oscillator provided by VASE software. Cody-Lorentz oscillator modeling of the VASE data yields a refractive index for ALD Al_2O_3 of n_{min} = 1.6603 and n_{max} = 1.6675 for the wavelength range 600 - 800 nm. For the gold film underneath the Al_2O_3 layer, optical constants from thin film-KK oscillator fit are used. We are unable to obtain fitted thickness values for the first 3 cycles of the ALD Al_2O_3 using ellipsometry, because below 0.3 nm thickness ellipsometric data are not reliable. Furthermore, we observe that extrapolation of the thickness data measured by ellipsometry produces unrealistic value for y- intercept (Figure 5.3) which is also observed by Smith *et al* [13] and Bain *et al* [42]where ellipsometric characterization is performed on self-assembled monolayers formed on gold film. Therefore, it is extremely challenging to have a precise distance dependence trend at very short distances ($\leq 0.4\ nm$) as the initial growth rate of Al_2O_3 on Au film is unknown. Lu *et al*. reported the thickness of Al_2O_3 deposition for the first four cycles is of 0.4-0.6 nm on Pd and Pt with the growth temperature of 200^0C.[41] In our case, the growth temperature is 100 ^{0}C, and the thickness for the first 5 cycles of ALD is ~0.4 nm measured by ellipsometry. Different growth rate is observed for 0-20 cycles of ALD, and 20-280 cycles of ALD as shown in Figure 5.3. Similar observation of ALD growth rate is reported by Van Duyne *et al*.[38]

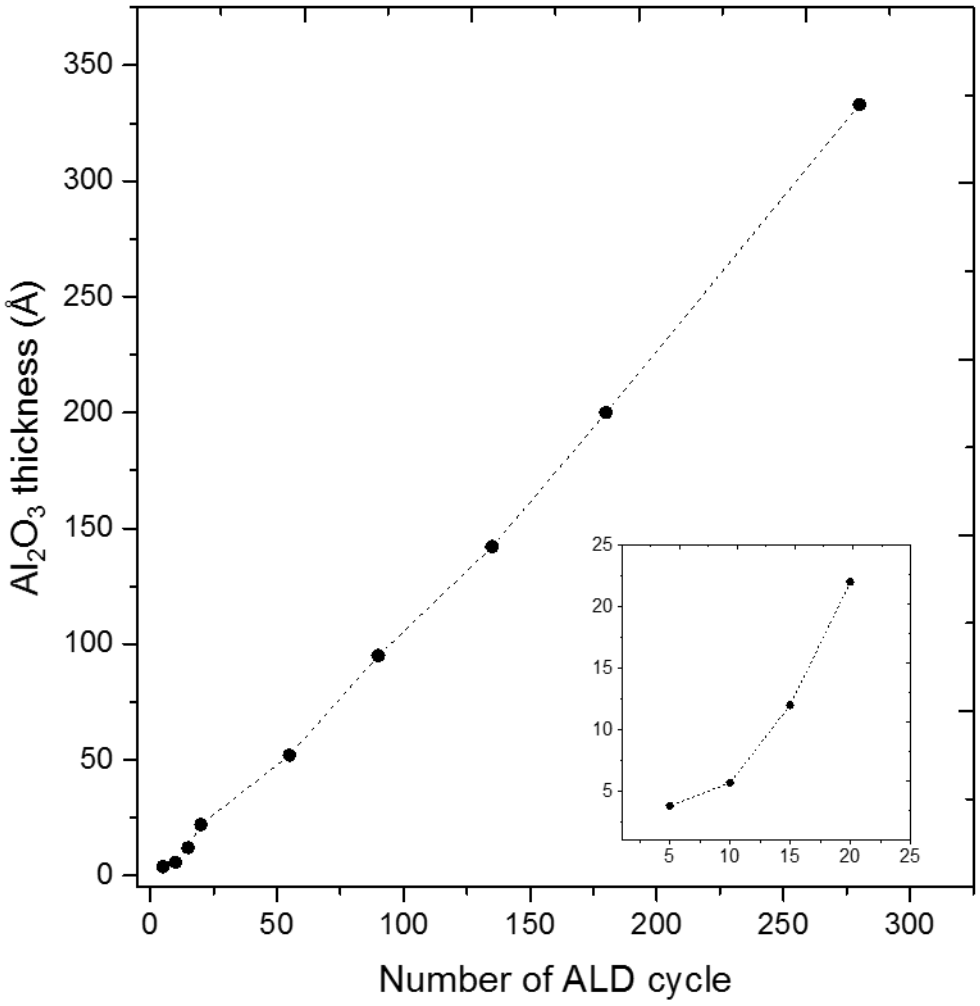

Figure 5.3 Al_2O_3 thickness as a function of number of ALD cycles. Inset focuses on Al_2O_3 thickness for initial ALD cycles.

5.2.3.2 Al_2O_3 film thickness measurement by transmission electron microscopy (TEM)

To confirm the Al_2O_3 film thickness measured by ellipsometry, TEM is used for imaging the cross section of 2 different samples: 10 ALD cycles and 55 ALD cycles. An FEI Tecnai F30 S/TEM operated at 300 kV in TEM mode is used with a 4k Ultrascan camera. Before taking the TEM images, thin cross section (< 100 nm thick) of the sample

is prepared by focused ion beam (FIB) using NOVA NANOLAB 600 dual beam at center for integrated nanotechnologies (CINT) user facility.

In the FIB, Pt is deposited in two phase as a protection layer on top of the A_2O_3 coated Au film. In the first phase, Pt is deposited by electron beam with low acceleration voltage (~5 kV) to protect the top layer. Electron beam protective coating of carbon rich Pt grows relatively slowly, and conforms to high aspect ratio structures as it is deposited. In the second phase, Pt is deposited by ion beam at high accelerating voltage (~30 kV). Ion beam is used as it is faster to deposit. Electron beam deposition of Pt is useful for samples that are sensitive to ion beam or where excellent step coverage is needed over high aspect ratio structures. Higher carbon content in electron beam can improve differential contrast for TEM.

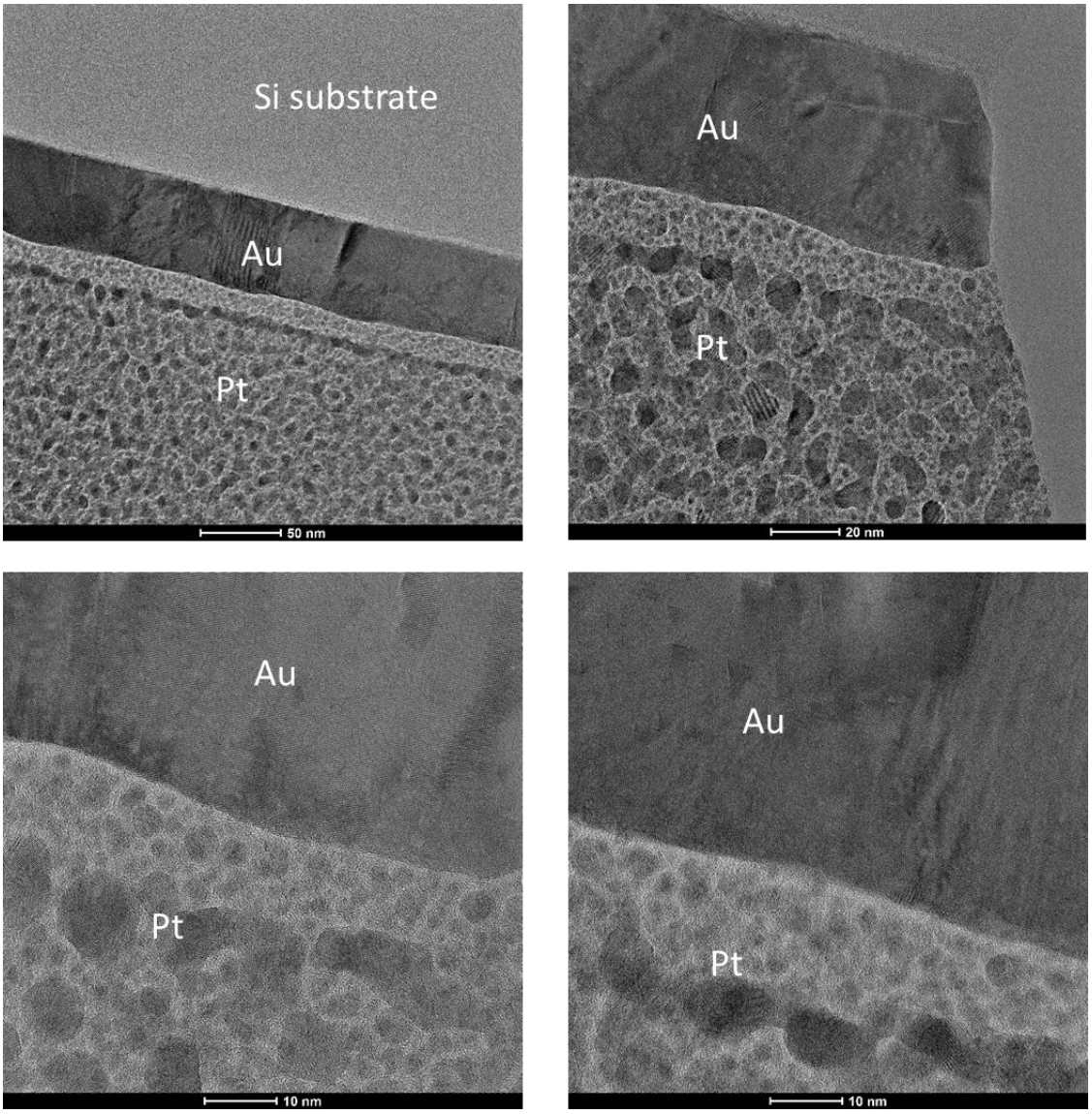

Figure 5.4 TEM images for 10 ALD cycles with different magnification (scale bars shown at the bottom) from different region

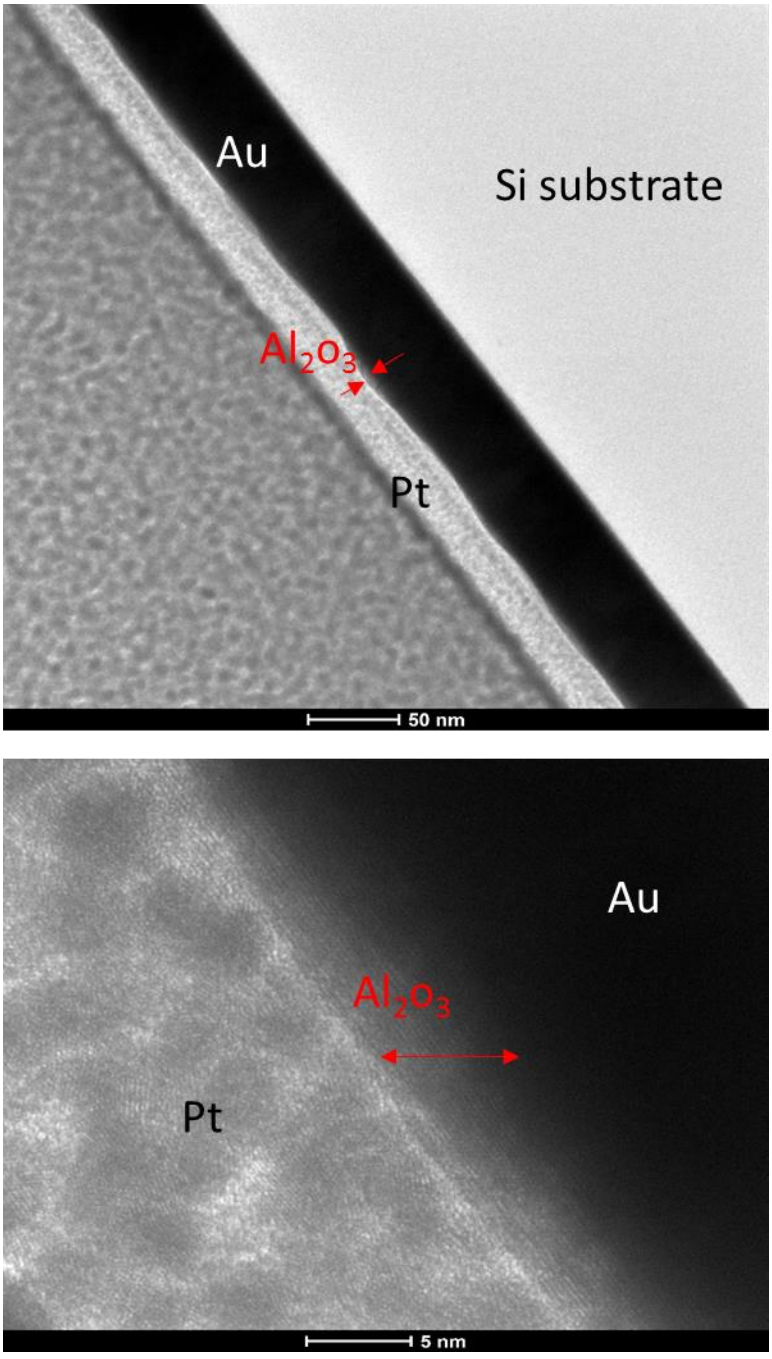

Figure 5.5 TEM images of 55 ALD cycles with low (top) and high (bottom) magnification

TEM images for 10 ALD cycles are shown in Figure 5.4. The thickness of 10 ALD cycles is 0.6 ± 0.2 nm measured by ellipsometry. But it seems difficult to conclude about

the thickness from the TEM images for this ultra-thin film of Al_2O_3. Therefore, we measure TEM images for 55 ALD cycles as shown in Figure 5.5 with low (top) and high (bottom) magnification. The Al2O3 ALD layer thickness for 55 cycles is around 6 nm confirmed by TEM. To be noted, the thickness measured by ellipsometry is $5.2 \pm 0.2\ nm$ for 55 ALD cycles.

5.2.4 Drop casting of gold nanorods (AuNRs)

Commercially available colloidal AuNRs solution from Nanopartz Inc. with aspect ratio 2 (80 nm × 40 nm) is diluted 100 times in DI water to remove excess surface ligands covering the nanorods. The AuNRs are coated with cetyl trimethylammonium bromide (CTAB). Diluted AuNRs solution is dispersed on Au film by drop-casting, and placed on a shaker for 1 minute. Then the solution blown off with N_2 gun before it dries completely to avoid particle aggregation and accumulation of excess surfactants molecules.

5.2.5 Dark-field scattering measurement

The AuNRs are excited by white light using dark-field microscope objective of numerical aperture 0.9. The dark-field scattering measurement is carried out using the GX51F5 Olympus microscope. The schematic is shown in Figure 5.6. The sample mounted on top of the objective is excited with 100W halogen lamp white light source. Dark-field images of the individual AuNRs are obtained by directing 10% of the signal to the camera (Olympus UC30) attached to the microscope. The corresponding scattering spectra are recorded by centering the particle to the focus of the objective, and directing 90% of the light collected from the sample to the spectrometer (IsoPlane Spectrograph of Princeton

Instruments), which uses a thermoelectrically cooled (-75^{0}C) and back-illuminated deep depletion CCD camera.

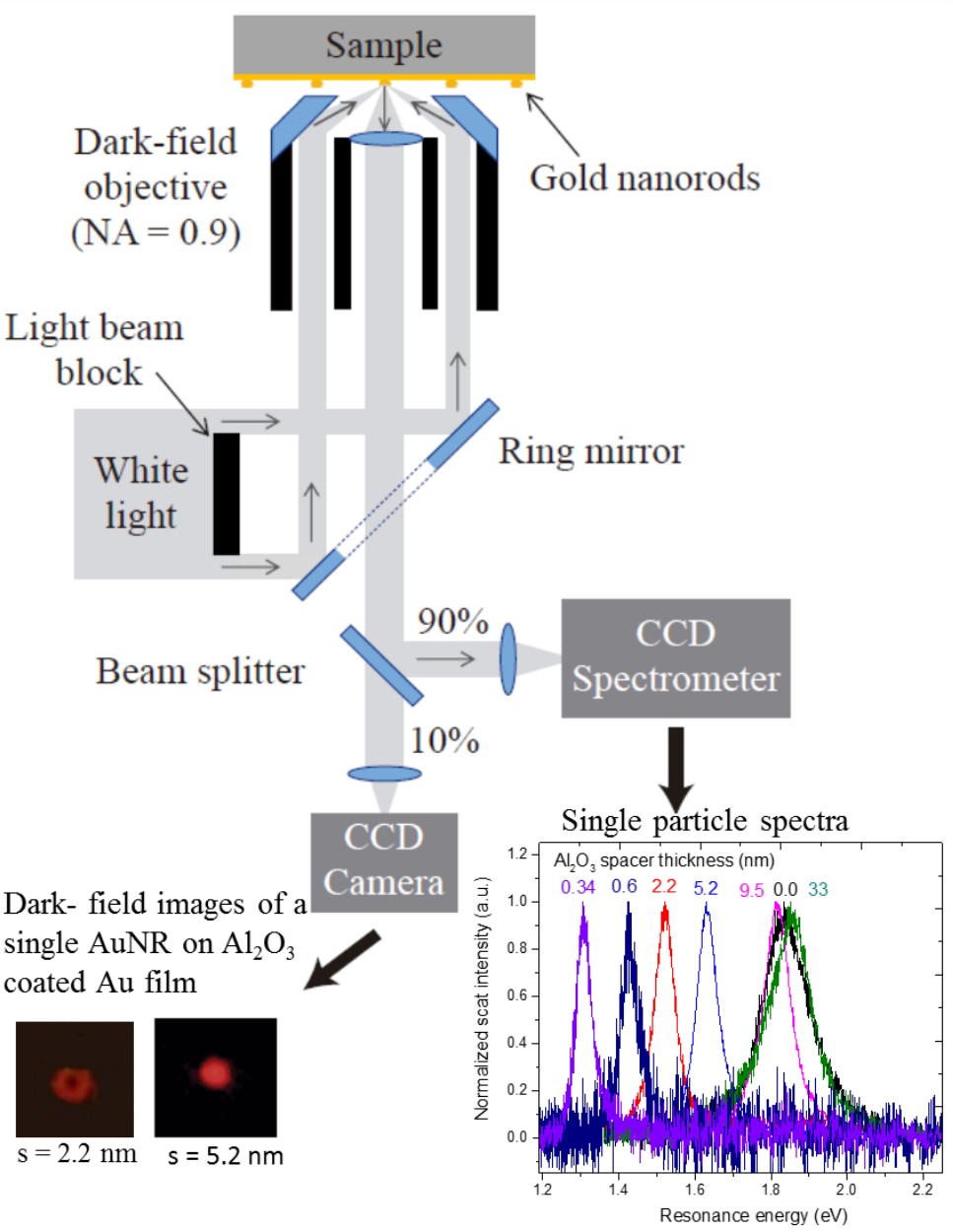

Figure 5.6 Schematic of the dark-field scattering microscopy and spectroscopy experimental setup

5.3 Results and discussion

The geometry of the gold nanorod coupled to the gold film through the ALD Al_2O_3 spacer layer is shown in the schematic in Figure 5.7a. AuNRs covered with CTAB surface ligands are placed on the Al2O3 dielectric spacer layer coated 50 nm-thick Au film deposited on Si. The optical response of the coupled particle-film plasmonic system is investigated as a function of varying Al2O3 dielectric spacer layer thickness (s) from 33 nm to sub-nanometer (<0.4 nm).

The plasmonic AuNRs are excited by focusing white light using dark-field microscope described in detail in the previous section. The normalized scattering spectra measured for individual AuNRs coupled to Au film through Al_2O_3 dielectric spacer layer of different thicknesses (s) are shown in Figure 5.7b along with their corresponding radiation pattern in dark-filed microscope image on the top. The radiation pattern of the AuNRs evolves from doughnut shape to solid spot as we increase the spacer layer thickness. The doughnut shape of the dark-filed scattering image is attributed to the vertical orientation of resultant dipole resulting from the dipole-image dipole interaction, creating a strong capacitive coupling.[28, 29] With increasing dielectric spacer layer thickness the coupling becomes weaker, as capacitance is inversely proportional to distance,

$$C = k\varepsilon_0 A/d$$

where C, k, ε_0, A and d correspond to capacitance, permittivity constant, permittivity of free space, surface area (in this case nanorod-film junction) and spacing distance (in this case, Al_2O_3 dielectric spacer layer thickness), respectively. As the interaction decreases with increasing thickness of the dielectric spacer layer, the radiation pattern transforms to

isotropic solid shape as observed in the dark-field scattering images. We observe the donut shaped radiation pattern is not resolved when the spacer layer thickness is around 5.2 ± 0.2 nm as shown on the top panel in Figure 5.7b.

For each spacer layer thickness, single particle scattering spectra of around 40 different AuNRs are acquired so that we can obtain a good estimate of average characteristics. We measure scattering spectra of AuNRs for 14 different spacer layer thickness from 33 nm to <0.4 nm, some of them are shown in Figure 5.7b. The normalized spectra for individual nanorods shown in Figure 5.7b is chosen that represents the average characteristics for that particular sample. Only one sharp plasmon resonance peak, which is the fundamental mode of the gap plasmon resonance, is observed for the spacer layer thicknesses ranging from 33 nm to 0.4 nm. Point to be noted, Al_2O_3 spacer layer thickness of 0.4 ± 0.2 nm is measured by ellipsometry for 5 cycles (5C) of ALD. This coupled plasmon mode has dipolar nature that radiates strongly.[45] There might be other modes, which radiate much weaker than dipole mode. We observe, the gap plasmon mode shifts toward lower energy as a result of increasing near-field interaction with decreasing dielectric spacer layer thickness which has been well studied.[10, 13, 28–30] Figure 5.7c shows the intensity map of 534 spectra of individual AuNRs at different spacer layer thicknesses labeled on the top. The blue dashed line is for guiding the eye to show how the average plasmon resonance energy changes with decreasing spacer layer thickness in classical region. The horizontal green dashed line indicates the average resonance energy when the AuNRs are coupled to the film conductively as determined by placing the AuNRs directly on the gold film.[27] This intensity map depicted clearly how the plasmon resonance shifts from classical to quantum tunneling regime. Peak position of the resonance energy varies

for the same sample from particle to particle, which is associated with slight variation in the coupling environment, CTAB coverage and their edge rounding.

On the plot the labels 1C-5C indicates the number of cycles used in the ALD process. The spacer layer thickness <0.4 nm are extremely challenging to be measured, hence cycle numbers of ALD process are mentioned for ultra-thin Al_2O_3 spacer layer to avoid the confusion about the thickness. The spectra for 1C-4C are shown in Figure 5.9. Classical local or nonlocal electromagnetic models can be used to describe the resonance shift from 33 nm – 0.4 nm.[13, 31] This regime is clearly capacitive in nature. The resonance energy changes drastically when the spacer layer thickness is <0.4 nm. As evidence, totally different plasmon mode is observed from 1C-4C as shown in Figure 5.7c. Using ALD we are able to access the true quantum plasmon regime where the junction of the film coupled nanorod system is no longer capacitive in nature, rather the junction turns into conductive due to quantum tunneling, and the observed mode is charge transfer plasmon mode. Hence, the spectral evolution with spacer layer thickness decreasing below 0.4 nm can be attributed to quantum tunneling phenomena.

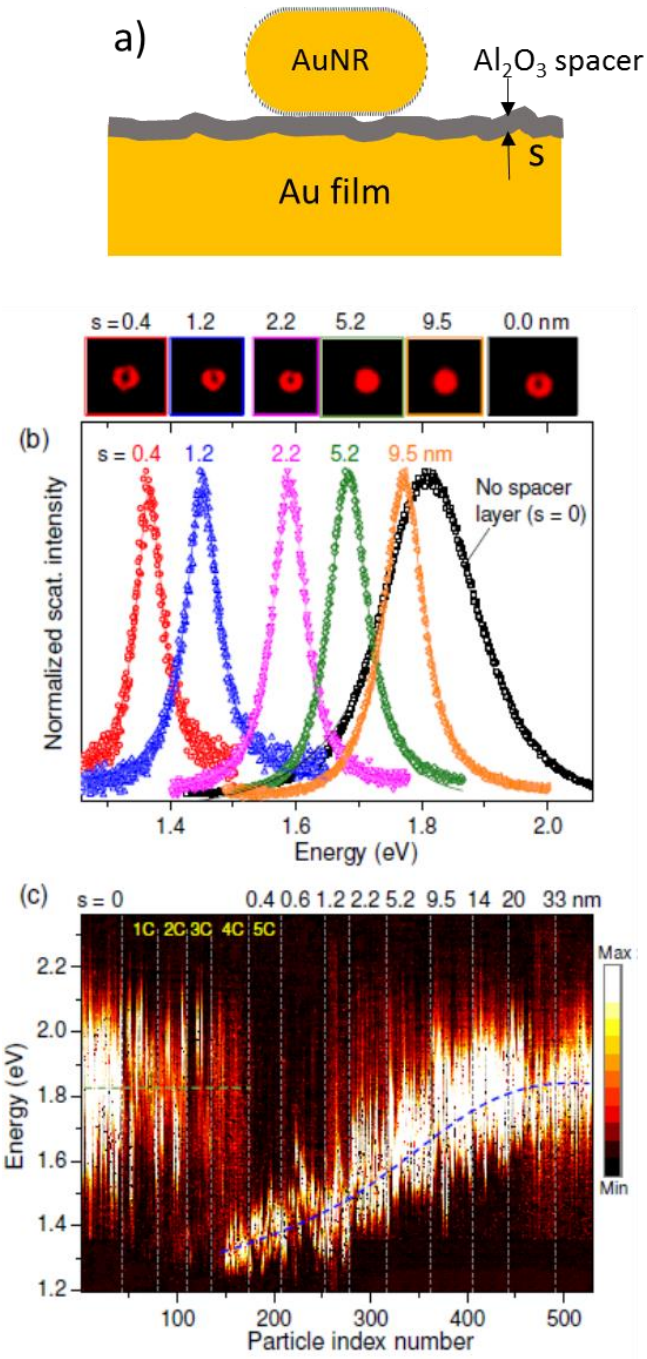

Figure 5.7 a) Schematic of the metallic film coupled plasmonic nanorod system separated by Al2O3 dielectric spacer layer. Spacer layer thickness (s) is controlled at atomic length scale. b) Normalized scattering spectra of AuNRs on Al_2O_3 coated Au film for different spacer layer thickness (s) showing red shifting with reducing the spacer layer thickness. Single particle spectra is chosen that represent the average characteristics for the spacer layer considered. The corresponding radiation pattern is shown on the top panel. c) Intensity map that includes 534 spectra of individual particles at different spacer layer thicknesses are labeled in the top x-axis. The labels 1C – 5C on the plot indicate the number of cycles used in the atomic layer deposition process. For five cycles (5C), the Al2O3 thickness is estimated as 0.4 ±0.2 nm.

Figure 5.8a depicts how the spectral linewidth changes with resonance energy. The linewidth values are extracted from the single particle spectra by fitting Lorentzian function to the experimental data. Ultra-narrow linewidth is observed with decreasing the Al_2O_3 spacer layer thickness. Narrowest linewidth of 44.8 ± 0.3 meV is extracted from 4 cycles of ALD (4C) for the spacer layer thickness of <0.4 nm. The standard deviation is also minimized as the spacer layer thickness getting narrower. Average resonance energy (left axis) and linewidth (right axis) with error bars as a function of spacer layer thickness are shown in Figure 5.8b. There is almost no change of the resonance energy for separation between 9.5 nm to 33 nm, which means the coupling between AuNRs and Au film in that spacer thickness range is insignificant, since AuNRs see only the dielectric Al_2O_3 spacer layer underneath. A red shift in the resonance is observed if the spacer layer thickness reduced further below 9.5 nm. Moreover, the shift to towards lower energy increases for spacer layer thickness below 2.2 nm - a small decrease in spacer layer thickness results a large decrease in the resonance energy. This could make devices designed in this regime, attractive for sensing applications.[46] The maximum red shift is observed for 4 ALD cycles (4C) of the thickness <0.4 nm at resonance energy 1.31 ± 0.01 eV, the narrowest linewidth (44.8 ± 0.3 meV) is also obtained for the same spacer layer thickness. This indicates, the extreme field confinement within the nanocavity where the scattering loss is significantly low. For 1C-3C cycles of ALD, we clearly observe multiple peaks which are quite different than the fundamental plasmon gap mode, and will be discussed separately in more detail in the next section. Therefore, we do not include the resonance energy and linewidth for the spacer layer of 1C-3C in Figure 5.8. To be noted, if there is no Al_2O_3 spacer layer, that is AuNRs coupled directly with the Au film, the junction becomes conductive and charge

transfer plasmon mode dominates.[27] The linewidth and resonance energy variation for this conductive junction –formed by direct coupling of the AuNRs to the Au film, in contrast with capacitive junction obtained by depositing Al_2O_3 spacer layer in between AuNRs and Au film, is presented in Figure 5.8 a- b. The spectral linewidth for AuNR-Au-film system without any spacer layer is broader, that is attributed to electron tunneling goes through resistance causing damping.

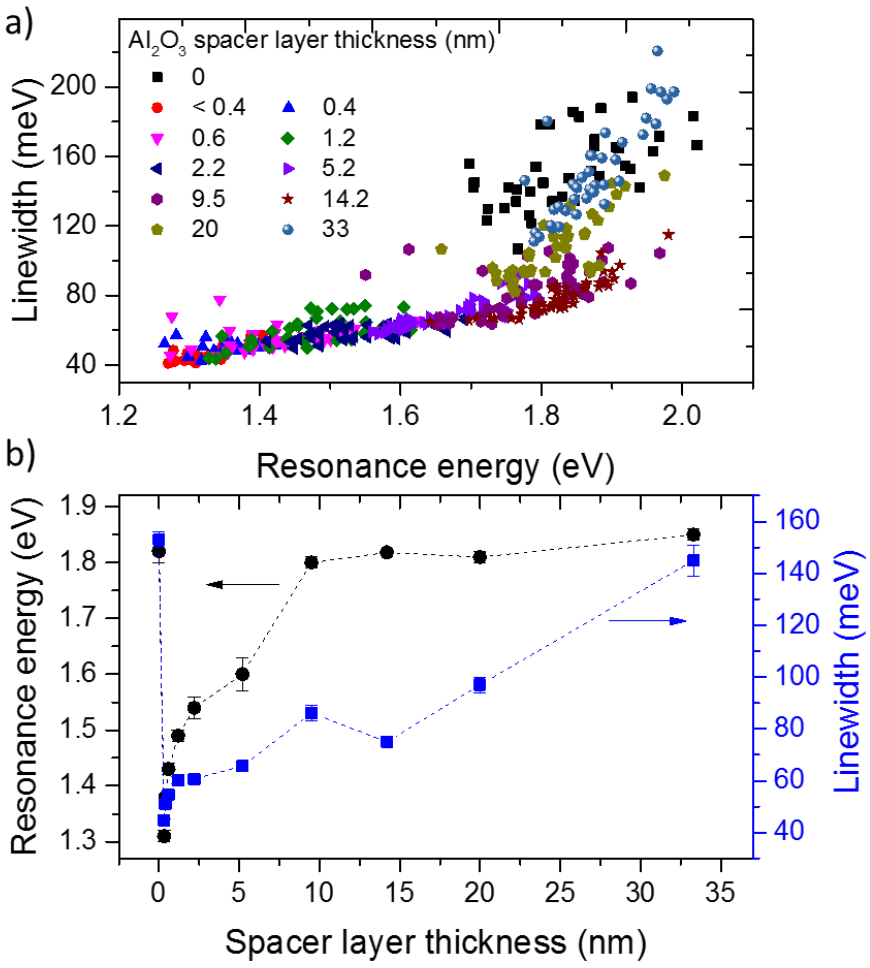

Figure 5.8 a) The spectral linewidth plotted as a function of resonance energy. The values are extracted from the single particle spectra by fitting Lorentzian function to the experimental data. b) The average resonance energy (left axis) and average linewidth (right axis) plotted as a function of spacer layer thickness. The error bars indicate the fluctuation from particle to particle.

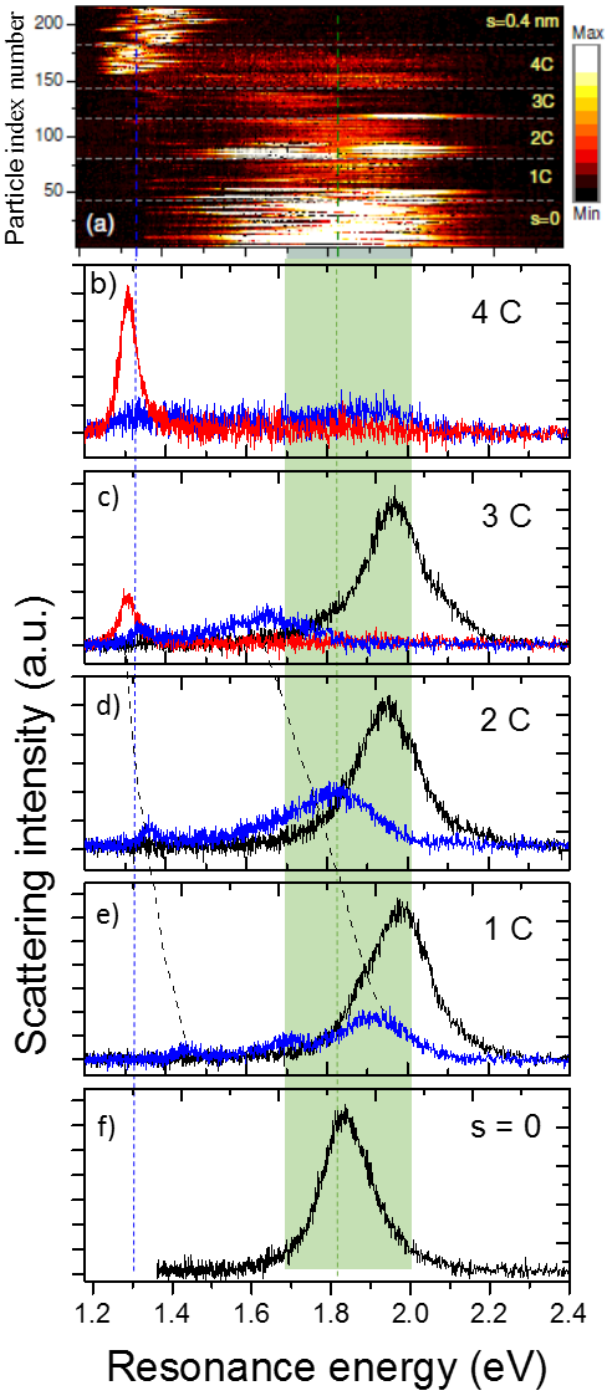

Figure 5.9 a) Intensity map of the scattering spectra of AuNRs for sub-nanometer Al2O3 dielectric spacer layer thicknesses. b) – e) Representative scattering spectra for ALD cycles 4C – 1C. The vertical dashed blue line indicates the average gap resonance energy observed for the thinnest Al2O3 spacer layer, which is obtained at 4 cycles (4C). For initial few cycles of ALD deposition, the sharp gap resonance disappears and broad resonances of various shapes appear as shown in b) – e). The main features of these resonances appear within the range of the resonance energy of the conductive coupling (shaded region) obtained when there is

no dielectric spacer layer (s = 0). The vertical dashed green line indicate the average resonance energy for s = 0. f) Representative scattering spectra of AuNRs measured for s = 0.

Intensity map of the spectra for sub-nanometer Al_2O_3 dielectric spacer layer thicknesses is presented in Figure 5.9 a. The vertical dashed blue line indicates the average gap resonance energy observed for the thinnest Al_2O_3 spacer layer that provides capacitive coupling, which is obtained for 4 cycles (4C), where gap resonance attains the lowest energy value of 1.31 ± 0.01 eV. . For the ALD cycles of four, corresponding to <0.4 nm spacer layer thickness, quantum tunneling starts to appear as indicated by the blue spectra in Figure 5.9b, but not strong enough, therefore the spectra obtained due to tunneling is extremely weak. In fact, the majority of the spectra have sharp gap plasmon mode similar to the one shown by red line in Figure 5.9b for 4C. Thus, four cycles of ALD creates Al_2O_3 spacer layer thickness that provides particle-film interaction at the boundary of classical and quantum regime. We do not observe such spectra for 5C, which indicates the coupling is completely capacitive in nature up to the thickness of ~ 0.4 nm.

Although determining the thicknesses for the first few ALD cycles using ellipsometry may not be reliable, the drastic spectral evolution is indicative of quantum tunneling and charge transfer plasmons. The drastic spectral evolution is observed, because a small change of the junction conductance can induce a large shift in the scattering strength and resonance energy.[26] As we reduce the ALD cycles further below 4C, the sharp gap resonance at lower energy disappears abruptly. For 3 cycles (3C), we observe the gap resonance is weak, and only one particle out of 27 shows up resonance at ~ 1.3 eV, shown by red spectra in Figure 5.9c. This lower energy resonance mode is not observed for 2C-1C that indicates the junction enters completely in quantum tunneling regime. We note

that, about 90% of the scattering spectra obtained for 1C-3C are similar to the blue spectra that have multiple peaks (see Appendix B), and ~10% of the scattering are similar to the black spectra with single peak as shown in Figure 5.9. The appearance of multiple peaks is attributed to excitation of higher order modes induced by electron tunneling. The main features of these resonances appear within the range of the resonance energy of the conductive coupling (shaded region) obtained when there is no dielectric spacer layer (s = 0). The vertical dashed green line indicates the average resonance energy for s = 0. As observed for 4C-1C, the system enters into the quantum regime and opens a conductance channel between the Au film and AuNRs surfaces before they touch physically. The higher energy resonances evolve more with decreasing the cycle number as tunneling becomes stronger because the conductance increases with reducing spacer thickness. We observe the charge transfer plasmon mode blue shifts with decreasing ALD cycles, indicated by black dashed line in Figure 5.9. This is attributed to reduced field enhancement and decreased coupling strength with increasing tunneling current with decreasing ALD cycles. Finally, the charge transfer plasmon mode is observed for the conductive coupling maximizing tunneling electrons, which is achieved by direct contact of the metallic nanoparticle-film system without dielectric spacer layer (s = 0), as shown in Figure 5.9 f). Unlike the conductive coupling in the presence of <0.4 nm Al_2O_3 spacer layer (4C-1C), charge transfer plasmon by direct coupling without spacer layer has one peak at higher energy ~1.82 eV, and lower energy resonances vanish. But the main features of the charge transfer plasmon resonances obtained with and without dielectric spacer layer, appear within a resonance energy range of the direct conductive coupling.

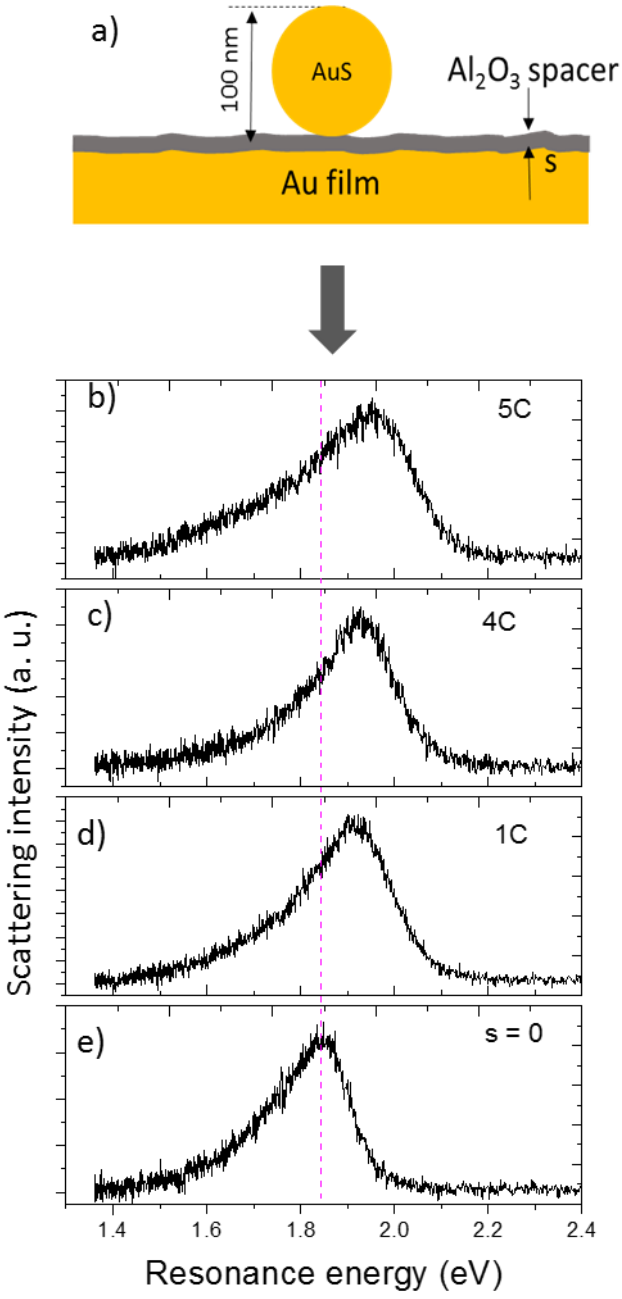

Figure 5.10 a) Schematic of metallic film coupled Au sphere through Al_2O_3 dielectric spacer (s). b)-d) Representative scattering spectra of Au sphere (diameter = 100 nm) for 5C, 4C and 1C ALD cycles, respectively. e) Representative scattering spectra of Au sphere without Al_2O_3 spacer (s = 0). Vertical dashed line indicates the average resonance energy without Al_2O_3 spacer (s = 0).

Similar experiment has been performed, for Au nanospheres of nominal diameter 100 nm coupled to Au film separated by Al_2O_3 spacer layer as shown by the schematic in

Figure 5.10a. Representative single particle spectra are shown in Figures 5.10b-e for different ALD cycles as labeled. For all cases, only broad plasmon resonance is observed. Similar, observation is also reported [49] for Au nanosphere of 60 nm diameter on Au film separated by organic and inorganic spacer layer. The charge transfer plasmon with multiple resonance energy, observed for AuNRs on Au film separated by few layers of Al_2O_3 spacer, are not observed for Au sphere at similar proximity to the gold film. As it is well known that particles with good optical quality and sharp resonances have higher field enhancement at their surfaces.[8, 50, 51] The radius of curvature for AuNRs is smaller than Au spheres with equivalent volume, therefore electric field enhancement is stronger at the surface of AuNRs than the Au spheres.

5.4 Conclusion

By controlling the distance between colloidal Au nanorods and Au film with subnanometer accuracy, experimental evidence for quantum plasmonics is presented. Atomic layer deposition of dielectric Al_2O_3 spacer layer makes precise control of the distance at atomic length scale. For the separation of ~ 0.4 nm and larger, sharp resonances of particle-film gap modes are observed due to capacitive coupling. When the separation between AuNRs and Au film is about < 0.4 nm, the system enters into quantum regime, creating conductive path, and charge transfer plasmon dominates. In this interaction regime, signatures of higher order modes are excited due to the strong charge transfer processes. With the ALD cycle number decreasing from 4 to 1, the tunneling becomes stronger as the separation getting shorter. Tunneling electrons screen the electric field, reducing field enhancement and coupling strength, resulting in the blue shifting of the charge transfer plasmon resonances. The higher order charge transfer plasmon resonance

peaks for <0.4 nm dielectric spacer layer merges with the charge transfer plasmon without spacer layer- that is due to direct contact conductive coupling. This fundamental understanding of particle-film optical interaction can give future direction for the development of non-linear optics, highly sensitive sensor, spectroscopy and many other optoelectronic devices.

References

1. Schuller, J. A. *et al.* Plasmonics for extreme light concentration and manipulation. *Nat. Mater.* **9**, 193 (2010).

2. Xu, H., Bjerneld, E. J., Käll, M. & Börjesson, L. Spectroscopy of Single Hemoglobin Molecules by Surface Enhanced Raman Scattering. *Phys Rev Lett* **83**, 4357–4360 (1999).

3. Moskovits, M. Surface-enhanced spectroscopy. *Rev Mod Phys* **57**, 783–826 (1985).

4. Nie, S. & Emory, S. R. Probing Single Molecules and Single Nanoparticles by Surface-Enhanced Raman Scattering. *Science* **275**, 1102 (1997).

5. Atwater, H. A. & Polman, A. Plasmonics for improved photovoltaic devices. *Nat. Mater.* **9**, 205 (2010).

6. Danckwerts, M. & Novotny, L. Optical Frequency Mixing at Coupled Gold Nanoparticles. *Phys Rev Lett* **98**, 026104 (2007).

7. Jackson, J. B. & Halas, N. J. Silver Nanoshells: Variations in Morphologies and Optical Properties. *J. Phys. Chem. B* **105**, 2743–2746 (2001).

8. Kelly, K. L., Coronado, E., Zhao, L. L. & Schatz, G. C. The Optical Properties of Metal Nanoparticles: The Influence of Size, Shape, and Dielectric Environment. *J. Phys. Chem. B* **107**, 668–677 (2003).

9. Moreau, A. *et al.* Controlled-reflectance surfaces with film-coupled colloidal nanoantennas. *Nature* **492**, 86 (2012).

10. Chikkaraddy, R. *et al.* How Ultranarrow Gap Symmetries Control Plasmonic Nanocavity Modes: From Cubes to Spheres in the Nanoparticle-on-Mirror. *ACS Photonics* **4**, 469–475 (2017).

11. Lassiter, J. B. *et al.* Plasmonic Waveguide Modes of Film-Coupled Metallic Nanocubes. *Nano Lett.* **13**, 5866–5872 (2013).

12. Chen, X. *et al.* Probing Plasmonic Gap Resonances between Gold Nanorods and a Metallic Surface. *J. Phys. Chem. C* **119**, 18627–18634 (2015).

13. Ciracì, C. *et al.* Probing the Ultimate Limits of Plasmonic Enhancement. *Science* **337**, 1072 (2012).

14. Tan, S. F. *et al.* Quantum Plasmon Resonances Controlled by Molecular Tunnel Junctions. *Science* **343**, 1496 (2014).

15. Zhu, W. *et al.* Quantum mechanical effects in plasmonic structures with subnanometre gaps. *Nat. Commun.* **7**, 11495 (2016).

16. Scholl, J. A., García-Etxarri, A., Koh, A. L. & Dionne, J. A. Observation of Quantum Tunneling between Two Plasmonic Nanoparticles. *Nano Lett.* **13**, 564–569 (2013).

17. Savage, K. J. *et al.* Revealing the quantum regime in tunnelling plasmonics. *Nature* **491**, 574 (2012).

18. Ward, D. R., Hüser, F., Pauly, F., Cuevas, J. C. & Natelson, D. Optical rectification and field enhancement in a plasmonic nanogap. *Nat. Nanotechnol.* **5**, 732 (2010).

19. Mühlschlegel, P., Eisler, H.-J., Martin, O. J. F., Hecht, B. & Pohl, D. W. Resonant Optical Antennas. *Science* **308**, 1607 (2005).

20. Merlein, J. *et al.* Nanomechanical control of an optical antenna. *Nat. Photonics* **2**, 230 (2008).

21. Halas, N. J., Lal, S., Chang, W.-S., Link, S. & Nordlander, P. Plasmons in Strongly Coupled Metallic Nanostructures. *Chem. Rev.* **111**, 3913–3961 (2011).

22. Duan, H., Fernández-Domínguez, A. I., Bosman, M., Maier, S. A. & Yang, J. K. W. Nanoplasmonics: Classical down to the Nanometer Scale. *Nano Lett.* **12**, 1683–1689 (2012).

23. Lassiter, J. B. *et al.* Close Encounters between Two Nanoshells. *Nano Lett.* **8**, 1212–1218 (2008).

24. Su, K.-H. *et al.* Interparticle Coupling Effects on Plasmon Resonances of Nanogold Particles. *Nano Lett.* **3**, 1087–1090 (2003).

25. Funston, A. M., Novo, C., Davis, T. J. & Mulvaney, P. Plasmon Coupling of Gold Nanorods at Short Distances and in Different Geometries. *Nano Lett.* **9**, 1651–1658 (2009).

26. Wen, F. *et al.* Charge Transfer Plasmons: Optical Frequency Conductances and Tunable Infrared Resonances. *ACS Nano* **9**, 6428–6435 (2015).

27. Kafle, B. *et al.* Robust Charge Transfer Plasmons in Metallic Particle–Film Systems. *ACS Photonics* (2018). doi:10.1021/acsphotonics.8b00554

28. Pérez-González, O. *et al.* Optical Spectroscopy of Conductive Junctions in Plasmonic Cavities. *Nano Lett.* **10**, 3090–3095 (2010).

29. Fontana, J. & Ratna, B. R. Highly tunable gold nanorod dimer resonances mediated through conductive junctions. *Appl. Phys. Lett.* **105**, 011107 (2014).

30. Savage, K. J. *et al.* Revealing the quantum regime in tunnelling plasmonics. *Nature* **491**, 574 (2012).

31. Scholl, J. A., García-Etxarri, A., Koh, A. L. & Dionne, J. A. Observation of Quantum Tunneling between Two Plasmonic Nanoparticles. *Nano Lett.* **13**, 564–569 (2013).

32. Gu, J. *et al.* Active control of electromagnetically induced transparency analogue in terahertz metamaterials. *Nat. Commun.* **3**, 1151 (2012).

33. Large, N., Abb, M., Aizpurua, J. & Muskens, O. L. Photoconductively Loaded Plasmonic Nanoantenna as Building Block for Ultracompact Optical Switches. *Nano Lett.* **10**, 1741–1746 (2010).

34. Ahmadivand, A., Gerislioglu, B., Sinha, R., Karabiyik, M. & Pala, N. Optical Switching Using Transition from Dipolar to Charge Transfer Plasmon Modes in Ge2Sb2Te5 Bridged Metallodielectric Dimers. *Sci. Rep.* **7**, 42807 (2017).

35. Pérez-González, O., Aizpurua, J. & Zabala, N. Optical transport and sensing in plexcitonic nanocavities. *Opt Express* **21**, 15847–15858 (2013).

36. Groner, M. D., Fabreguette, F. H., Elam, J. W. & George, S. M. Low-Temperature Al2O3 Atomic Layer Deposition. *Chem. Mater.* **16**, 639–645 (2004).

37. Dillon, A. C., Ott, A. W., Way, J. D. & George, S. M. Surface chemistry of Al2O3 deposition using Al(CH3)3 and H2O in a binary reaction sequence. *Surf. Sci.* **322**, 230–242 (1995).

38. Whitney, A. V. *et al.* Localized Surface Plasmon Resonance Nanosensor: A High-Resolution Distance-Dependence Study Using Atomic Layer Deposition. *J. Phys. Chem. B* **109**, 20522–20528 (2005).

39. George, S. M. Atomic Layer Deposition: An Overview. *Chem. Rev.* **110**, 111–131 (2010).

40. Groner, M. D., Elam, J. W., Fabreguette, F. H. & George, S. M. Electrical characterization of thin Al2O3 films grown by atomic layer deposition on silicon and various metal substrates. *Thin Solid Films* **413**, 186–197 (2002).

41. Lu, J. *et al.* First-Principles Predictions and in Situ Experimental Validation of Alumina Atomic Layer Deposition on Metal Surfaces. *Chem. Mater.* **26**, 6752–6761 (2014).

42. Bain, C. D. *et al.* Formation of monolayer films by the spontaneous assembly of organic thiols from solution onto gold. *J. Am. Chem. Soc.* **111**, 321–335 (1989).

43. Mock, J. J. *et al.* Distance-Dependent Plasmon Resonant Coupling between a Gold Nanoparticle and Gold Film. *Nano Lett.* **8**, 2245–2252 (2008).

44. Chen, H. *et al.* Effect of the Dielectric Properties of Substrates on the Scattering Patterns of Gold Nanorods. *ACS Nano* **5**, 4865–4877 (2011).

45. Huang, S. *et al.* Ultrasmall Mode Volumes in Plasmonic Cavities of Nanoparticle-On-Mirror Structures. *Small* **12**, 5190–5199

46. Chen, W., Zhang, S., Deng, Q. & Xu, H. Probing of sub-picometer vertical differential resolutions using cavity plasmons. *Nat. Commun.* **9**, 801 (2018).

47. Hill, R. T. *et al.* Plasmon Ruler with Angstrom Length Resolution. *ACS Nano* **6**, 9237–9246 (2012).

48. Esteban, R., Borisov, A. G., Nordlander, P. & Aizpurua, J. Bridging quantum and classical plasmonics with a quantum-corrected model. *Nat. Commun.* **3**, 825 (2012).

49. Ciracì, C. *et al.* Film-coupled nanoparticles by atomic layer deposition: Comparison with organic spacing layers. *Appl. Phys. Lett.* **104**, 023109 (2014).

50. Sherry, L. J., Jin, R., Mirkin, C. A., Schatz, G. C. & Van Duyne, R. P. Localized Surface Plasmon Resonance Spectroscopy of Single Silver Triangular Nanoprisms. *Nano Lett.* **6**, 2060–2065 (2006).

51. Hu, M. *et al.* Dark-field microscopy studies of single metal nanoparticles: understanding the factors that influence the linewidth of the localized surface plasmon resonance. *J. Mater. Chem.* **18**, 1949–1960 (2008).

Chapter 6

Summary and future directions

6.1 Summary of work

The work in this dissertation focuses on plasmon coupling of colloidal gold nanoparticle with InAs semiconductor quantum dots (QDs) in InGaAs/GaAs, and metallic gold-film, hereafter, investigate the optical interaction of localized surface plasmon resonance for semiconductor and metal, from capacitive to conductive junctions. Temperature dependence of the plasmonic effect on semiconductor quantum dots has been investigated. To achieve higher field amplification, optical interaction has been investigated for the plasmon coupled semiconductor, and metal systems, separated by a spacer layer with sub-nanometer accuracy. To this extent, conformal, uniform deposition of dielectric spacer layer precisely controlled at sub-nanometer length scale using atomic layer deposition is utilized. It is known that the characteristics of localized surface plasmon resonance depend on the particle size,[1–3] geometry,[4] orientation,[5] material, and dielectric function of the surrounding medium.[6, 7] Therefore, to couple the plasmonic structure with another nanostructure, thin-film, molecule, or quantum dot, it is vital to understand the interaction of the plasmonic coupled system for the widespread applications.[8–12]

An overview on the localized surface plasmon resonance, its properties and applications have been introduced in chapter 1. Chapter 2 focuses on understanding the effect of localized surface plasmon resonance on enhancing the carrier generation and photon emission, by monitoring the emission enhancement at room temperature, for the plasmonic system, colloidal gold nanorods (AuNRs) and InAs QDs, as an emitter

embedded in InGaAs quantum well using GaAs as a capping layer. Distance dependencies of near-field confinement, carrier diffusion and excitation energy transfer to the metal surface that leads to quenching of photoluminescence (PL) at short AuNR-InAs separation distances have been investigated systematically both experimentally and theoretically by analyzing the carrier dynamics through GaAs capping layer controlling the thickness with sub-nanometer accuracy. In Chapter 3, the effect of localized surface plasmon resonances on enhancing carrier generation and photon emission are studied by analyzing the temperature dependence of the QDs PL coupled to the colloidal gold nanorods, through the GaAs capping layer. Two peaks in the emission enhancement factor, linewidth broadening, and blue-shift in emission peak energy are the consequences of localized surface plasmon effect on QDs as a function of temperature, which help to understand the fundamental properties of carrier dynamics for plasmon coupled semiconductor QDs system at different temperatures. Then Chapter 4 focuses on controlling the gap between plasmonic nanostructures and GaAs semiconductor to optimize the emission enhancement for InAs/InGaAs/GaAs dot-in-a-well structure. Organic and inorganic spacer layers are introduced to control the gap. We show, an organic spacer is not useful for optimization of plasmon coupled InAs/InGaAs/GaAs system because of organic surfactants cetyltrimethylammonium bromide (CTAB) coated around AuNRs react with the organic spacer. Therefore, inorganic spacer layer of Al_2O_3 dielectric using atomic layer deposition is demonstrated for uniform, conformal deposition of spacer layer for controlling the gap with sub-nanometer accuracy. Al_2O_3 dielectric spacer layer for AuNR-GaAs system is explored to study the resonance properties varying the spacer layer thickness at nanometer scale. Strong plasmon coupling effect is observed even for a spacer layer thickness of 8.5

nm for AuNR-GaAs system due to high index of GaAs. The plasmon coupling effect for AuNR-GaAs (metal-semiconductor) and AuNR-SiO_2 (metal-dielectric) systems are compared using Al_2O_3 as spacer layer. In Chapter 5, the optical interaction of the metallic gold particle-film system, separated by inorganic Al_2O_3 dielectric spacer layer, using atomic layer deposition, is examined. Controlling the spacer layer thickness precisely at sub-nanometer length scale provides the opportunity to access the classical to quantum mechanical regime experimentally. Hence, the optical interactions of metallic particle-film system are investigated in capacitive to conductive junction.

6.2 Future directions

Optimization of emission efficiency for plasmon coupled InAs/InGaAs/GaAs dot-in-a-well structure has been demonstrated by controlling the gap between AuNR-GaAs interface using Al_2O_3 spacer layer. Thickness control of Al_2O_3 dielectric spacer on GaAs is attained at 150 ^{0}C using atomic layer deposition. The thinnest Al_2O_3 spacer layer achieved at that temperature is 3.5 nm. Therefore, modification is required for further optimization controlling the Al_2O_3 deposition on GaAs below 3 nm at lower temperature.

Temperature dependence of plasmonic effect for Al_2O_3 spacer layer coated InAs/InGaAs/GaAs is needed to investigate for better understanding the system.

To investigate the plasmon enhanced PL for InAs/InGaAs/GaAs QDs, wavelength (λ) = 633 nm (1.96 eV) is used for the excitation. Therefore, all the layers are excited, and we cannot separate the influence of carrier diffusion from direct carrier capture to QDs

emission. Using $\lambda = 946$ nm (1.3 eV) laser for excitation, we can study the carrier dynamics in InGaAs quantum well, that contributes to QDs emission.

To investigate the carrier dynamics for plasmon coupled InAs/InGaAs/GaAs system, plasmon enhanced PL can be monitored by overlapping the plasmon resonance with QDs emission energy (1.03 eV). To that extent, bigger AuNRs can be used that has resonance at near-infrared region. Therefore, we can easily limit the overlapping of plasmon resonance for enhancing the photocarrier absorption, using $\lambda = 633$ nm (1.96 eV) for the excitation.

Understanding the optical interactions of different plasmonic system can lead the development of plasmonic devices. Therefore, we study the distance dependence of localized surface plasmon resonance on metal, semiconductor, and dielectric material as reference, and hereafter, compare the results for different plasmonic systems. Al_2O_3 dielectric spacer layer is used with sub-nanometer accuracy using atomic layer deposition to control the distance. In Figure 6.1, the linewidth as a function of resonance energy is compared for the plasmonic system AuNR-gold film (Figure 6.1a) to AuNR-GaAs (Figure 6.1b). The resonance energy and linewidth are plotted in Figure 6.2a, and 6.2b, respectively, for the plasmonic systems, AuNR-Au film, AuNR-GaAs, and AuNR-SiO_2, as a function of Al_2O_3 spacer layer thickness. Comparing the results, we have seen that the AuNR-Au film is very attractive for higher field confinement with reduced loss, because of strong interaction of plasmon resonance with the free electrons of metallic Au-film, when a thin dielectric spacer is used. We observe interesting results for AuNR-GaAs system, varying the Al_2O_3 spacer layer. But our investigation is not complete, as we need

more data points for AuNR-GaAs, and AuNR-SiO_2 systems to have a comprehensive analysis on these systems.

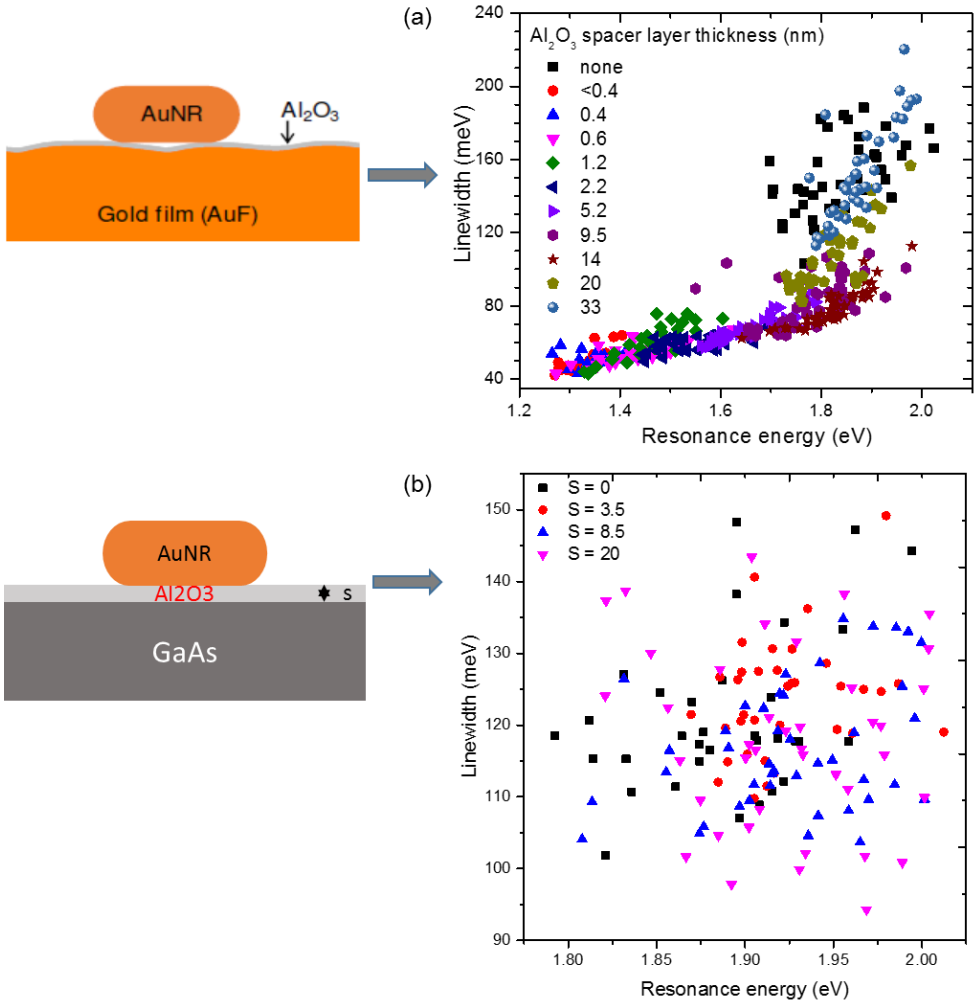

Figure 6.1 Linewidth as a function of resonance energy varying the Al_2O_3 spacer layer thickness for (a) AuNR-AuF (b) AuNR-GaAs. The schematic of the corresponding plasmonic system is shown on the left side.

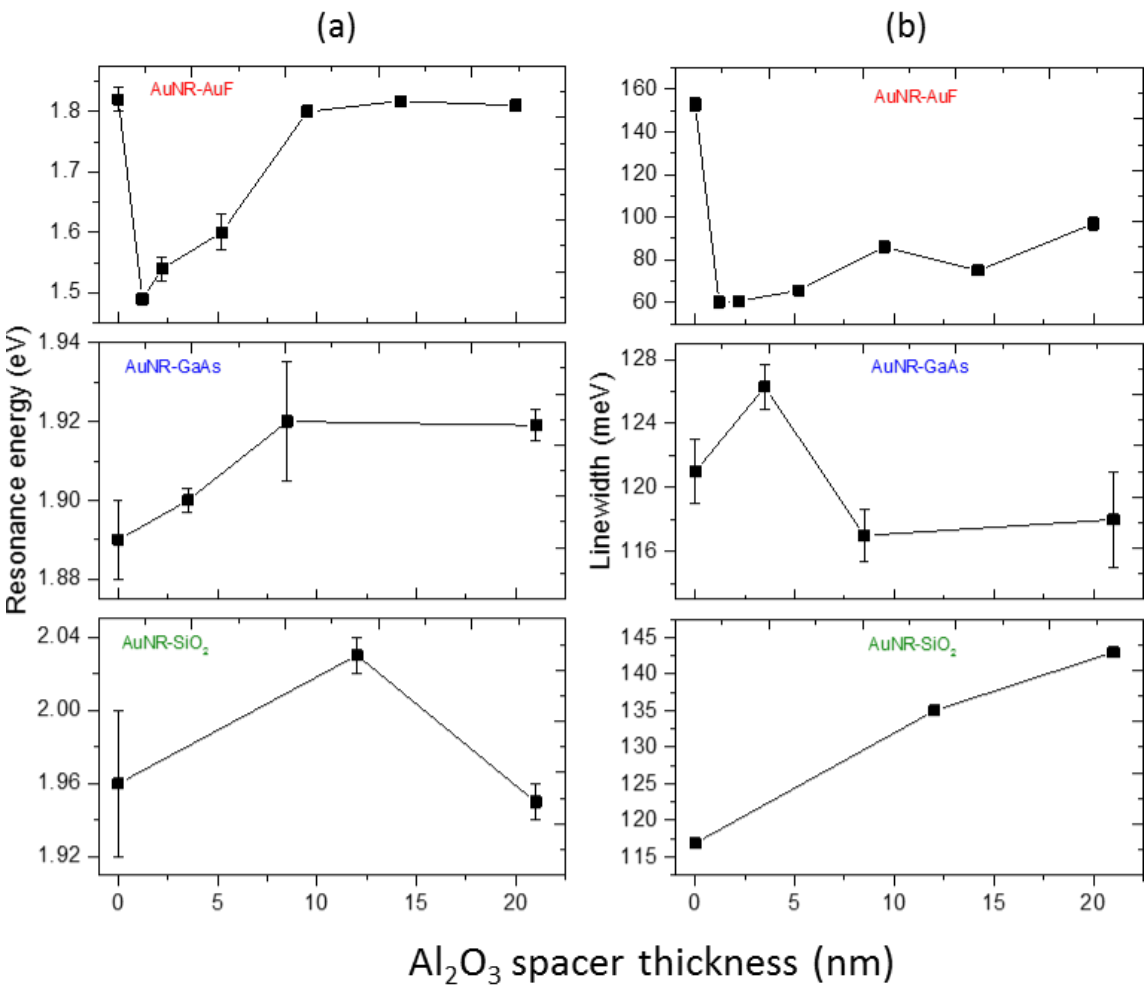

Figure 6.2 Optical interactions of different plasmonic systems, AuNR-Au film, AuNR-GaAs, and AuNR-SiO_2 as mentioned in the plot, as a function of Al_2O_3 spacer layer thickness, (a) resonance energy (b) linewidth.

The results presented in this dissertation provide insightful information of semiconductor, and metallic plasmon coupled systems, which may inspire the researchers to explore the possibilities of plasmon resonance towards the development of optoelectronics, and sensing devices.

References

1. Jackson, J. B. & Halas, N. J. Silver Nanoshells: Variations in Morphologies and Optical Properties. *J. Phys. Chem. B* **105**, 2743–2746 (2001).

2. Kelly, K. L., Coronado, E., Zhao, L. L. & Schatz, G. C. The Optical Properties of Metal Nanoparticles: The Influence of Size, Shape, and Dielectric Environment. *J. Phys. Chem. B* **107**, 668–677 (2003).

3. Huang, S. *et al.* Ultrasmall Mode Volumes in Plasmonic Cavities of Nanoparticle-On-Mirror Structures. *Small* **12**, 5190–5199

4. Sönnichsen, C. *et al.* Drastic Reduction of Plasmon Damping in Gold Nanorods. *Phys. Rev. Lett.* **88**, 077402 (2002).

5. Habteyes, T. G. Direct Near-Field Observation of Orientation-Dependent Optical Response of Gold Nanorods. *J. Phys. Chem. C* **118**, 9119–9127 (2014).

6. Knight, M. W., Wu, Y., Lassiter, J. B., Nordlander, P. & Halas, N. J. Substrates Matter: Influence of an Adjacent Dielectric on an Individual Plasmonic Nanoparticle. *Nano Lett.* **9**, 2188–2192 (2009).

7. Xu, Z. Optical Properties of Metal Clusters By Uwe Kreibig (I. Physikalisches Inst. der RWTH Aachen, Gmermany) and Michael Vollmer (Technische Physik Brandenburg, Germany). Springer: New York. 1994. xvii + 532 pp. $69.00. ISBN 0-387-57836-6. *J. Am. Chem. Soc.* **118**, 6098–6098 (1996).

8. Brongersma, M. L., Halas, N. J. & Nordlander, P. Plasmon-induced hot carrier science and technology. *Nature Nanotechnology* **10**, 25 (2015).

9. Atwater, H. A. & Polman, A. Plasmonics for improved photovoltaic devices. *Nature Materials* **9**, 205 (2010).

10. S. C. Lee, S. Krishna & S. R. J. Brueck. Plasmonic-Enhanced Photodetectors for Focal Plane Arrays. *IEEE Photonics Technology Letters* **23**, 935–937 (2011).

11. Xu, H., Bjerneld, E. J., Käll, M. & Börjesson, L. Spectroscopy of Single Hemoglobin Molecules by Surface Enhanced Raman Scattering. *Phys. Rev. Lett.* **83**, 4357–4360 (1999).

12. Tesema, T. E., Kafle, B., Tadesse, M. G. & Habteyes, T. G. Plasmon-Enhanced Resonant Excitation and Demethylation of Methylene Blue. *J. Phys. Chem. C* **121**, 7421–7428 (2017).

Appendix A

The time evolution for the level occupations N_n^{α} Nnof a quantum dot is determined for n = 1 from

$$\frac{dN_1^{\alpha}(t)}{\partial t} = \frac{\beta_1(\Omega,t)I_0(\Omega,d)}{\hbar\Omega} - \mathcal{R}_1(t) + [1 - N_1^{\alpha}(t)]\left[[\gamma_1^{\alpha}(t) + \kappa_1^{\alpha}(t)] + \sum_{m=n+1}^{M}\frac{N_m^{\alpha}(t)}{\tau_0}\right] \quad \text{..... (1)}$$

And for n ≥ 2 from

$$\frac{dN_n^{\alpha}}{\partial t} = \frac{\beta_n(\Omega,t)I_0(\Omega,d)}{\hbar\Omega} - \mathcal{R}_n(t) + [1 - N_n^{\alpha}(t)]\left[\gamma_n^{\alpha}(t) + \kappa_n^{\alpha}(t) + \sum_{m=n+1}^{M}\frac{N_m^{\alpha}(t)}{\tau_0}\right] - \sum_{m=1}^{n-1}\frac{N_n^{\alpha}(t)}{\tau_0}[1 - N_m^{\alpha}(t)] \quad \text{..... (2)}$$

where α = e or h corresponds to electrons or holes in a quantum dot, n = 1, 2, · · · , M label all the bound-state energy levels, $\hbar\Omega$sp is the energy of illuminating photons, d is the spacer-layer thickness, ττ$_0$ is the inter-level energy-relaxation time, $\mathcal{R}_n^{QD}$ (t) and β_n^{QD} (Ωsp, t) are the nth-level associated rate for spontaneous emission and absorption coefficient, $\gamma_n^{\alpha}(t)$ and $\kappa_n^{\alpha}(t)$ are the capture rates for photo-excited carriers from the spacer-layer and from the quantum well.[1]

Including the reabsorption of the quantum-dot spontaneous emission by metal nanorods on the surface of the spacer layer, we get the net rate per area from all quantum dots $\hat{R}QD = \sigma(R - Q)$, where σ is the quantum-dot areal density. The quenched quantum-dot emission spectrum is given by

$$\frac{d\tilde{R}(\omega)}{d\omega} = \sigma\left\{\eta\left[\frac{dR(\omega)}{d\omega} - \frac{dQ(\omega)}{d\omega}\right] + (1-\eta)\left[\frac{dR^0(\omega)}{d\omega} - \frac{dQ^0(\omega)}{d\omega}\right]\right\}$$

…… (3)

where η is the surface-filling fraction of metallic nanorods, the first and second terms correspond to the emission and the quenching spectra with illumination in the region with and without nanorods, respectively. Additionally, we calculate the emission and quenching spectra as[2]

$$\frac{dR\ (\omega)}{d\omega} = \frac{\sqrt{\varepsilon_b}\ e^2 x\hbar^2}{4\pi^2 \mu_r' \varepsilon_o\ \varepsilon_b}\ [\varepsilon_1^e + \varepsilon_1^h + \ \varepsilon_G\ (T)]\frac{\omega^3}{c^3}$$

$$\times \sum_{n=1}^{M} N_n^e\ \ N_n^h\ \{\frac{\Theta\ [\hbar\omega - \varepsilon_n^e - \ \varepsilon_n^h - \ \varepsilon_G\ (T)]}{[\varepsilon_1^e + \varepsilon_1^h + \ \varepsilon_G\ (T)]^2}\}\frac{\hbar\delta_n}{[\hbar\omega - \varepsilon_n^e - \ \varepsilon_n^h - \ \varepsilon_G\ (T)]^2}$$

……..... (4)

$$\frac{dQ\ (\omega)}{d\omega} = \ -\eta_{NR}\left(\frac{9\kappa^2 \Delta Z S_{NR}}{8\pi\varepsilon_b^2\ d^6}\right) Im\ [\epsilon_{NR}\ (\omega)]\frac{c^3}{\omega^3}\left[\frac{dR\ (\omega)}{d\omega}\right]$$

…… (5)

where Θ(x) is the unit-step function, $\hbar\omega$ is the energy of emitted photons, μ_r' is the reduced e-h mass in a quantum dot, ε_G(T) and ϵ_b are the bandgap energy and dielectric constant of the host material for quantum dots, ε_n^e and ε_n^h are the nth energy levels of electrons and holes, $\hbar\delta_n$ is the homogeneous level broadening of the quantum dot, ΔZ and S_{NR} are the

thickness and surface area of a nanorod, κ^2 is the orientation function between dipoles of a quantum dot and a nanorod, and Im [$\epsilon_{NR}(\omega)$] is the nanorod loss function.[3]

References

1. Haq, S. *et al.* Active Mediation of Plasmon Enhanced Localized Exciton Generation, Carrier Diffusion and Enhanced Photon Emission. *Scientific Reports* **7**, 864 (2017).

2. Huang, D. & Alsing, P. M. Many-body effects on optical carrier cooling in intrinsic semiconductors at low lattice temperatures. *Phys. Rev. B* **78**, 035206 (2008).

3. Fan, X., Zheng, W. & Singh, D. J. Light scattering and surface plasmons on small spherical particles. *Light: Science &Amp; Applications* **3**, e179 (2014).

Appendix B

Scattering spectra measured from different single AuNR for a particular Al_2O_3 spacer thickness from 1-5 ALD cycles.